FABRICATION OF OPAL-BASED PHOTONIC CRYSTALS USING ATOMIC LAYER DEPOSITION

A Thesis
Presented to
The Academic Faculty

By

Jeffrey Stapleton King

In Partial Fulfillment
of the Requirements for the Degree
Doctor of Philosophy in Materials Science and Engineering

Georgia Institute of Technology

August, 2004

FABRICATION OF OPAL-BASED PHOTONIC CRYSTALS USING ATOMIC LAYER DEPOSITION

Approved by:

Dr. Christopher J. Summers, Advisor

Dr. Rina Tannenbaum

Dr. Shawn-Yu Lin

Dr. Zhong-Lin Wang

Dr. Ken Sandhage

August 10, 2004

To Emily, my wife

ACKNOWLEDGEMENTS

I would like to express my thanks to my advisor, Dr. Chris Summers, for his support, guidance and kindness. I also would like to thank my committee members, Drs. Shawn-Yu Lin, Ken Sandhage, Rina Tannenbaum, and Zhong-Lin Whang. I also wish to express my appreciation to Dr. Elton Graugnard for his help and advice and to Curtis Neff and Dr. Wounjhang Park for their contribution to getting this project off the ground. Many thanks also to the rest of the photonic crystals research group, including Davy Gaillot, Tsuyoshi Yamashita and Dawn Heineman. Thanks also to Steve Blomquist, Dr. Eric Forsythe, and Dr. Dave Morton of the U.S. Army Research Laboratories for their assistance and for allowing me to use their facilities.

My deepest thanks also go to my family and friends. I thank my wife, Emily, for always believing in me and for enriching my life with her companionship. To my parents, Frank and Kay King, thank you for your love, caring, and enduring confidence in me. I also want to thank my mother and father-in-law, Marsha and Hunter Lindblom for their encouragement and support. I would never have completed this dissertation without the inspiration, advice, and friendship from my brothers, Bruce, Bryan, and Stephen and my brothers and sisters-in-law Tim, Susan, Sam, Paige, and Saskia. Thanks also to my friends, who have always been there to help, give me confidence, and have fun.

This project was supported by the Army Research Office under MURI contract DAAD19-01-1-0603, the Georgia Institute of Technology Molecular Design Institute, under prime contract N00014-95-1-1116 from the Office of Naval Research, and Sandia National Laboratories,under contract No. 18499.

TABLE OF CONTENTS

LIST OF FIGURES

SUMMARY

The past decade and a half has seen the rapid emergence of a new material class known as photonic crystals (PCs), structures that exhibit 1, 2, or 3, dimensional periodicity of their dielectric constant, resulting in a modification of the dispersion characteristics from the normal $\omega = \nu k$ relationship found in isotropic materials. Several remarkable electromagnetic pheonomenon result, including the formation of photonic band gaps (PBGs), which are specific energy ranges where electromagnetic wave propagation is forbidden, and the existence of energies where the photon group velocity is slowed drastically from its normal value. The resulting modification of a material's "photonic band structure" allows unprecedented control of light, resulting in phenomena such as self-collimation, and spontaneous emission modification or lasing threshold reduction through either band edge effects (low group velocity) or microcavity defect incorporation. PCs for operation at visible wavelengths are difficult to form due to the need for nanoscale fabrication techniques. The research described focused on the fabrication of photonic crystal phosphors by using the infiltration and subsequent removal of self-assembled opal templates to make inverted opal-based photonic crystals. This thesis shows the advantages that atomic layer deposition (ALD) has as an important method for use in photonic crystal fabrication, and highlights the exciting results of use of ALD to fabricate luminescent ZnS:Mn and optically inactive TiO_2 inverse opals, as well as ZnS:Mn/TiO_2 luminescent composite inverse opals.

CHAPTER I

INTRODUCTION

The past decade and a half has seen the rapid emergence of a new material class known as photonic crystals (PCs). PCs are structures that exhibit 1, 2, or 3, dimensional periodicity of their dielectric constant, resulting in a modification of the dispersion characteristics from the normal $\omega = \nu k$ relationship found in isotropic materials. This yields several remarkable electromagnetic phenomenon, including the formation of photonic band gaps (PBGs), which are specific energy ranges where electromagnetic wave propagation is forbidden, and the existence of energies where the photon group velocity is slowed drastically from its normal value. The resulting modification of a material's "photonic band structure" allows unprecedented control of light, resulting in phenomena such as self-collimation, and spontaneous emission modification or lasing threshold reduction through either band edge effects (low group velocity) or microcavity defect incorporation.[1-4] The use of photonic crystal fibers, which are 2D photonic crystals, has already found commercial application, with characteristics that ordinary optical fibers cannot offer, such as highly nonlinear performance for super continuum generation.[5, 6] PC properties are scalable with the dimensions of the periodicity, so devices can be designed for application wavelengths ranging from the UV to microwave region.

The discovery of PCs offers the potential for a wealth of new devices, with applications possible in many different fields ranging from optical computing to biosensing. However, many hurdles lie ahead for the successful realization of photonic

crystal-based devices. Fabrication techniques of today will need to be modified and novel materials processing techniques must be developed in order to make photonic crystals a success. The length scale of the dielectric periodicity must be on the order of the wavelength where the photonic band effect is desired, which unfortunately means that for photonic crystals for use at UV-IR wavelengths, materials must be patterned with lattice spacings from ~ 150 nm to several microns. The minimum feature sizes are therefore beyond the range of traditional photolithographic techniques. This thesis shows the advantages that atomic layer deposition (ALD) has as an important method for use in photonic crystal fabrication, and highlights the exciting results of use of ALD to fabricate luminescent ZnS:Mn and optically inactive TiO_2 inverse opals, as well as ZnS:Mn/TiO_2 luminescent composite inverse opals.

The research described in this thesis focused on the fabrication of photonic crystal phosphors by using the infiltration and subsequent removal of opal templates to make inverted opal-based photonic crystals. The confinement cell method pioneered by Park and Xia was used, with modifications, to fabricate high-quality self-assembled thin film opals for infiltration.[7] The technique required mono-dispersed colloidal solutions of silica spheres with less than 5% deviation. The Stober method was used to synthesize spheres in the size range 150 – 500 nm, (adequate spheres could not be purchased), and great care was taken to ensure that the spheres were monodispersed and of the correct size. [8] Small changes in sphere size affect the photonic crystal behavior of the opal, so it was critical to have a comprehensive assortment of sizes. Using these colloids, opal films of various sphere sizes were grown on both quartz and silicon substrates. The films were then sintered in order to make them structurally stable.

ALD was investigated as an effective infiltration route for fabricating inverse opals for use in the visible. Methods of infiltration such as chemical bath deposition or chemical vapor deposition have shown good results, but the resulting materials have typically shown incomplete filling and/or porosity, or complicated deposition schemes. These methods also give poor nano-scale control over the amounts of materials deposited. However, ALD has proven to be a superior method of infiltration. This technique is a flexible method of conformal film deposition that is capable of growth of all classes of materials, with monolayer control and mass production scalability. The successful implementation of photonic crystal devices will require precisely controlled coatings on complicated sub-micron three-dimensional shapes, and ALD can accomplish this goal. For example, John and Busch predict that in an inverse opal PC, the width of the photonic band gap can be increased by using highly conformal infiltration.[9] By this, they meant that the infiltrated high index material should be conformally built up on the surfaces of the spheres, but the coating process should be halted prior to filling the interstitial space completely. In order to accomplish this, the infiltration layer thickness must be highly controllable, because while the infiltration may not completely fill the void space, it still must be very uniform and conformal. The monolayer control of ALD makes it an attractive route for examining the effects of highly controlled infiltration amounts, since methods such as CBD or CVD are not sufficiently precise.

One of the potential applications for photonic crystals is the modification of spontaneous emission, and was one of the goals of this thesis. Unfortunately, luminescent materials often have insufficient refractive indices to form photonic band gaps. To solve this problem, the work described in this thesis also resulted in the successful fabrication

of multilayered luminescent inverse opal photonic crystals. These materials are made of two components: a highly luminescent material that has an insufficient index for a full band gap, and an optically inactive material that has a high index. The combination of the two materials allows us to greatly increase the refractive index contrast of the PC, while still maintaining luminescent behavior. To accomplish this goal, the work described herein had three targeted areas. First, luminescent ZnS:Mn-based infiltrated and inverse opals were demonstrated using ALD. Next, TiO_2 infiltration using ALD was studied, yielding highly conformal and tunable inverse opals. The two knowledge bases developed in the first two research phases were then combined, allowing successful formation of luminescent ZnS:Mn/TiO_2 multilayered inverse opal photonic crystals.

CHAPTER 2

PHOTONIC CRYSTALS

In recent years the need for the control of light has driven the development of many novel optoelectronic materials and devices. The principle driving area has been optical communications, since the high speed of light allows much more rapid transmission of information, and technologies such as low-loss transmission fibers, solid state lasers, and multiplexers have been developed. However, technology areas such as optical computing, information display, chemical and biological sensing, and lighting all benefit from components that increase the control of light. The proposal and subsequent experimental demonstrations of photonic crystals (PC's) have created a wealth of possibilities for devices for the modification, control, or generation of light. Following their proposed existence by Eli Yablonovitch [2] and Sajeev John [10] the last 15 years has seen an exponential growth in the theoretical and experimental work on such structures.

In 1987, Yablonovitch proposed the idea of "Inhibited Spontaneous Emission in Solid-State Physics and Electronics"[2]. He did not coin the term "Photonic Crystal" but discussed the potential for the existence of a three dimensional "electromagnetic band gap." At the time, the existence of one-dimensional PC's had already been demonstrated; they just had not been identified as such. For example, a Fabry-Perot resonator makes use of periodic layers of high and low dielectric thin films to create a forbidden gap where light propagating perpendicular to the layers is not allowed to propagate within a given range of wavelengths. This energy gap is tunable, based on the interplanar spacing and

the refractive index of each layer. Yablonovitch proposed two new ideas. First, that spatial dielectric periodicity could be extended to three dimensions, resulting in a forbidden gap in the electromagnetic spectrum for all propagation directions. Second, that the overlap of the electromagnetic band gap with the electronic band edge of a direct-gap semiconductor should result in the inhibition of radiative electron-hole recombination. These ideas suggested that PC's could be used as lossless waveguides, or as emission tailoring host materials, among other possibilities.

Less than a month after Yablonovitch's publication, S. John reported on the possible existence of "Strong Localization of Photons in Certain Disordered Dielectric Superlattices."[10] He proposed that it should be possible to create strong photon localization, resulting in electromagnetic "pseudo-gaps" by forming disordered superlattice microstructures that exhibit high dielectric contrast. John claimed that the "interplay between order and disorder leads to the restriction of coherent back scattering to certain Bragg resonance channels." Essentially, the proposal was that a properly designed material could be used to localize and trap light. The two new principles proposed by Yablonovitch and John form the foundation of PC theory; and since then the science behind theoretical modeling and experimental realization of PC's has developed rapidly.

2.1 A Description of Photonic Crystals

A PC is a periodic dielectric structure with lattice constants on the order of the wavelength of radiation of interest. This results in alternating regions of high and low

dielectric material, which, if the index contrast is high enough, causes the formation of "photonic band gaps" (PBG's). This phenomenon is very similar (but definitely not identical) to the way that in a semiconductor, the areas of high and low potential from the electronic structure of the atoms result in electronic band gap behavior. The result of a PBG is a gap in the electromagnetic density of states within a given frequency range, which yields a range of wavelengths of radiation that are not allowed to propagate in the PC. For example, Figure 2.1 shows the calculated photonic band diagram, or dispersion relation, for an inverse opal-based silicon photonic crystal, one of the most often studied photonic crystal architectures. The x-axis represents k-vectors for photon propagation within the PC, the y-axis represents normalized frequency, and the curves indicate the allowed energies at given k-vectors. For normalized frequency values from ~ 0.55 to 0.57, there are no allowed energies for any direction, resulting in a complete photonic band gap, as indicated by the grey box.

Photonic crystals can have one-dimensional, two-dimensional, or three-dimensional periodicity, as shown in Figure 2.2 – 2.4. A 1D PC consists of alternating thin films of material resulting in a structure that is uniform in two directions, but is which periodic in the third. An example of a 1D PC is a simple multi-layer Bragg stack, shown in Figure 2.2 A 2D PC is formed by fabricating a structure that has periodicity in two directions, such as by etching a periodic array of holes in a thin film as shown in Figure 2.3, or by formation of a photonic crystal fiber.[11] A 3D PC is realized by the creation of a material with periodicity in all three directions as in the synthetic opal shown in Figure 2.4. The confinement of photons within these structures is limited by their dimensionality; for example, a 1D PC can only have a band gap in one direction.

Therefore, the structure with the most potential for revolutionary new devices is the 3D PC, since it can result in complete confinement of light. Unfortunately, while this architecture is the most interesting, it is also the most difficult to fabricate. There are a number of different approaches that are being implemented for the fabrication of 3D PC structures; these will be discussed in more detail in section 2.5.

In addition to the formation of photonic band gaps, photonic crystals also enable the formation of localized defect modes. If disorder, in the form of a dielectric defect, is introduced into the lattice, it is possible to form midgap modes whose eigenfunctions are localized about the defect.[12] This disorder can be in the form of planar defects, line defects, or point defects; for example one lattice point in a 3D photonic crystal could be replaced with a different index material, either higher or lower in refractive index. If properly designed, a photonic crystal can be used to suppress the spontaneous emission from an embedded atom or molecule by positioning the photonic band gap in the same wavelength range as the emission. However, if the emission wavelength coincides with a localized defect mode, the spontaneous emission can also be enhanced.

PCs clearly provide great potential for control of light through band gaps and defect modes, but another effect that is often overlooked is the so called “group velocity anomaly.” [12] Within the photonic band diagram, there are clearly bands that form that display less slope than other bands, and are often labeled “flat” or “heavy” bands. The slope of the dispersion curves, $\delta\omega/\delta k$, is equal to the group velocity, so when the curves flatten out, the PC has a small group velocity for that frequency range. Since the group velocity is equal to the radiation energy velocity in a photonic crystal, this has the effect of increasing the interaction time between the radiational mode and the photonic crystal,

increasing coupling between them, and potentially enhancing optical processes including stimulated emission, and absorption. [3, 13]

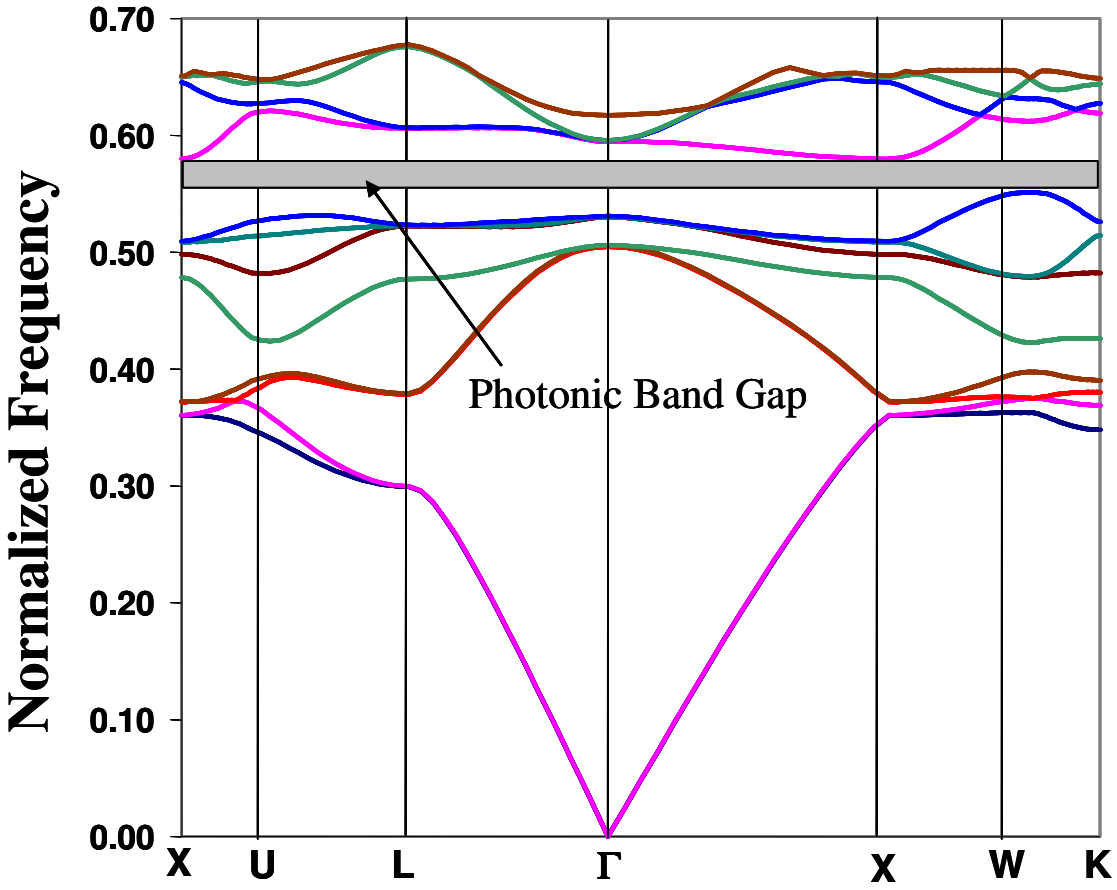

Figure 2.1 Photonic band structure of a silicon inverse opal.

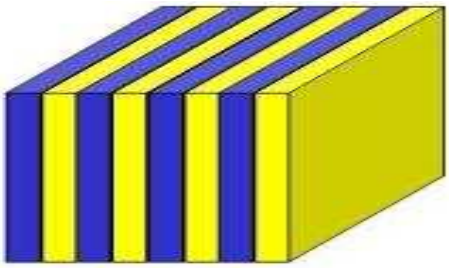

Figure 2.2 1D photonic crystal

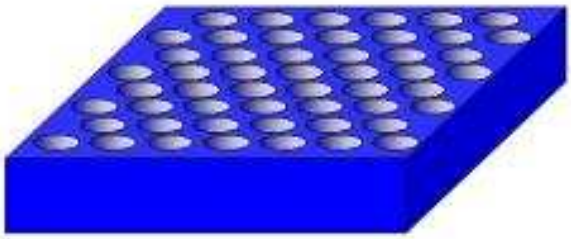

Figure 2.3 2D photonic crystal

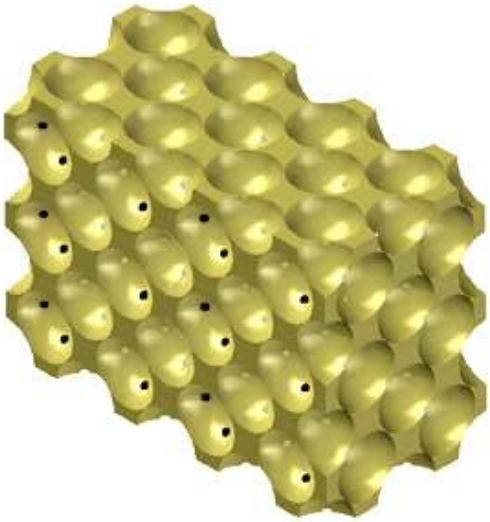

Figure 2.4 3D photonic crystal

2.2 Potential Applications of Photonic Crystals

Some potential applications of photonic crystals include all optical transistors[14], emission rate enhancement[15], improved thermovoltaics[16], super continuum generation[5], stimulated emission suppression[2], low threshold lasers[15], nonlinear optical materials[17], lossless waveguides[18], and microcavity based devices[19]. This thesis focuses on optically inactive as well as phosphor-based photonic crystals, or Photonic Crystal Phosphors (PCP's). If a PC is completely or partially composed of a luminescent material, it is possible to modify the luminescence by positioning the band gap on or near the emission wavelengths, as proposed by Yablonovitch. Also, in a similar manner to doped semiconductors, PC's can be "doped" by the introduction of carefully designed defects in the crystal. These defects cause the formation allowed states within the photonic band gap. One potential use of this architecture is to design a photonic crystal to completely suppress the emission of a broadband phosphor, but to allow a narrow emission wavelength by the introduction of a defect state within a band gap that overlaps the broad emission peak. Other useful phenomenon that photonic crystals allow are band edge emission enhancement, and increased absorption due to the decreased group velocity at band edges and where "flat" bands exist (group velocity anomaly). [12, 20] Increased absorption could improve processes ranging from chemical spectroscopy to photoluminescence. For example, instead of forming a band gap at the emission wavelength of a phosphor, it may be possible to tailor the PC so that the group velocity is very low at the excitation wavelength of the material, increasing the PL efficiency by increasing the coupling between the incident radiation field and the PC. This may be

accomplished by formation of a complete band gap at energies just below that of the excitation wavelength, or by the presence of flat bands in an incomplete band gap environment.

2.3 Photonic Band Diagrams

The ability to predict the behavior of photonic crystals is critical for the successful realization of useful structures. Three-dimensional PCs are quite difficult to fabricate, as will be discussed in section 2.5, so the only effective way to advance the field is to use computer modeling to predict which structures will have useful properties prior to fabrication. Maxwell's equations describe all macroscopic electromagnetism, including the propagation of light in a photonic crystal, and photonic band diagrams can be calculated by solving the eigenvalue problem of the wave equation derived from Maxwell's equations used to describe the propagation of EM waves in periodic media. There are several numerical methods with are commonly used to solve the equation, including the plane-wave-expansion (PWE) and the finite-difference-time-domain (FDTD) methods. Typically these numerical methods are used to calculate the photonic band diagram for a given PC configuration, which is a plot of the allowed modes for given k-vectors within the crystal.

As previously discussed, 1D photonic crystals are usually simply dielectric multi-layers, or "Bragg stacks" which have alternating high and low dielectric constant materials, and their optical properties are well known. [21] It is helpful for an understanding of photonic crystal band gap formation to examine their development in

these simple structures. Figure 2.5 shows a schematic of a 1D PC as well as its reciprocal space representation, and will be referenced in the discussion that follows.

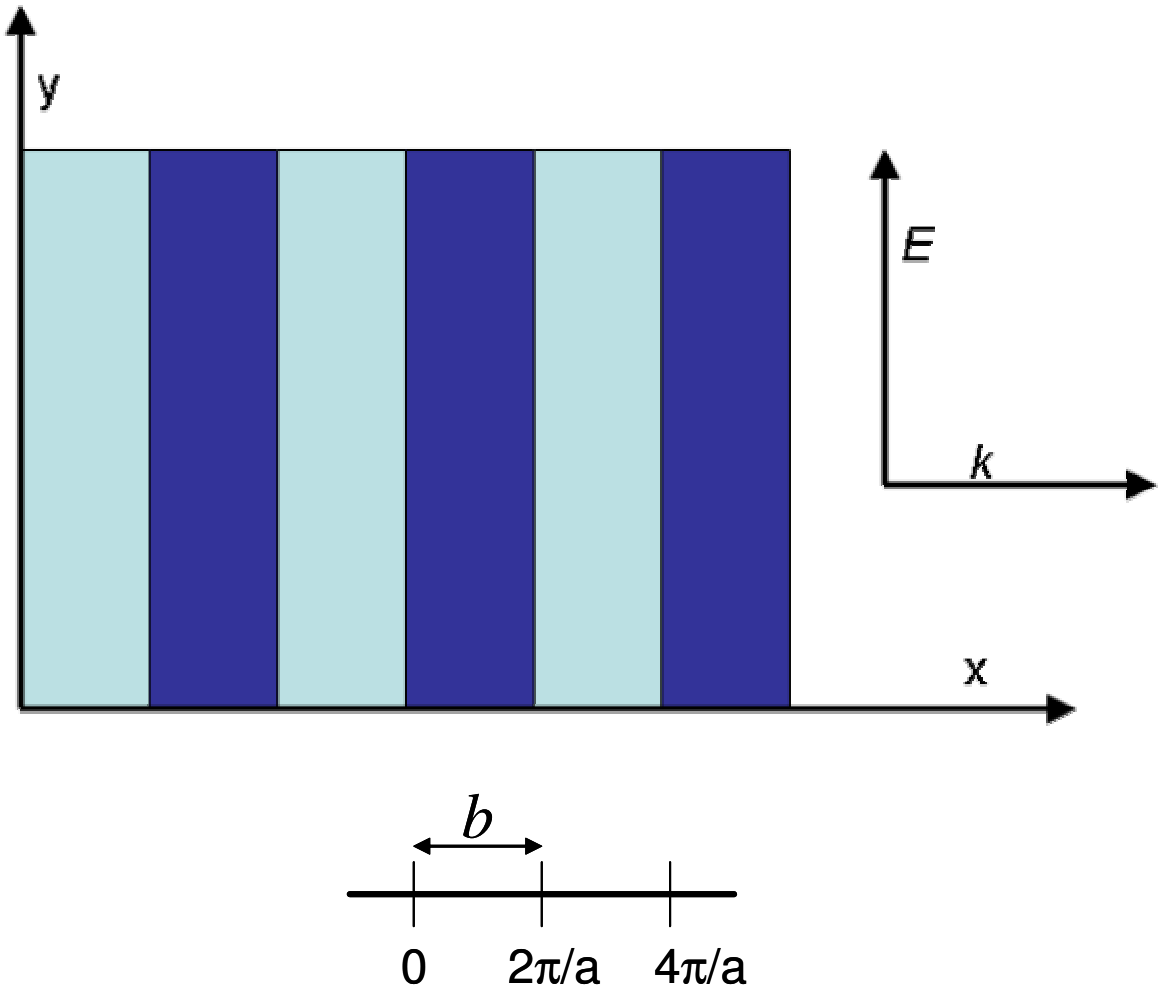

Figure 2.5 Bragg stack 1D photonic crystal, with propagating wave vector direction indicated as *k,* and electric field direction as *E*. The reciprocal space representation is also shown.

For propagation through the dielectric stack, consider the situation where the x-axis is perpendicular to the dielectric layers and denotes the direction of EM wave propagation, and the y axis lies parallel to the layers, and in the direction of the polarization of the propagating waves. The propagating waves are represented by the *k*-vector, $k=2\pi/\lambda$, in reciprocal space. *E(x,t)* denotes the electric field of the propagating wave and is a complex function for convenience. Maxwell's equations can be used to derive the wave equation:

$$\frac{c^2}{\varepsilon(x)}\frac{\partial^2 E}{\partial x^2} = \frac{\partial^2 E}{\partial t^2} \qquad (2.1)$$

In this equation, $\varepsilon(x)$ is the dielectric function, which describes the distribution of the dielectric constant as a function of position, and since it is periodic, the following equation is valid:

$$\varepsilon(x+a) = \varepsilon(x) \qquad (2.2)$$

In addition, $\varepsilon^{-1}(x)$, can be expanded as the following Fourier series, where *m* is an integer and $\{\kappa_m\}$ are the Fourier coefficients:

$$\varepsilon^{-1}(x) = \sum_{m=-\infty}^{\infty} \kappa_m \exp\left(i\frac{2\pi m}{a}x\right) \qquad (2.3)$$

In an ordinary crystal, the spatial periodicity of the potential energy that an electron experiences due to interaction with atomic nuclei causes the existence of electronic eigenstates (Bloch's theorem), and the same behavior is found for electromagnetic waves propagating in a photonic crystal. Therefore, any eigenmode in the 1D PC can be described by a wave number (k) and if ω_k is the eigen-angular frequency and $u_k(x)$ is a periodic function that can be expanded as a Fourier series, the equation:

$$E(x,t) \equiv E_k(x,t) = u_k(x)\exp\{i(kx - \omega_k t)\} \tag{2.4}$$

$$E_k(x,t) = \sum_{m=-\infty}^{\infty} E_m \exp\left\{i\left(k + \frac{2\pi m}{a}\right)x - i\omega_k t\right\} \tag{2.5}$$

Only taking components m=0 and ±1 for the inverse dielectric function, and substituting equations 2.3 and 2.5 into the wave equation, results in the following equation:

$$\kappa_1\left\{k + \frac{2(m-1)\pi}{a}\right\}^2 E_{m-1} + \kappa_{-1}\left\{k + \frac{2(m+1)\pi}{a}\right\}^2 \approx \left\{\frac{\omega_k^{\,2}}{c^2} - \kappa_0\left(k + \frac{2m\pi}{a}\right)^2\right\}E_m \tag{2.6}$$

Rewriting equation 2.6 for $m = 0$ and $m = 1$ results in:

$$E_0 \approx \frac{c^2}{\omega_k^2 - \kappa_0 c^2 k^2}\left\{\kappa_1\left(k - \frac{2\pi}{a}\right)^2 E_{-1} + \kappa_{-1}\left(k + \frac{2\pi}{a}\right)^2 E_1\right\} \tag{2.7}$$

$$E_{-1} \approx \frac{c^2}{\omega_k^2 - \kappa_0 c^2 \left(k - \frac{2\pi}{a}\right)^2} \left\{ \kappa_1 \left(k - \frac{4\pi}{a}\right)^2 E_{-2} + \kappa_{-1} k^2 E_0 \right\} \tag{2.8}$$

Equations 2.6-2.8, can be numerically solved to calculate the resulting photonic band diagram. However, the positions of the photonic band gaps can be visualized by applying a few conditions. Assuming that $k \approx |k-2\pi/a|$, (for example, $k = \pi/a$), and that $\omega_k^2 = \kappa_0 c^2 k^2$, then E_0 and E_{-1} are dominant in the electric field equation (2.5). Neglecting all other terms, the resulting two coupled equations have a non-trivial solution when the determinant of the resulting square matrix of their coefficients is equal to zero. The solution to this determinant gives the range of frequencies where no propagation mode exists for the $k \approx |k-2\pi/a|$ points:

$$\frac{\pi c}{a}\sqrt{\kappa_0 - |\kappa_1|} < \omega < \frac{\pi c}{a}\sqrt{\kappa_0 + |\kappa_1|} \tag{2.9}$$

The wave vectors that differ by multiples of π/a are identical due to the periodic nature of the crystal, and so the resulting photonic band diagram typically only includes the k-vectors $-\pi/a \rightarrow \pi/a$. An example of the resulting 1D band diagram is shown in Figure 2.6. Several phenomenon relating to this band diagram should be pointed out. First, decreasing the spatial modification of the crystal will close the band gap, and the dispersion relation will then converge to $\omega = \nu k$, as indicated by the dotted diagonal lines in the Figure. Also, decreasing the dielectric contrast will accomplish the same thing. The resulting frequency gaps are always located where the $\omega = \nu k$ dispersion lines cross.

Finally, it is important to realize that this gap only exists for waves propagating in the x-direction, since it is only a 1D photonic crystal.

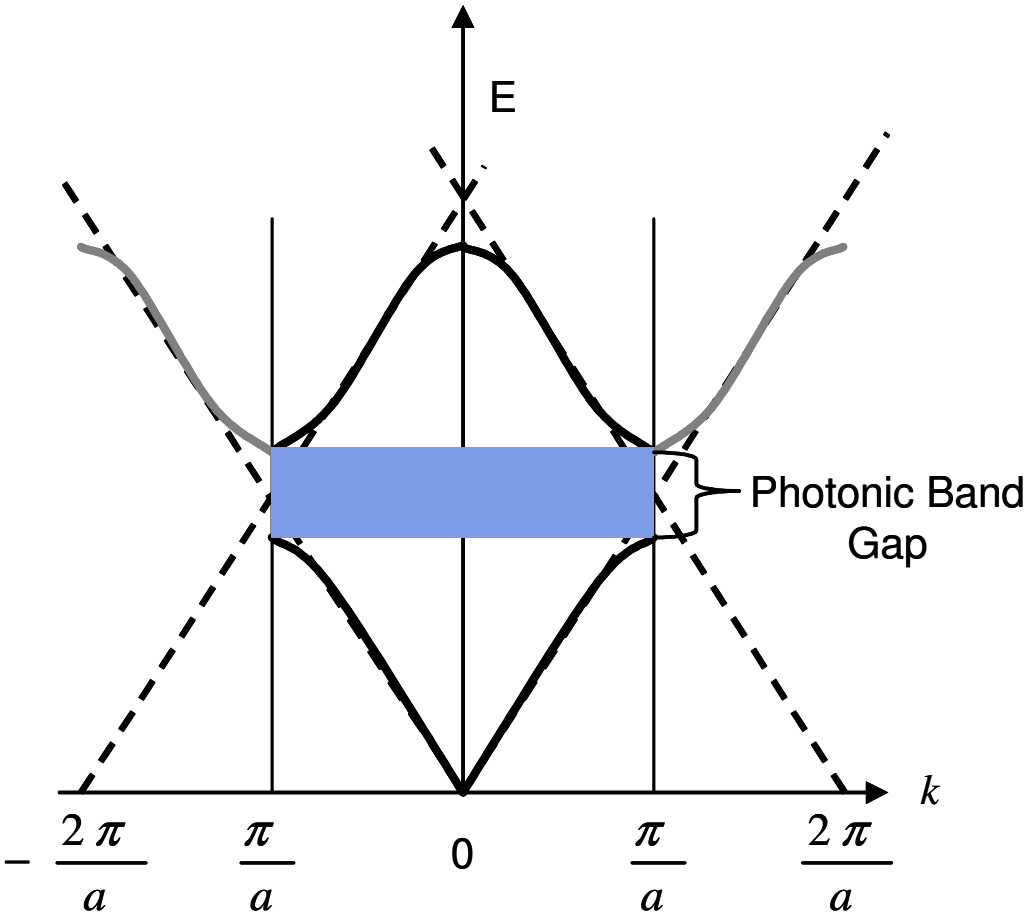

Figure 2.6 Photonic band diagram for 1D photonic crystal.

For 3D photonic crystals, the photonic band calculations are far more computationally intensive. The two most common methods are the PWE and the FDTD methods. The PWE method involves substitution of the expansions of the electric field and the dielectric function using plane waves (sin/cosine waves) into the wave equation form of Maxwell's equations (as in the previous 1D calculation), as shown in the following equations:

$$\nabla^2 \vec{E}(\vec{r},t) + \varepsilon_r(\vec{r}) \frac{\omega^2}{c^2} \vec{E}(\vec{r},t) = 0 \qquad (2.10)$$

$$\vec{E}(\vec{r},t) = \sum_{m=-j}^{j} \vec{E}_m \exp\left\{i(\vec{k}_m \cdot \vec{r} - \omega t\right\} \qquad (2.11)$$

$$\vec{\varepsilon}(\vec{r}) = \sum_{m=-j}^{j} \vec{C}_m \exp\left\{i(k_m) \cdot \vec{r}\right\} \qquad (2.12)$$

To solve the equation, it is necessary to group terms with the same exponential components, and to solve the system of $2j$ +1 equations for k and the normalized frequency (ω). This is accomplished by finding the eigenvalues of the resulting square matrix. Unfortunately, the PWE method has some limitations, including poor convergence when the dielectric contrast is too high (> 4:1).[12]

The FDTD method is a more exact computational technique and is based on numerical time integration of Maxwell's equations. However, the required computational resources increase dramatically over the PWE method. Using the time-dependent Maxwell curl equations (equations 2.13 and 2.14), and assuming both free space

propagation and no electromagnetic sources or sinks within the crystal the following sets of equations result:

$$\frac{\partial \vec{H}}{\partial t} = -\frac{1}{\mu_0}\nabla \times \vec{E} \qquad (2.13)$$

$$\frac{\partial \vec{E}}{\partial t} = -\frac{1}{\varepsilon_0}\nabla \times \vec{H} \qquad (2.14)$$

$$\frac{\partial H_x}{\partial t} = \frac{1}{\mu_0}\left[\frac{\partial E_y}{\partial z} - \frac{\partial E_z}{\partial y}\right] \qquad (2.15)$$

$$\frac{\partial E_x}{\partial t} = \frac{1}{\mu_0}\left[\frac{\partial H_z}{\partial y} - \frac{\partial H_y}{\partial z}\right] \qquad (2.16)$$

$$\frac{\partial H_y}{\partial t} = \frac{1}{\mu_0}\left[\frac{\partial E_z}{\partial x} - \frac{\partial E_x}{\partial z}\right] \qquad (2.17)$$

$$\frac{\partial E_y}{\partial t} = \frac{1}{\mu_0}\left[\frac{\partial H_z}{\partial x} - \frac{\partial H_x}{\partial z}\right] \qquad (2.18)$$

$$\frac{\partial H_z}{\partial t} = \frac{1}{\mu_0}\left[\frac{\partial E_x}{\partial y} - \frac{\partial E_y}{\partial x}\right] \qquad (2.19)$$

$$\frac{\partial E_z}{\partial t} = \frac{1}{\mu_0}\left[\frac{\partial H_y}{\partial x} - \frac{\partial H_x}{\partial y}\right] \qquad (2.20)$$

The equations of propagation can be discretized by taking central difference approximations for the derivatives of time and space. The electric and magnetic field components can then be interleaved spatially in a 3D network known as the Yee mesh. [22] The fields can then also be interleaved in time, since from the equations above, we know the that temporal response of one field is proportional to the spatial variation of the other. Hence, at a given position in space, the field at each time step can be calculated from the previous value of the field. This interleaving of the fields yields a difference equation version of Maxwell's equations, the solution of which is calculated by setting an initial condition, for example an initial magnetic or electric field, and calculating all the induced fields as time progresses. Applying a Fast Fourier Transform (FFT) to the

resulting time series and locating the resulting resonant peaks allows location of the resulting modes in energy and *k*-space.

The structures dealt with in photonic crystals are often based on the face-centered-cubic structure (FCC), whose Brillouin zone representation is shown below in Figure 2.7. Photonic band or dispersion diagrams for FCC have on their x-axis, the k-vector and on their y-axis, the normalized frequency. The high symmetry directions shown in the Brillouin zone representation are typically indicated on the x-axis. For example, propagation in the (111) direction (normal to the close-packed planes) is denoted as the Γ-L direction, and the allowed propagation modes for that direction are shown in that portion of the band. Previously presented in section 2.1, Figure 2.1, the band diagram for a silicon inverse opal photonic crystal was calculated using the PWE method, yielding a band gap width of 4.25 %.[23] For comparison, the band diagram for the same structure, calculated using the FDTD method is shown in Figure 2.8, which indicates a band gap width of 3.5 %.[24]

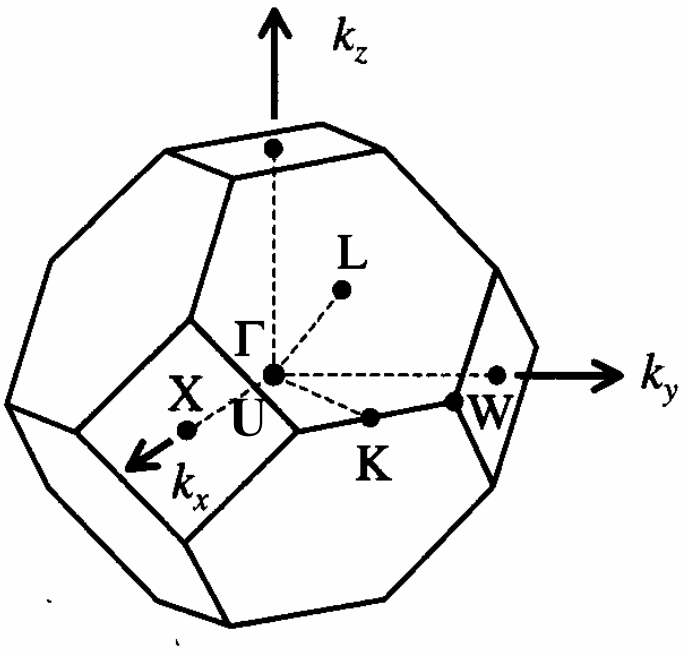

Figure 2.7 FCC Brillouin zone

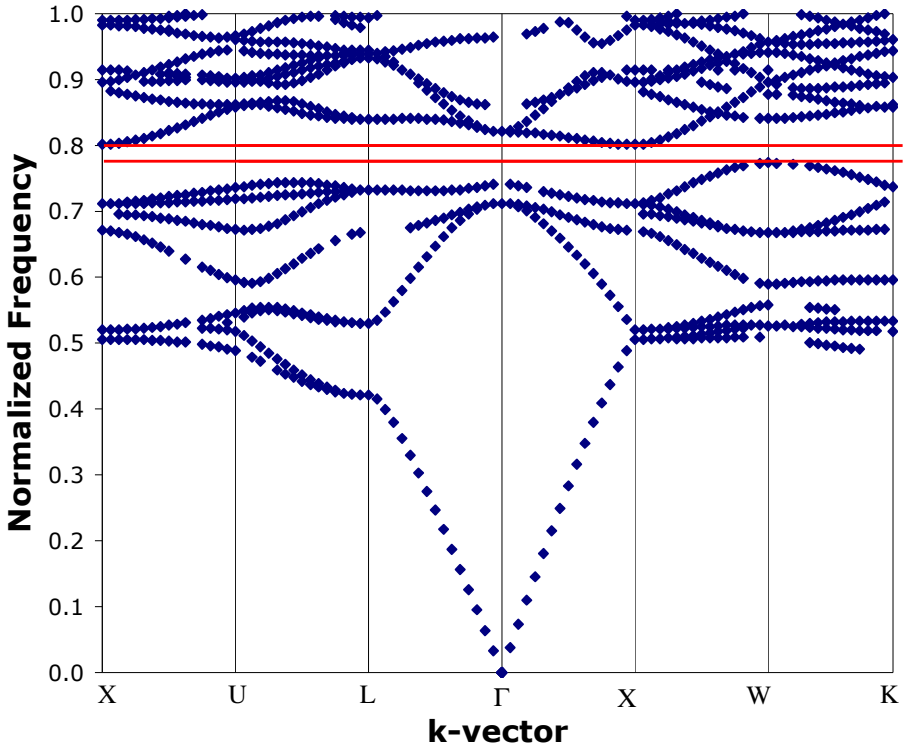

Figure 2.8: Photonic band diagram for silicon inverse opal, calculated using FDTD.

2.4 Modification of Emission in Photonic Crystals

It is well known that the density of states for electromagnetic radiation in free space where is given as:

$$D(\omega) = \frac{\omega^2 V}{\pi^2 c^3} \qquad (2.21)$$

Since the rate of spontaneous emission in a material is proportional to ω(D(ω)), the density of states substantially changes the spontaneous emission rate of atoms and molecules. [25] Two examples of material structures that can accomplish modification of spontaneous emission by this route are microcavity resonators and, of course, photonic crystals. Stimulated emission (i.e. lasers) can also be modified by photonic crystals. The amplitude amplification factor for stimulated emission is inversely proportional to the group velocity, and as such, when the photonic bands are flat a large enhancement of the stimulated emission can be expected.[12] This can lead to a large reduction in the lasing threshold which could be at the band edges, where v_g goes to zero, or at other regions of the dispersion diagram exhibiting a group velocity anomaly. There have been numerous efforts to demonstrate modification of spontaneous, stimulated, and even thermionic emission using PC's.[16, 26-31]

2.5 Three-Dimensional Photonic Crystal Fabrication Issues

In order to make a 3D PC that operates at sub-micron wavelengths, it is necessary to synthesize a material with dielectric periodicity in the sub-micron range. If the wavelength of interest is in the visible range of light (~400 – 700 nm) then the periodicity

must be on the order of λ/2n, which is 150 – 300 nm or lower, meaning the minimum feature sizes are in the 10's of nm. These dimensions complicate processing, since they are at the limits of traditional photolithography, which has proven to be exceedingly difficult for fabrication of three-dimensional photonic crystals. Yablonovitch proposed and fabricated a structure called "Yablonovite" which is formed by drilling holes in a bulk material to make a 3D periodic structure with mm scale feature sizes that exhibited a full photonic band gap in the millimeter wavelength range.[32] Figure 2.9 shows an example of Yablonovite fabricated by Chelnokov, et.al, formed using focused ion beam (FIB) milling of silicon, which has micron-sized dimensions, which results in an infrared photonic band gap [33] However, this technique would be very difficult to use for forming structures with the small dimensions required for visible wavelength applications. Another method for making 3D PC's is to make a "Log pile" structure, as shown in Figure 2.10a. This structure was successfully formed by micro-machining silicon wafers and stacking them up to successfully form a PC with a PBG in the millimeter range. [34] S. Lin et al. successfully fabricated a similar structure (Figure 2.10b) in 1998 that exhibited a PBG in the infrared using multiple steps of traditional microelectronic photolithography, etching, thin film deposition, and chemical-mechanical polishing.[35] Another promising method for fabricating 3D PC's is the use of holographic lithography to create 3D structures in epoxy-based photoresist, as shown in Figure 2.11.[36] This method is effective for making structures with the dimensions required for photonic crystals, but unfortunately, the refractive index contrast is too low to create a full PBG.

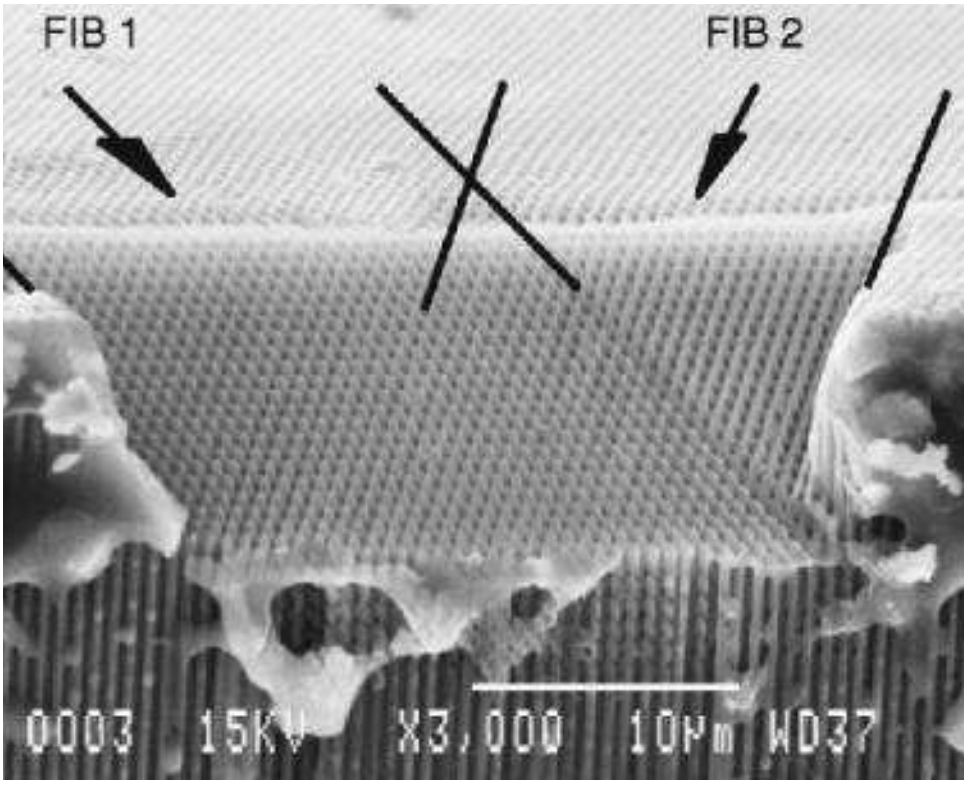

Figure 2.9 Silicon Yablonovite, fabricated using dual FIB milling. [33]

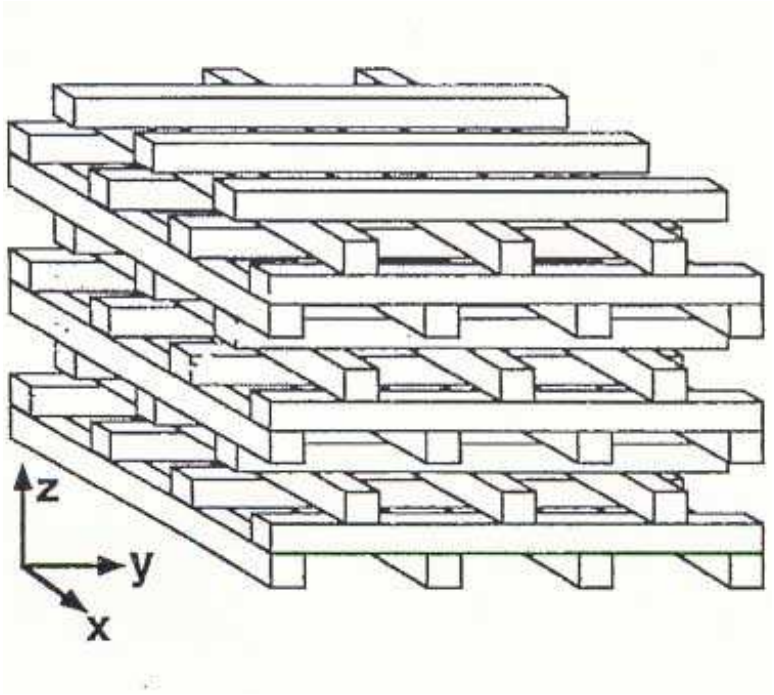

(a)

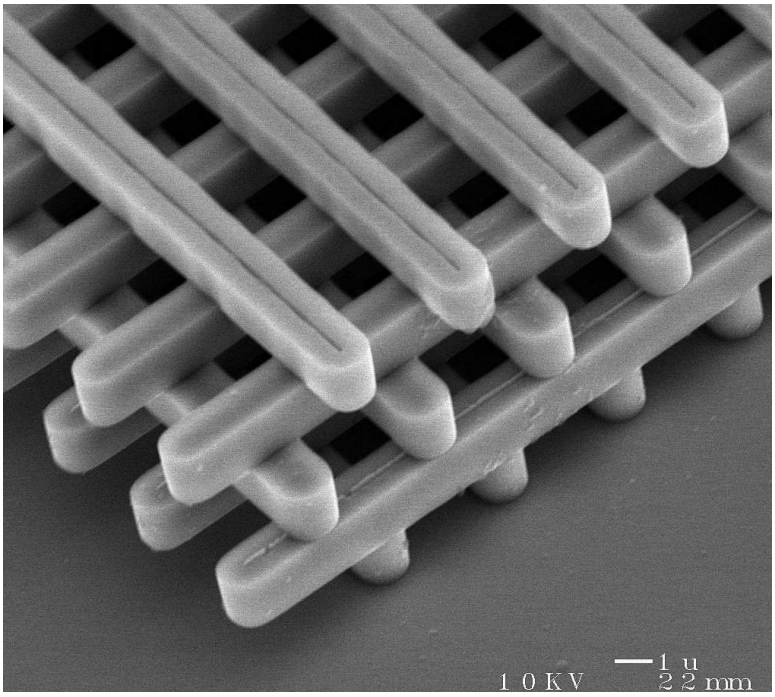

(b)

Figure 2.10 (a) 3D Log pile Structure[34] (b) Silicon 3D photonic crystal [37]

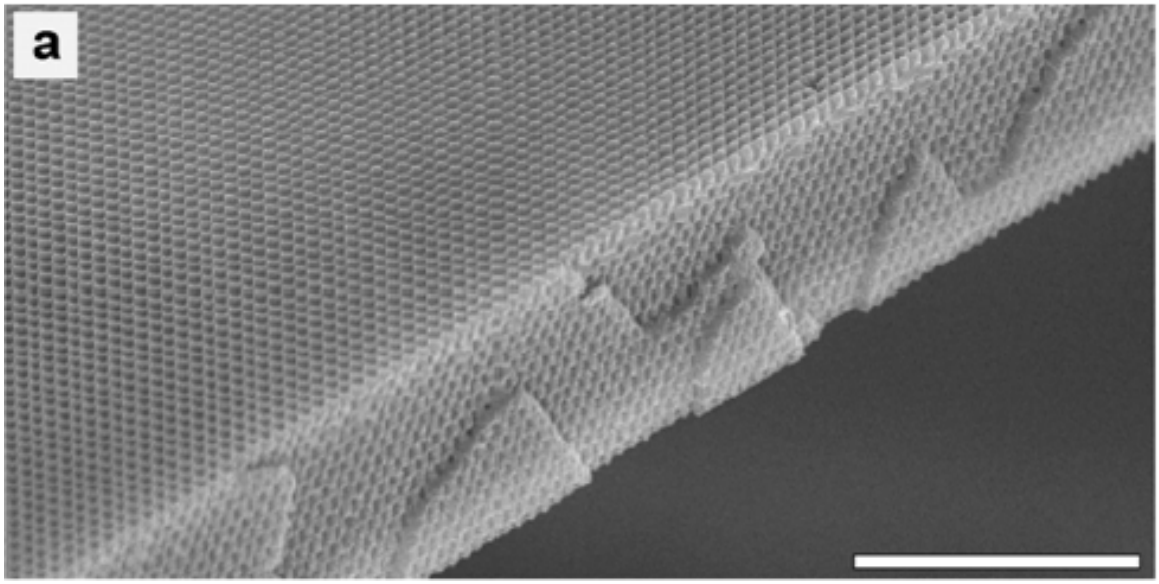

Figure 2.11 SEM image of a PC fabricated using holographic lithography. Scale bar is 10 microns. [36]

Three-dimensional PC's can also be fabricated by using a “bottom-up” approach that makes use of self-assembly to grow a 3D structure using spherical building blocks. In this case, monodispersed colloidal sub-micron spheres are first used to create an artificial opal using self-assembly, resulting in an FCC lattice of ceramic or polymer spheres that can then be used as a template for making photonic crystals. A variety of techniques can be used to form this template, ranging from pure sedimentation to forced sedimentation in a confinement cell.[7] After growth of the 3D opal, a high dielectric material is then deposited in the space between the spheres by some form of chemical or physical deposition, followed by removal of the spheres using chemical etching or burnout, thus creating an "inverse" or "inverted" opal. This route is illustrated in Figure 2.12. As predicted theoretically and demonstrated experimentally in the IR regime, the inverse opal is one of a few known 3D structures that exhibit a full photonic band gap, as previously shown in Figures 2.1 and 2.8.[38, 39] This structure does require a high refractive index contrast in order to obtain a full band gap, with the minimum index contrast predicted to be ~2.8. This method of 3D PC fabrication was used for the structures described in this thesis. The next section details some of the recent work on PC fabrication using this method.

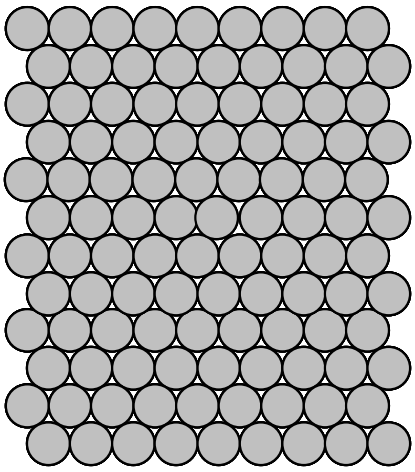

Sintered Opal

(a)

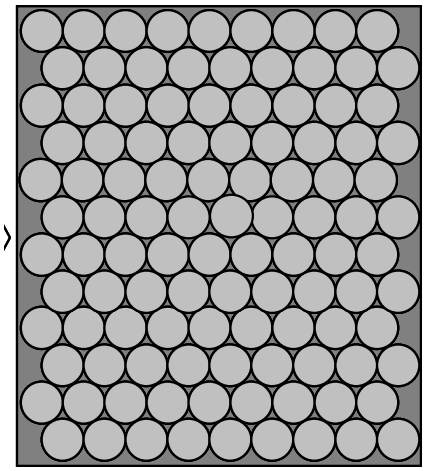

Infiltrated Opal

(b)

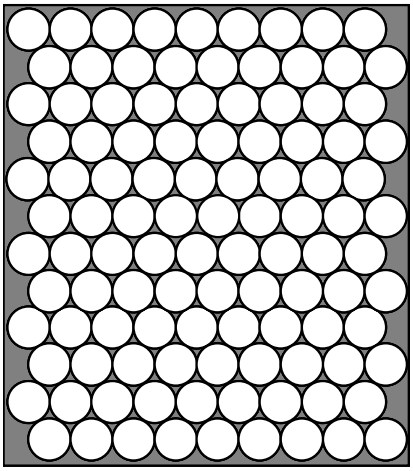

Inverse Opal

(c)

Figure 2.12 Opal-based photonic crystal structure, showing (a) self assembled, (b) Infiltrated, and (c) inverted opals.

2.6 Recent Progress in Opal Infiltration

Many groups have shown that the infiltration of opals is a suitable route for the formation of a photonic crystal. Opal templates have been grown from a variety of materials, including polystyrene, PMMA, and SiO_2. Several routes for infiltration have been pursued, including chemical bath deposition (CBD)/solution precipitation, chemical vapor deposition (CVD), low pressure chemical vapor deposition (LPCVD), atomic layer deposition (ALD), nanoparticle co-sedimentation, and liquid metal infiltration.

Since it requires no special equipment, CBD is by far the most common method for infiltrating opals. Unfortunately, it typically results in low filling fractions of material. The exceptions have been ZnS[27], which has been incorporated with approximately 50% filling of the interstitial volume and CdS[26], with filling fractions as high as 96%. However, this technique tends to produce many nano-crystallites such that the luminescent properties are poor and usually the resulting structures exhibit high porosity, which decreases the effective refractive index. In addition, there is very little control over infiltration filling fractions and the deposited material tends to grow uniformly in the void space instead of on the opal surface, making the formation of new, complex architectures such as multi-layered inverse opals impossible.

TiO_2 has a high refractive index (>2.9 for the rutile phase) making it attractive for photonic crystals. Wijnhoven, et. al. reported polystyrene opal infiltration by chemical reaction of titania precursors in the void space, followed by calcination to form TiO_2 and burn off the polystyrene spheres [40, 41]. However, this technique yields infiltrations that exhibit a high degree of roughness (~10 nm) due to the nano-crystalline nature, and low

filling fractions (~ 12%) of the void space. This technique was successful in forming the inverse opal structure. Ferroelectric $BaTiO_3$ inverse opals have also been successfully formed by solution precipitation in polystyrene opals followed by calcination[42]. As in the case of TiO_2, a high degree of roughness results from this technique. In a different work, $BaTiO_3$, $PbTiO_3$, and $SrTiO_3$ compounds were successfully infiltrated into a SiO_2 opal by similar means[43]. Ferroelectric (Pb,La)(Zr,Ti)O_3 (PLZT) inverse opal photonic crystals have also been formed with an electrically tunable photonic band gap (549.7–553.5 nm shift in peak position for 0 – 700 V), again using a solution precipitation method in a polystyrene opal[44]. Chalcogenides (As_2S_3 and AsSe) have high indices of refraction (3.5 – 3.6), strong photorefractive effect, optical non-linearity, and significant electro-optic behavior. These materials have also been incorporated into silica opals by CBD yielding up to 40% infiltration of the void space[45]. VO_2 is an interesting material because it has a semiconductor to metal phase transition that occurs at 67° C, and inverse opals have been formed by solution precipitation of V_2O_5 in silica opals followed by high temperature reduction and subsequent removal of the SiO_2 using HF[46]. SnO_2 has also been infiltrated in polystyrene opals from tin tert-butoxide precursor for use as a gas sensor[47]. Carbon inverse opals have also been fabricated by infiltrating silica opal with phenolic resin followed by pyrolyzation[48].

Chemical vapor deposition (CVD) has also been used to grow low filling fractions of GaP [49] (<32 % of void space), InP[50] , and TiO_2[51] (4% volume fraction). A CVD-like process using $SnCl_4$ and H_2S was used to infiltrate ~60% of the voids of a PMMA opal with SnS_2[52]. In this case, the inverse opal was successfully formed as well by burning out the PMMA. CVD has also been used to form inverse opals of carbon as

well[48]. The most successful of the currently used techniques (other than ALD), low pressure chemical vapor deposition has been used for infiltration of both silicon[39] and germanium,[53] exhibiting filling fractions ranging from 1-100%. This method produces the most conformal films and the best infiltration control of any technique reported other than ALD. In addition, LPCVD has been used to infiltrate opals with multilayers of both germanium and silicon, creating a Si/Ge/Si/opal structure[54].

Nanoparticle co-sedimentation is another technique that has been used in several instances, including the successful formation of TiO_2 and silica inverse opals[55, 56]. However, as in CBD, this method yields low filling fractions and high porosity. Another technique, liquid metal infiltration was used to infill a silica opal with Ga, yielding 100% infiltration[57]. This works well, but is not applicable to high melting temperature oxides and semiconductors.

For the work performed here, atomic layer deposition (ALD) was used for the infiltration step. This method has been successfully used to form both ZnS:Mn, TiO_2, and multi-layered ZnS:Mn/TiO_2 inverse opals with exhibiting high filling fractions, conformal layers, and good crystalline quality.[30, 58-60]

2.7 Importance of Infiltration "Finesse"

2D and 3D PC structures are being extensively modeled, and these studies show that changes in the structures such as shifting the distribution of dielectric material can significantly improve PBG properties. While the lattice structure (FCC, BCC, Diamond, etc.) of the PC is of utmost importance, the primitive cell structure of a photonic crystal

also plays a key role in the photonic band properties. The importance of the precise placement of the dielectric material and its effect on the primitive cell is demonstrated by the inverted "shell" structure, where the opal is infiltrated with a conformal shell-like coating, leaving small air pockets in the FCC interstitial sites. For example, in a silicon inverse "shell" opal, the width of the PBG can be increased from 4.25% to 8.6%, when the opal void space is infiltrated conformally with 90% high dielectric material, which results in an inverse opal with 24.5% overall silicon volume fraction. [9] For this thesis, the same calculation was performed for 86% filling fraction using FDTD, and a band gap width of 10% was found, as shown in Figure 2.13.[24] This filling fraction represents the maximum filling of an infiltrated opal, assuming a conformal shell growth infiltration mechanism, which will be discussed more in depth in Chapter 4. The resulting structure has well defined air pockets in the center of the interstitial sites that results from conformal infiltration, as illustrated in Figure 2.14. Similarly, the PBG width can be increased to 9.6% by the formation of a non-close-packed structure, where the basis is changed by reducing the diameter of the air spheres with respect to the lattice constant of the opal, and inserting cylindrical tubes connecting the spheres, as illustrated in Figure 2.15.[61] Thus, the performance of these structures depends critically on precisely and accurately placed high dielectric material, and the fabrication of these optimized structures will require a highly controllable infiltration method. Similarly, even for 2D and 3D photonic crystals not based on the opal architecture, highly controllable deposition methods will be imperative for maximizing desired photonic effects in real structures.

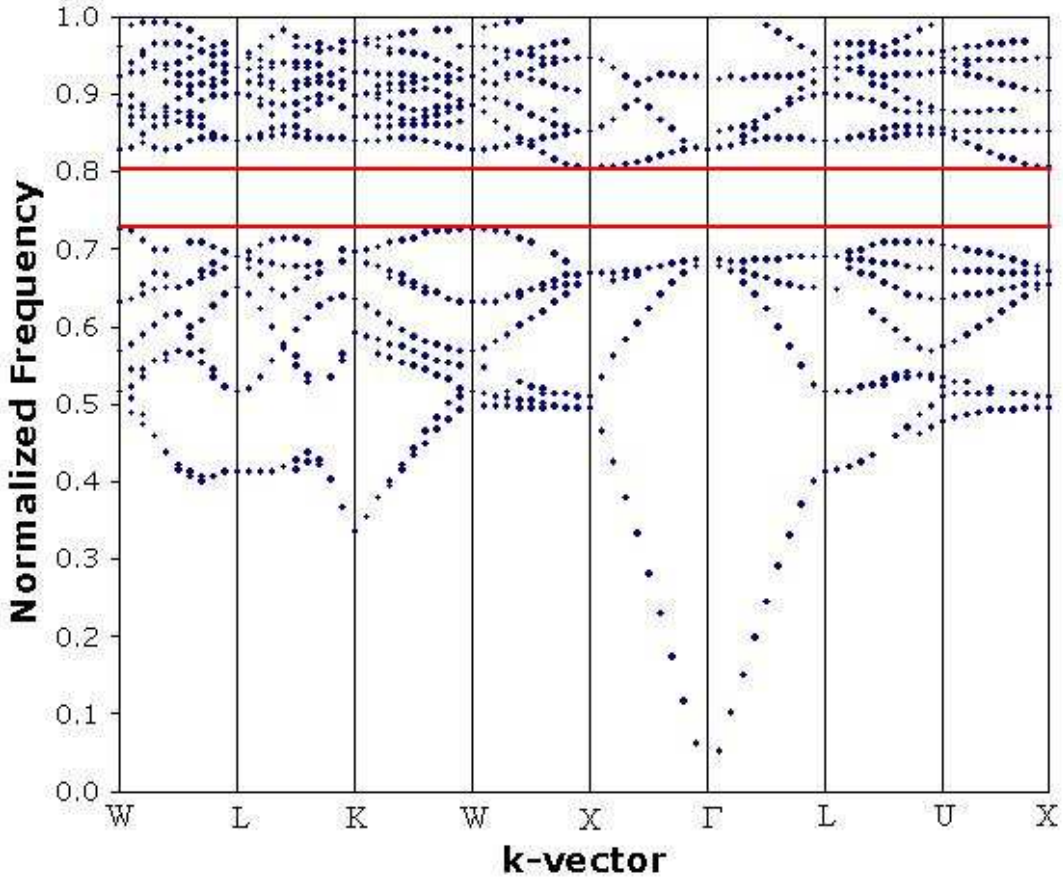

Figure 2.13 Photonic band structure for inverse silicon opal 86% infiltrated “shell” opal.

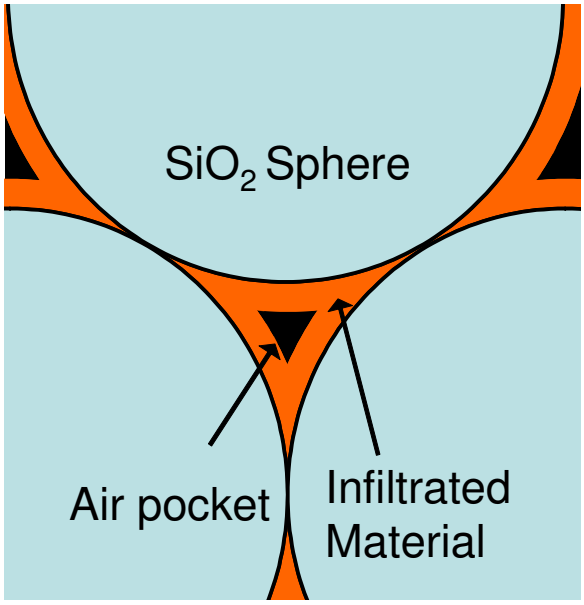

Figure 2.14 Cross section of “shell” opal infiltration.

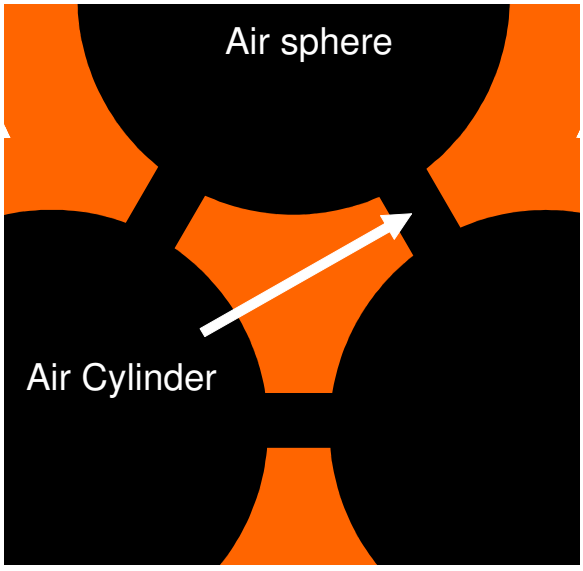

Figure 2.15 Cross section of non-close-packed inverse opal PC.

CHAPTER III

ATOMIC LAYER DEPOSITION

3.1 Principles and Advantages of Atomic Layer Deposition

Epitaxy is a growth process whereby a thin solid film is grown onto a crystalline substrate where the growing film mimics the atomic arrangement of the substrate atoms. While there are many techniques of epitaxial deposition; Atomic Layer Epitaxy (ALE) is one such method that also has the advantage of monolayer growth control. A broader term, atomic layer deposition (ALD) describes the case where the growth is not necessarily epitaxial, as is the case of the amorphous deposition of TiO_2, or in any deposition where the film does not grow to match the substrate crystal structure, as is the case when films are grown on glass. Suntola and Antson patented the "Atomic layer epitaxy thin-film growth technique" in the mid 1970's.[62] In this technique, the reactants are sequentially transported to the substrate as pulses, such that only one of the reactants is supplied to the substrate at a time.[63] Each pulse is followed by a "dead time," which typically involves an inert or reactive gas purge (sometimes H_2 is used) before the other reactant is pulsed. These pulses are either neutral molecules or atoms, delivered as chopped beams in the case of high or ultrahigh vacuum systems, or as switched vapor streams in the case of gas-flow ALD. Figure 3.1 shows a typical gas pulse sequence for ALD growth of ZnS. Figure 3.2 illustrates the events that take place during the ALD growth of ZnS.

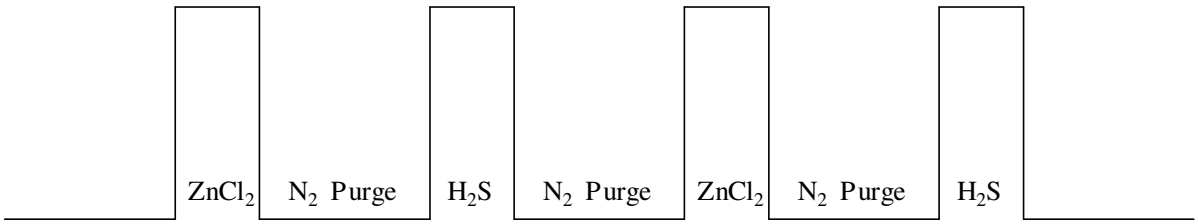

Figure 3.1 ZnS ALE deposition sequence

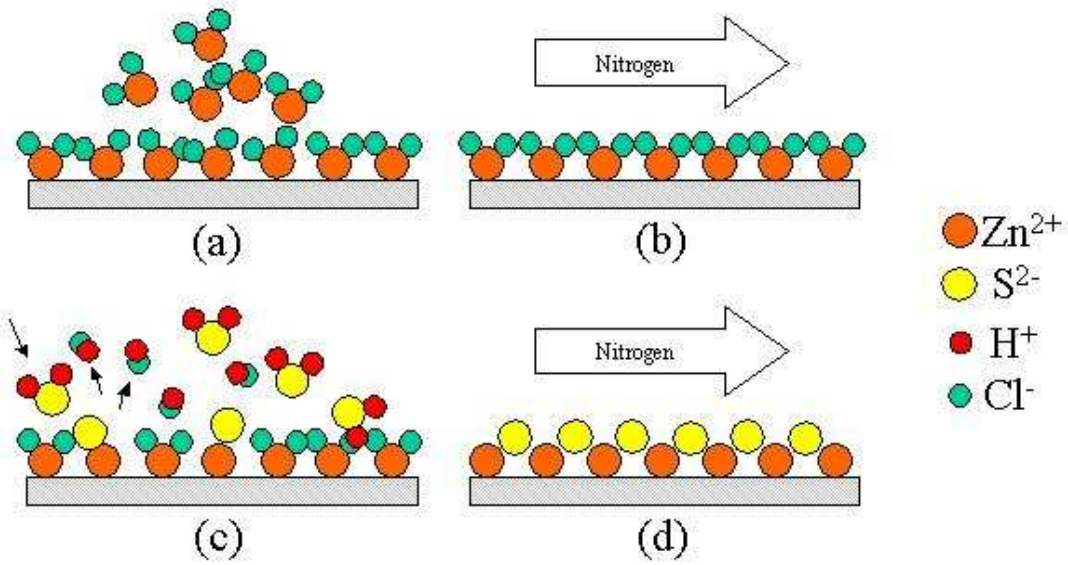

Figure 3.2 Illustration of ALD Process. Growth of ZnS from $ZnCl_2$ and H_2S is shown. (a) $ZnCl_2$(g) adsorbs to substrate (b) Nitrogen purge sweeps away excess $ZnCl_2$ (c) H_2S(g) reacts with $ZnCl_2$ to form ZnS(s) and HCl(g) (d) Nitrogen sweeps away HCl and excess H_2S

3.2 Growth Mechanisms

A critical advantage of ALD over conventional deposition techniques is that film growth is surface-controlled instead of source-controlled, as is the case with most epitaxial techniques. This is because only one molecular layer remains on the substrate after a pulse/purge sequence. ALD growth is often generalized as shown previously, for growth of ZnS from $ZnCl_2$ and H_2S, where the self-limiting growth is described in terms of chemiadsorption during each pulse. In this case, monolayer growth occurs because during a pulse, the first layer of molecules that adsorbs on the substrate has a strong interaction with the substrate (chemisorption), while any additional layer interactions are weak. Therefore, if the substrate is kept at a sufficiently high temperature, any additional weakly bound layers beyond the first will re-evaporate from the surface during the inert gas purge between pulses of the reactants. Therefore, what occurs is highly controlled film growth where one monolayer is deposited at a time with each reactant cycle.[63] It is important to point out that true monolayer growth only occurs if the materials are deposited from their elemental forms, for example from Zn and S. The reason for this decreased surface coverage is due to steric hindrance from the “extra” elements that make up the precursors, for example the Cl groups on the $ZnCl_2$ molecule. Therefore, the Zn ion cannot fully saturate the surface, yielding growth rates below one monolayer per cycle. ALD growth from tetrachlorides then yields even lower growth rates, due to increased steric hindrance.

For self-limiting growth to occur, there is a range of temperatures where ALD growth can occur known as the ALD "temperature window." This mechanism does a

good job of summarizing what is occurring, but in reality, ALD film growth is much more complicated. For example, self-limiting growth can also occur when each precursor actually reacts with chemical species on the surface, and does not simply chemisorb. If there are a limited number of reactant sites (for example, hydroxyl groups on the surface of an oxide), then self-limited growth can occur once the precursor has reacted with all available species. The surface can then be made reactive again by application of a second precursor; for example, water can react with a metal halide, forming an oxide layer, and making the surface hydroxylated again. A very important advantage that arises from this type of growth is that a much wider temperature window exists for film growth. The window is no longer dictated by physisorbed species or desorption of chemisorbed species, but is more limited by precursor vapor pressure and reactivity of those precursors at deposition temperatures. An example of a material that can be grown in this manner is TiO_2, which can be grown by ALD using $TiCl_4$ and H_2O at temperatures ranging from below 100 º C to 600º C or greater.

The films that result from ALD are high-quality and conformal, even for low length scale structures. The technique has been used to successfully grow complex multi-layered structures, such as layered Ta_xAl_yO films[64], Al_2O_3 ultra thin coatings on BN particles [65, 66], and high aspect ratio $Hf_xAl_yO_2$ coatings[67] (shown in Figure 3.3). The latter structures are the most significant to this study because they show that the necessary coating characteristics are achievable. Figure 3.3 shows that ALD is able to grow extremely thin films that remain conformal even on abrupt features like the 90 degree bend shown. This figure also shows the ability to grow nanolaminates using this process, as the layers in the image are 4 nm or less in thickness.

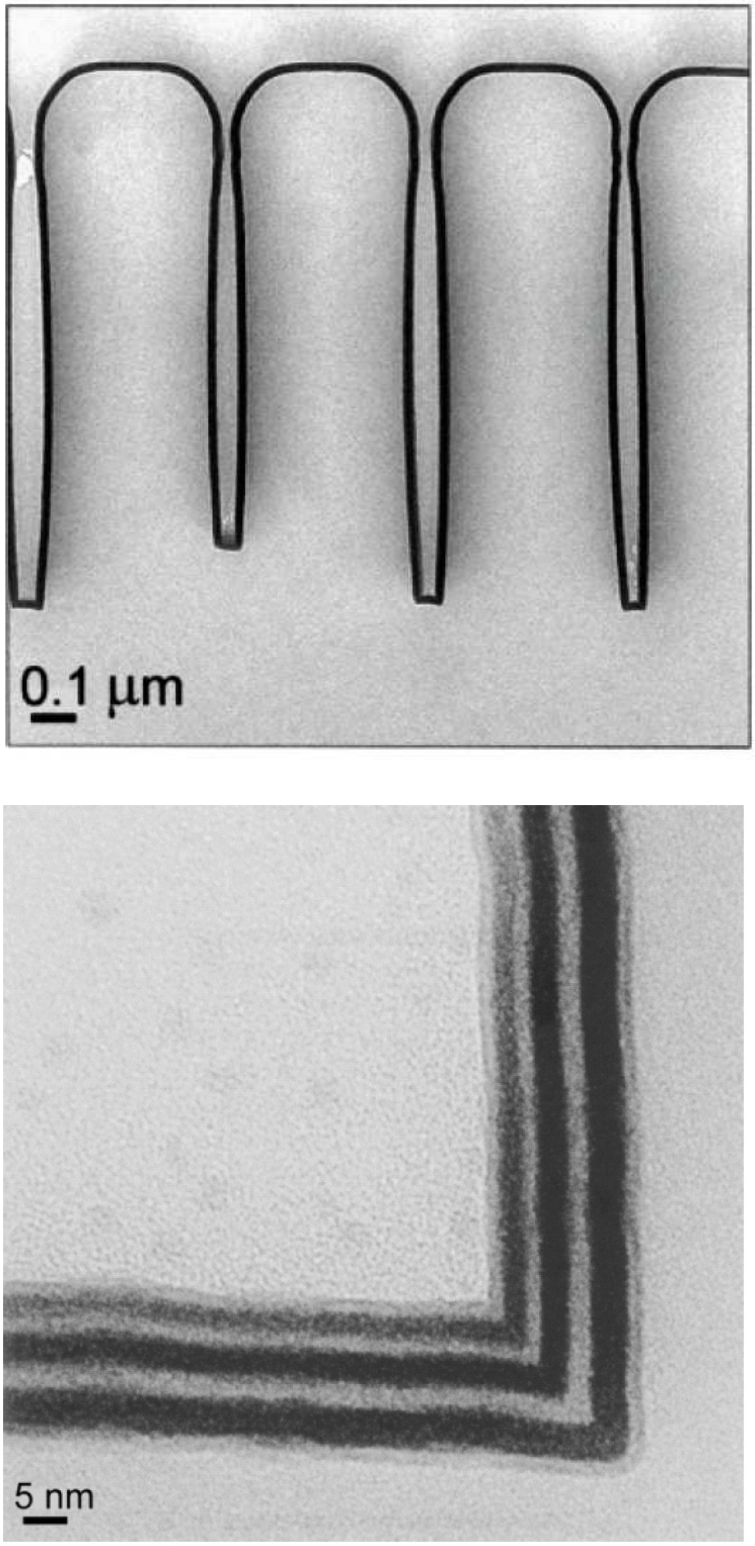

Figure 3.3 TEM images of $Hf_xAl_yO_2$ composite structure. Lower image is detail of corner.[67]

3.3 Atomic Layer Deposition Methods

There are several different forms of ALD, based on their reactant delivery methods, including Atomic Layer Chemical Vapor Deposition (ALCVD), which uses gas pulses in near atmospheric pressure conditions; High Vacuum Atomic Layer Epitaxy (HVALE), which also uses gas sources, but in HV conditions; and Ultrahigh Vacuum Atomic Layer Epitaxy (UHVALE), which uses effusion cells like those used in solid source molecular beam epitaxy (MBE), and UHV conditions. The method that was used for this work is ALCVD using a "gas flow reactor", often labeled simply Atomic Layer Deposition (ALD). In this method the precursors are delivered to the substrate as switched vapor streams with an inert carrier gas, where the same gas is used in between pulses to purge the excess reactant gas, using gas flow controls to switch on and off the pulses.[63] Gas pulses can be generated from pure gas sources, vaporization of solid sources, or boil off from liquid sources.

3.4 Materials Systems

ALD precursors can be classified into two categories, pure elements and compounds, based on the growth mechanism used. The source materials should have high vapor pressures at useful temperatures (elevated, but lower than the desired substrate temperature). For the proposed work, compounds will be used for ALD growth. Both inorganic and organometallic compounds can be used as ALD precursors. For example, in the case of GaAs growth, $GaCl_3$ can be used as well as $Ga(CH_3)_3$ as the Ga source.

The most commonly used inorganic compounds are metal halides, since they satisfy the high vapor pressure condition.[68]

ALD can be used to grow a multitude of different materials, including III-V and II-VI compounds, as well as many different metal oxides. For example, GaAs (III-V), ZnS (II-VI), and TiO_2, are all commonly grown using ALD. For this thesis, interest lies in luminescent and high refractive index materials. In order to make an inverse opal with a complete PBG, we are limited to materials with a refractive index greater than 2.8. Use of a material such as ZnS, which has a refractive index of 2.56 – 2.33 in the wavelength range of interest (400 – 700 nm) will not create a complete gap, but will create a pseudo-gap, exhibiting band gap behavior in limited directions, instead of all directions.[69] Since this material is so well understood in the ALD regime, as well as luminescent, it was used as a "proof of principle" material prior to utilization of a higher refractive index material. Titania is transparent and has an average refractive index that for 400 – 700 nm ranges from 3.2 – 2.7 from for the rutile phase, and from 2.9 to 2.5 for the anatase phase, so it is a candidate for formation of a complete PBG.[69, 70] Another candidate material was gallium phosphide, which has a refractive index of 3.44 at 550nm and 3.25 at 700 nm, with a fundamental absorption edge (band gap) at 564 nm.[69] Gallium phosphide has also been successfully grown by ALD using Ga, $GaCl_3$, or $Ga(CH_3)_3$ and PH_3 as sources. [68, 71, 72] However, these are highly toxic precursors, and would require a complex deposition tool that had safety features incorporated in it to minimize risk of exposure during normal runs or in the event of an accident. SnS_2 is a high refractive index material ($n > 3$ at 700 nm) that has been used for fabrication of infiltrated and inverted opals, but with limited success.[52] Potential ALD precursors for Sn are $SnCl_4$

and H_2S, as they have successfully been used as CVD precursors.[73] Unfortunately, the growth of SnS_2 by ALD, proved to be more complex than anticipated, and beyond the scope of this thesis. For this thesis, ZnS:Mn and TiO_2 were chosen as infiltration materials. The wavelength dependent refractive indexes of ALD grown ZnS:Mn, and the anatase and rutile phases of TiO_2 are shown in Figure 3.4.

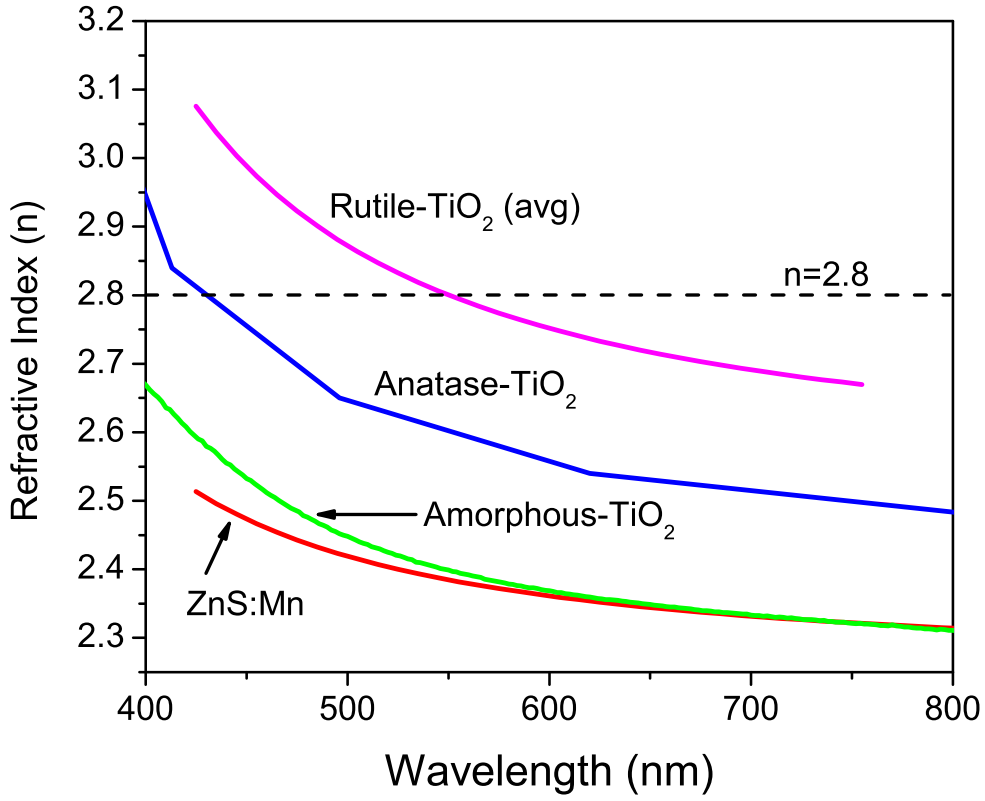

Figure 3.4 Dependence of refractive indices of ZnS:Mn and TiO_2 polymorphs on wavelength, with minimum index required for full PBG in an inverse opal indicated by dotted line. [69, 70, 74]

3.4.1 ALD Growth of ZnS:Mn

ZnS can be grown by ALD using $ZnCl_2$ and H_2S reactants, as previously illustrated in Figures 3.1 and 3.2.[75] These two reactants can combine to form ZnS via the following reaction:

$$ZnCl_2(g) + H_2S(g) \rightarrow ZnS(s) + 2HCl(g) \qquad (3.1)$$

The resulting standard enthalpy of reaction is -90.5 kJ/mol. ZnS can also be grown by ALD from the elements Zn and S, or from Dimethylzinc and H_2S:

$$Zn + S \rightarrow ZnS \qquad (3.2)$$

$$Zn(CH_3)_2 + H_2S \rightarrow ZnS + 2CH_4 \qquad (3.3)$$

However, the growth of ZnS from its halide is well studied, and allows for dopant incorporation using $MnCl_2$. This method was selected for infiltration studies described in this thesis. In this method, the substrate is first exposed to $ZnCl_2$ gas, which results in the chemisorption of a monolayer of the gas molecules on the surface such that the Zn atom attaches to the surface. For growth on oxide substrates, the Zn atom attaches itself by formation of Zn-O bonds. The substrate is next purged with nitrogen to remove excess $ZnCl_2$. Conversion to ZnS is accomplished by application of a H_2S pulse to the substrate. The H_2S gas reacts with the $ZnCl_2$, forming ZnS on the substrate, and HCl gas as a by product. This sequence results in a monolayer of ZnS, which can be repeated to precisely

grow a film layer by layer. The growth temperature is limited to above 380° C because the $ZnCl_2$ gas is provided by the vapor pressure from a heated solid precursor held at this temperature. Mn^{2+} luminescent centers can be incorporated into the film using $MnCl_2$. Similar to $ZnCl_2$, this reactant is a solid, and is placed in a hot region of the reactor in order to create a high enough vapor pressure for deposition. The $MnCl_2$ must be maintained at a temperature above 480° C to have significant vapor pressure, which pushes the deposition temperature required to about 500°C. Typical doping involves a 30 sec pulse consisting of both $MnCl_2$ and $ZnCl_2$, applied every 100 cycles. As will be reported in Chapter 5, doping of films thinner than about 20 nm requires a shorter pulse (~3 s) applied every 32 cycles. The doping sequences used yields Mn^{2+} concentrations of 1.5 – 1.7 mol %. [76] Higher or lower concentrations than this yield poor luminescence. [77]

3.4.2 ALD Growth of TiO_2

Titania can be grown by ALD from the reaction of $TiCl_4$ and H_2O liquid precursors, as first reported by Ritala, *et.al*. [78] The resulting standard enthalpy of reaction is -66.4 kJ/mol. Their work demonstrated that TiO_2 films could be grown by ALD over the temperature range of 150-600° C. The liquid precursors have sufficient vapor pressures to allow for growth as low as room temperature, and can be introduced into the reactor without using a bubbler. As previously discussed, the growth of TiO_2 proceeds by reactions between precursor and substrate, not by simple chemisorption, which allows a large temperature window for growth. Ritala found that growth at all temperatures on amorphous substrates yielded amorphous films. This data is anomalous,

however, because Alaric, *et.al* found that growth as low as 165° C showed crystallinity, and we have found the same to be true through our experiments.[74, 79] In addition, Aarik reported growth of amorphous films at 100° C that exhibited very low surface roughness.

Ideally, ALD growth of TiO_2 proceeds by the reaction of $TiCl_4$ with H_2O and hydroxyl groups through the following exchange reactions, where n = 1-3:

$$n(-OH)(s) + TiCl_4(g) \rightarrow (-O-)_n TiCl_{4-n}(s) + nHCl(g) \qquad (3.4)$$

$$(-O-)_n TiCl_{4-n}(s) + (4-n)H_2O(g) \rightarrow (-O-)_n Ti(OH)_{4-n}(s) + (4-n)HCl(g) \qquad (3.5)$$

Introduction of the $TiCl_4(g)$ to a hydroxyl covered-surface, i.e. silica, easily produces the reaction in equation 3.4, yielding a surface covered with $(-O-)_nTiCl_{4-n}$ species and HCl gas. The water pulse then reacts with these species, as in equation 3.5, releasing HCl and again leaving the surface hydroxyl covered. The hydroxyl and titanium species are strongly bonded to the substrate, so the activation energy for desorption is very high, which allows a very wide temperature window for growth. This process is illustrated in Figure 3.5.

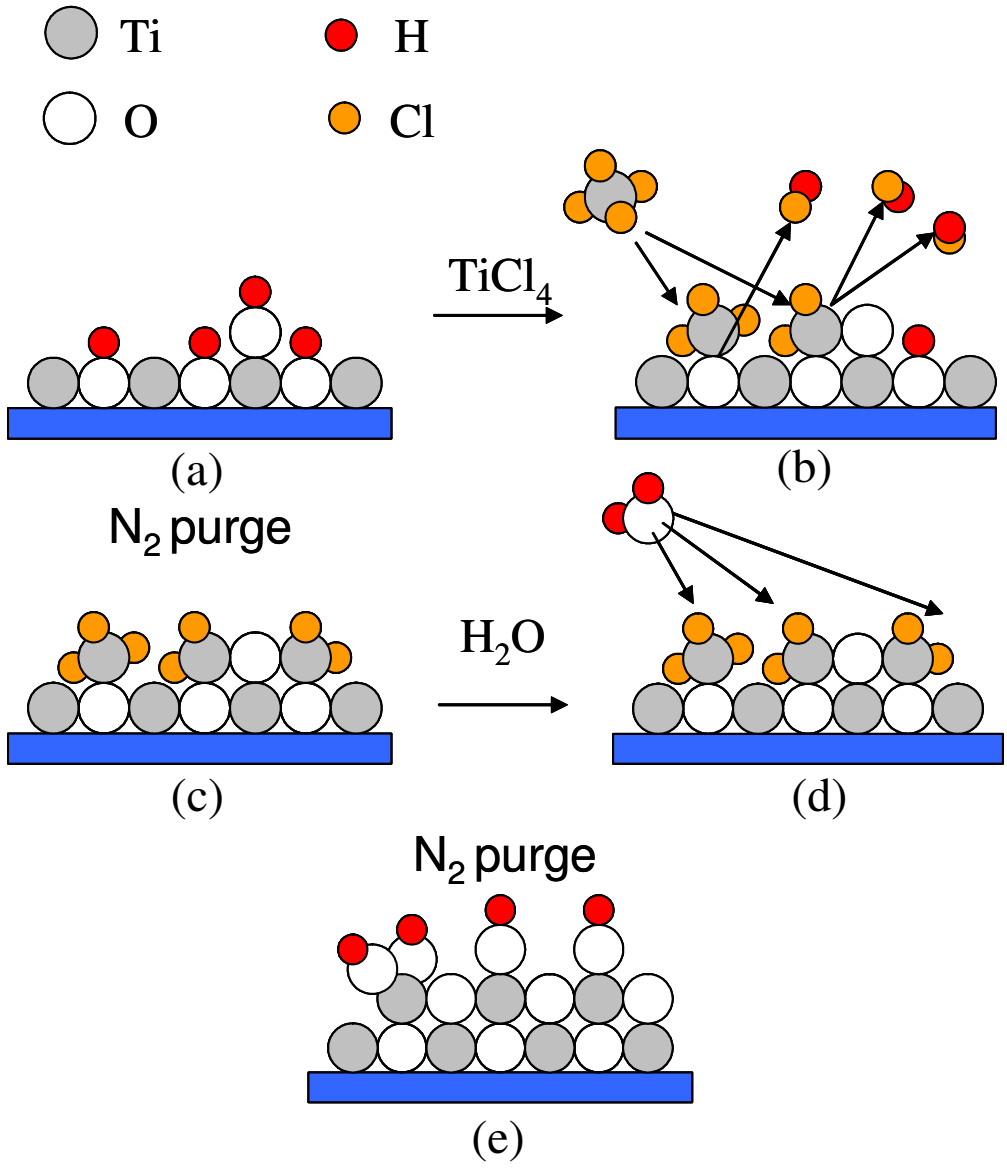

Figure 3.5 ALD growth of TiO_2 from $TiCl_4$ and H_2O. (a) initial hydroxylated TiO_2 surface, (b) surface exposed to $TiCl_4$ pulse, (c) N_2 purge removes byproducts and excess reactant, (d) H_2O pulse rehydroxylates the surface by reacting with the Cl ions, and (e) N_2 purge removes byproducts and excess reactant, leaving hydroxylated surface, ready for another cycle.

The real situation is different from the ideal mechanism, however, and the actual growth mechanism is complicated. There are many alternate reactions which can occur during deposition, and the species involved can exist in many different configurations. For example, the hydroxyl groups on the surface can react with each other, instead of reacting with $TiCl_4$ by:

$$Ti(OH)-O-Ti(OH)(s) \rightarrow Ti(-O-)_2Ti(s)+H_2O(g) \qquad (3.6)$$

or

$$2-Ti(OH)(s) \rightarrow -Ti-O(s)+-Ti(s)+H_2O(g) \qquad (3.7)$$

In addition, $TiCl_4$ can react with oxygen bridges instead of the hydroxyl groups, though this reaction is not as efficient, given hydroxyl groups are present:

$$Ti(-O-)_2Ti(s)+TiCl_4(g) \rightarrow Ti(Cl)-O-Ti(OTiCl_3)(s) \qquad (3.8)$$

Another complication arises if the HCl byproduct adsorbs on the growing TiO_2 surface through the following reversible reactions:

$$Ti-OH(s)+HCl(g) \leftrightarrow Ti(H_2O)-Cl(s) \qquad (3.9)$$

$$Ti-OH(s)+HCl(g) \leftrightarrow Ti(Cl)(s)+H_2O(g) \qquad (3.10)$$

$$Ti(-O-)_2Ti(s)+HCl(g) \leftrightarrow Ti(OH)-O-Ti-Cl(s) \qquad (3.11)$$

TiO_2 growth actually consists of all of the above competing reactions, with equations 3.4 and 3.8 leading to film growth. Each of the above reactions has a different dependence on temperature. For example, reactions 3.9 to 3.11 have equilibria on the right for low temperatures, but shift to the left for higher temperatures. Also, the dehydroxylation process illustrated by equations 3.6 and 3.7 only occurs above 180° C on the surface of anatase TiO_2. While the actual mechanisms are, in fact complicated, the reality is that for a given temperature and other growth conditions (pulse, purge length, base pressure, etc.), it is possible to attain highly conformal, surface limited growth with sub-monolayer precision. The difficulty arises when temperatures are changed, which changes the reaction balance, and as a result, the growth rate.

CHAPTER 4

EXPERIMENTAL APPARATUS AND METHODS

For this thesis, a complete process was developed for fabricating inverse opal structures, from the formation of the photonic crystal templates – the synthesis of nano-sized spheres and their self-assembly into synthetic opal structures, to their infiltration by ALD. The opal fabrication scheme involves the formation of silica sphere colloids using the Stober process, which were then used to make thin film (5 – 20 μm thick) opals on silicon, silica, ITO and TiO_2-coated substrates using a modification of the confinement cell approach. [7, 8]

For opal infiltration we utilized a unique method of fabricating inverse opal films that employs ALD for the infiltration step, a growth technique that comprises the sequential application of reactants coupled with substrate temperature optimization to achieve monolayer-by-monolayer growth[68]. As a result, growth is surface-controlled instead of source-controlled, enabling highly controllable deposition of conformal films on substrates with complex geometries[67], such as opals, or any equivalent device. Two different ALD tools were used in this work, including a commercial system, the Microchemistry, Ltd. F120, and a custom built tool designed specifically for deposition of TiO_2. Characterization methods used included specular reflectance and transmission, x-ray diffraction, scanning electron microscopy (SEM), transmission electron microscopy (TEM), atomic force microscopy (AFM), focused ion beam (FIB), and

photoluminescence (PL). The experimental methodology and apparatus is described in this chapter.

4.1 Silica Sphere Synthesis

In order to obtain a broad range of particle sizes, silica spheres were synthesized using the Stober method.[8] This method involves the ammonia-catalyzed hydrolysis of tetraethylorthosilicate (TEOS) to precipitate spheres in a solvent solution:

$$Si(OEt)_4 + 4H_2O \rightarrow Si(OH)_4 + 4EtOH \qquad (4.1)$$

$$nSi(OH)_4 \rightarrow nSiO_2 + 2nH_2O \qquad (4.2)$$

Ammonia hydroxide was used as a catalyst, and the reaction was carried out in anhydrous denatured ethanol. Control of the molar ratios of the reactants allows precise prediction of the resulting sphere sizes, as shown in Figure 4.1, which shows the dependence of sphere size on ammonia concentration in the 150 – 300 nm range. Sphere sizes were measured using transmission electron microscopy, and later confirmed by specular reflectance measurements. Calculation of percent monodispersity using TEM images is a tedious process, involving sizing of at least 100 spheres. However, it was found that the quickest way to test the quality as well as sizes of the silica spheres was to use them to make opals. It the resulting opal was poor, as evaluated from visual inspection and specular reflectivity measurements, then the batch was not used again. Since opals are comprised of close-packed arrays of spheres, Bragg diffraction results from constructive and

destructive interference of when light interacts with the sphere layers within the film. Since the diffraction peak position is dependent on the interplanar spacing, measuring specular reflectivity of the film allows the average sphere size to be calculated. This will be discussed more in depth in section 4.3.

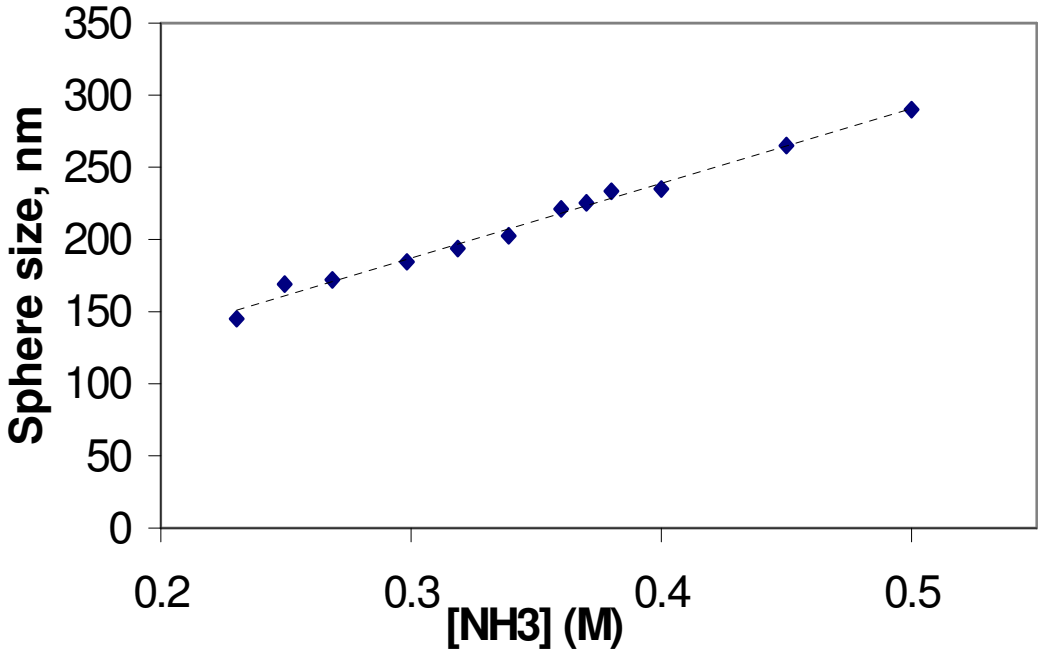

Figure 4.1 Sphere size as a function of ammonia concentration, for silica sphere synthesis using the Stober method.[8]

4.2 Fabrication of Thin Film Opals Using the Modified Confinement Cell Technique

A modified confinement cell method was used to fabricate thin film opals on both silicon and quartz substrates.[7] Using this method, opals useful for infiltration studies can be formed in 24 hours. Higher crystalline quality films can be formed in several days, to several weeks, depending on the colloid sphere size. The technique involves the injection of a colloidal solution into the space between two substrates defined by a "gasket" or "confinement cell", which allows for growth of a thin film opal of controlled thickness. This technique was chosen because it is relatively fast and allows uniform growth of high quality opals. It also makes "doping" of the opal possible by incorporation of spheres other than silica, which will allow formation of microcavities in the future.

The confinement cell designed by Park and Xia was formed from positive photoresist.[7] Using photolithography, shallow drains (~100 nm deep) were defined in the top walls of a square "cell" made of resist on top of a glass slide. After first defining the shape of the cell using a square mask, these drains were defined by exposing the top wall through a mask comprised of narrow slits, oriented perpendicular to the wall. To make the drains shallow, a very short exposure time was used (~ 5 sec.). The result is that the photoresist is not exposed very deep, so when placed in developer, only a small amount of resist is removed. However, there are several drawbacks to this technique. For example, we found it nearly impossible to define drains only 100 nm deep. The resulting drains usually had very rough cross sectional profiles, and were 500 nm to 1 micron in depth. In addition, the cell must be used (for opal growth) on the substrate that the lithographic steps were performed on. The cells also proved to be quite fragile, and often would dissolve during the opal deposition, since they were formed from positive resist,

which has low physical strength and low chemical resistance. Since they are so fragile, and because they could not be transferred to other substrates, it was clear that these cells could only be used once.

The process of Park and Xia was improved upon by switching to an epoxy-based negative photoresist. In negative resists, the area exposed by UV light is cross-linked, therefore it is the area that remains after developing. Instead of using short exposure times to define a quite shallow drain, a substrate was physically patterned with a thin layer of evaporated aluminum, creating a template. The number of processing steps increased, but the benefits of this technique outweigh the negatives. First, positive resist was spun onto a glass slide. Next, a mask consisting of many parallel lines was used to define 0.100 mm wide trenches in a square shape. The surface was next coated with 150 nm of aluminum using evaporation coating. Using a liftoff process, the photoresist and excess aluminum was removed, leaving a square frame of 150 nm thick aluminum lines, as shown in Figure 4.2. The square frame that results now can be used as a template to pattern a robust epoxy-based gasket. Negative photoresist was next spun onto the substrate. Variation of spin speed allowed changing the gasket thickness from 2 - 20 μm. The gasket itself was next defined by a mask comprised of a square-shaped frame, as shown in Figure. After developing the exposed substrate, a robust epoxy gasket remained, on top of the aluminum lines. Next, simply placing the coated substrate in water allowed removal of the gasket without damaging the metal lines. The aluminum template could then be re-used to form another gasket, and more importantly, the gasket could be transferred to any desired substrate for opal growth. These fabrication steps are illustrated in Figure 4.3, and Figure 4.4 is a photograph of the resulting epoxy gasket.

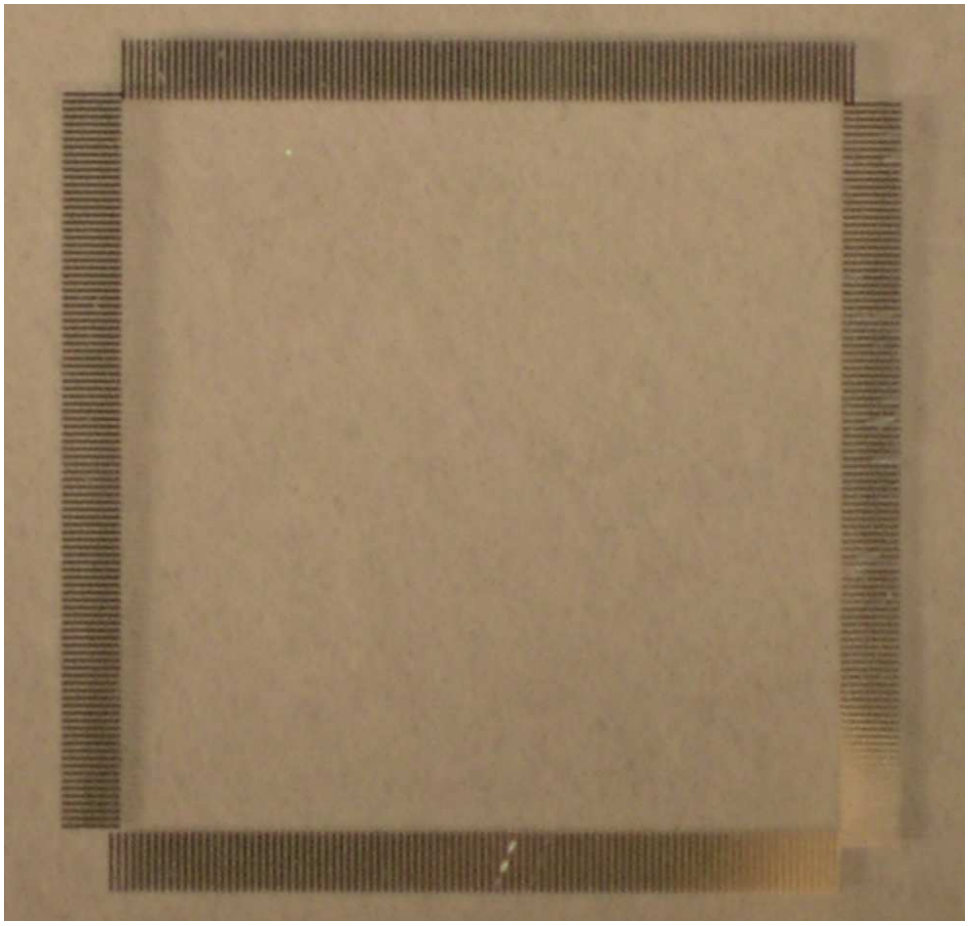

Figure 4.2 Aluminum line template used to define drains in the underside of the epoxy gasket.

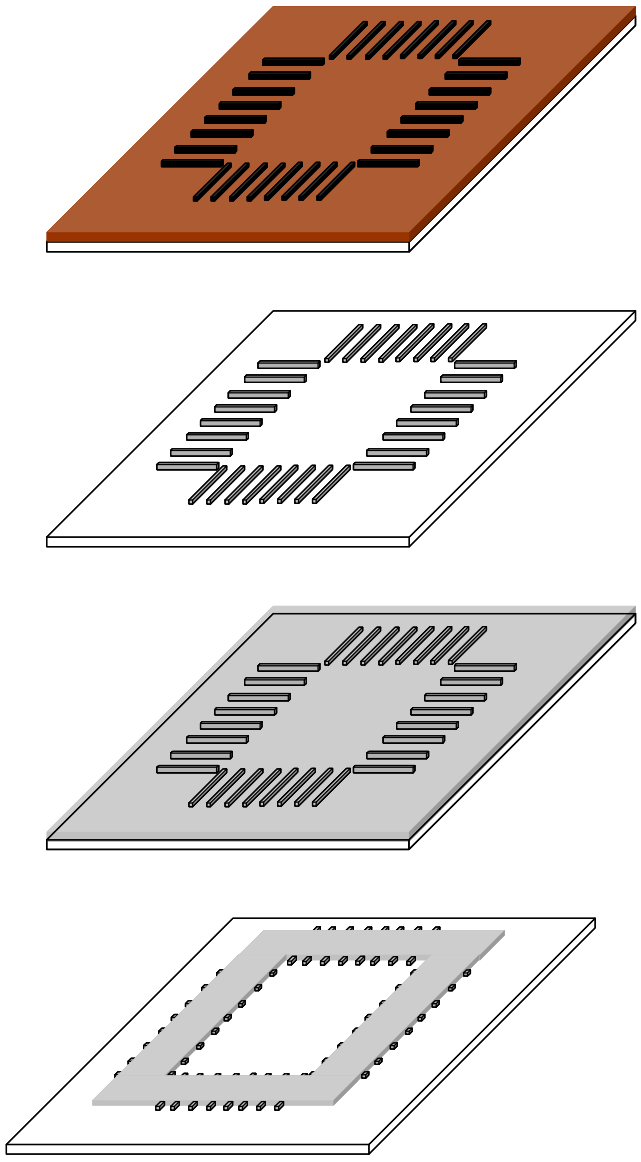

Figure 4.3 Gasket fabrication sequence. Top to bottom: Aluminum line definition, resulting template after liftoff, negative resist spun onto template, expose gasket shape and develop, yielding rectangular frame with 150 nm drains on underside.

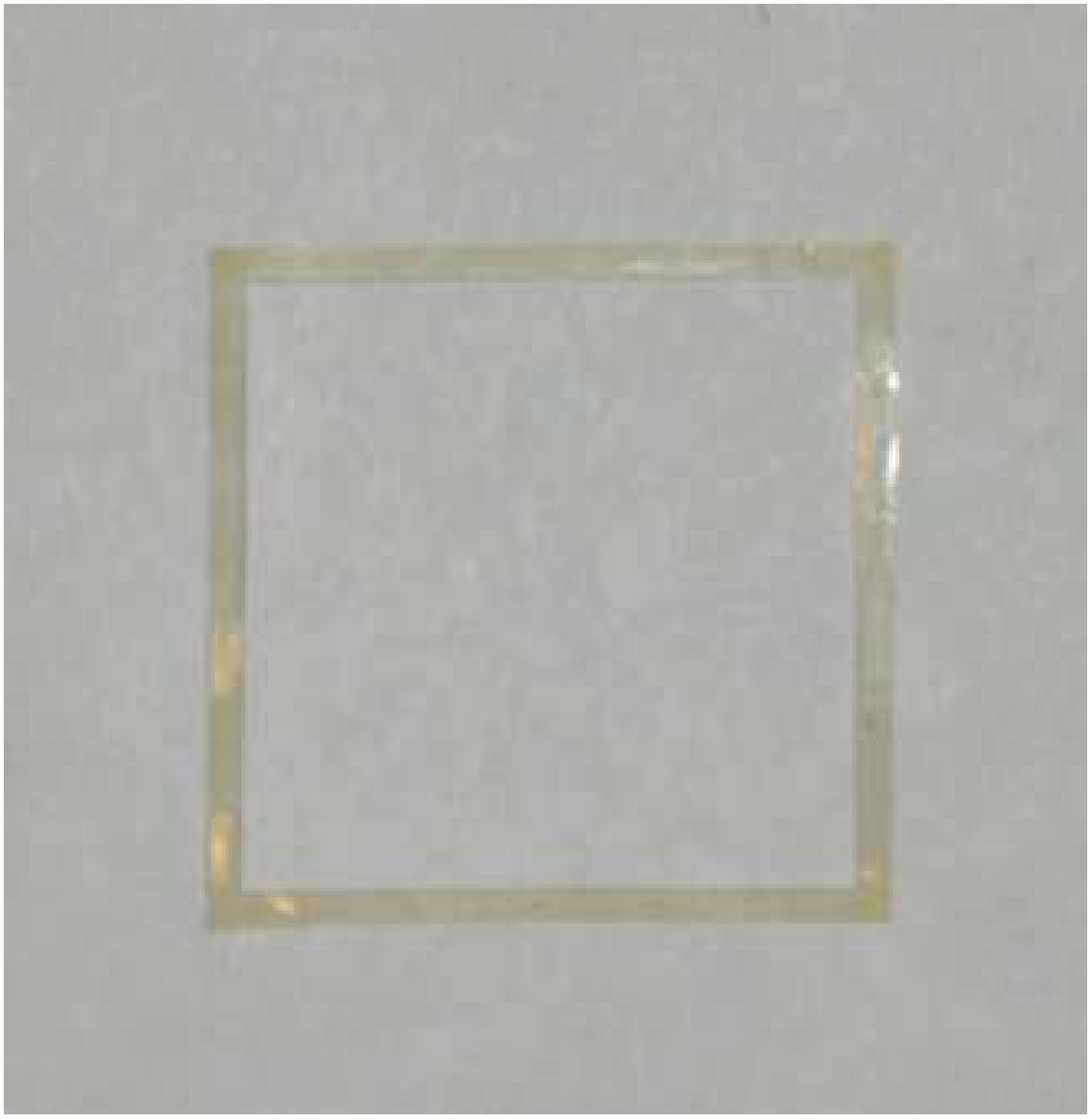

Figure 4.4 Resulting epoxy gasket used for opal fabrication.

To grow an opal, a gasket was placed on the desired substrate (quartz or silicon), and covered with a glass top. The glass top had a hole drilled in it, and a tube attached the top, allowing injection of colloidal solution into the cavity. This glass top was treated with a fluorination coating that renders the surface hydrophobic, to allow for cell disassembly without damaging the opal. Figure 4.5 is a schematic of the confinement cell, and a photograph of an assembled cell.

The cell was next filled with a colloidal silica solution, pressurized at 3 psi, and placed on a vibration stage. This vibration stage consisted of a metal plate attached to the cleaning basket of an ultrasonic cleaner, as shown in Figure 4.6. A manifold was used to deliver multiple gas lines to the system, so that up to six opals could be deposited at a time. Depending on the sphere concentration (10^{-1} - 10^{-2} g/ml) in the colloidal solution, the cell filled with opal in as little as 1 day. After the cells filled, the opals were dried in air, and the cell was disassembled, leaving a 10 micron thick opal film. Finally, the films were sintered in a box furnace at 700 – 800 ° C for 2 hours. Figure 4.7 shows an SEM image of the top surface of a silica opal grown in the confinement cell. The image shows the surface of the film, clearly a (111) plane. The confinement cell method results in films oriented with the (111) plane parallel to the substrate.[7] Figure 4.8 shows a SEM image of a fractured opal cross-section. The fracture surface is faceted with close packed planes, and the resulting geometry, relative to the (111) planes on the surface of the opal confirm that the opal exhibits FCC ordering throughout the film. Hexagonal close-packed crystals (HCP) only have one set of close packed planes (the basal plane), so the fracture surface would not contain close packed planes if the film were HCP, whereas FCC crystals have four intersecting close-packed planes angled 70.5 degrees apart, so a

fracture surface perpendicular to the (111) surface plane should cleave along close-packed planes, as observed in Figure 4.8. The specular reflectance spectra of the resulting films were measured, allowing for calculation of the effective lattice constant of the opals due to Bragg diffraction from the (111) planes. The calculated values agreed well with the sphere sizes obtained from TEM analysis. The observed growth of the close-packed planes parallel to the substrate is due to both the proclivity of close packed phases to nucleate on flat surfaces, and to the effect that shear stress has on ordering within the cell.[80, 81] When an ordered colloidal crystal phase flows, or has shear applied to it, the close packed planes align parallel to the shear direction.[81] The flow of the colloidal solution in the confinement cell is parallel to the substrate, and the growing crystalline film also experiences shear stress due to the flow of the water through the cell, resulting in close-packed planes on both the top and bottom of the opal film.

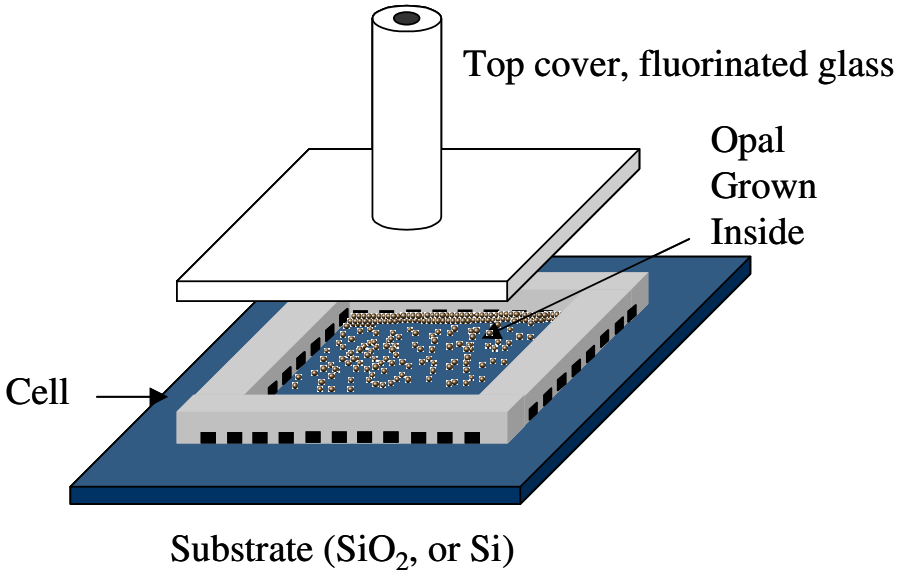

(a)

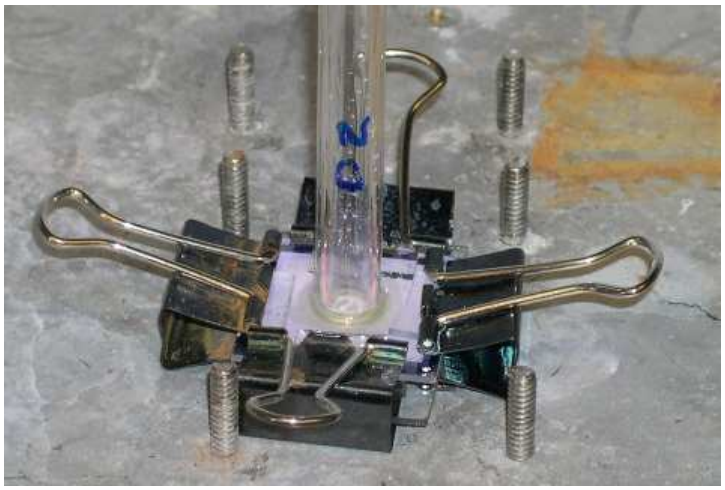

(b)

Figure 4.5 Confinement cell used for opal fabrication. (a) illustration of cell assembly and (b) assembled cell, held together with metal binder clips.

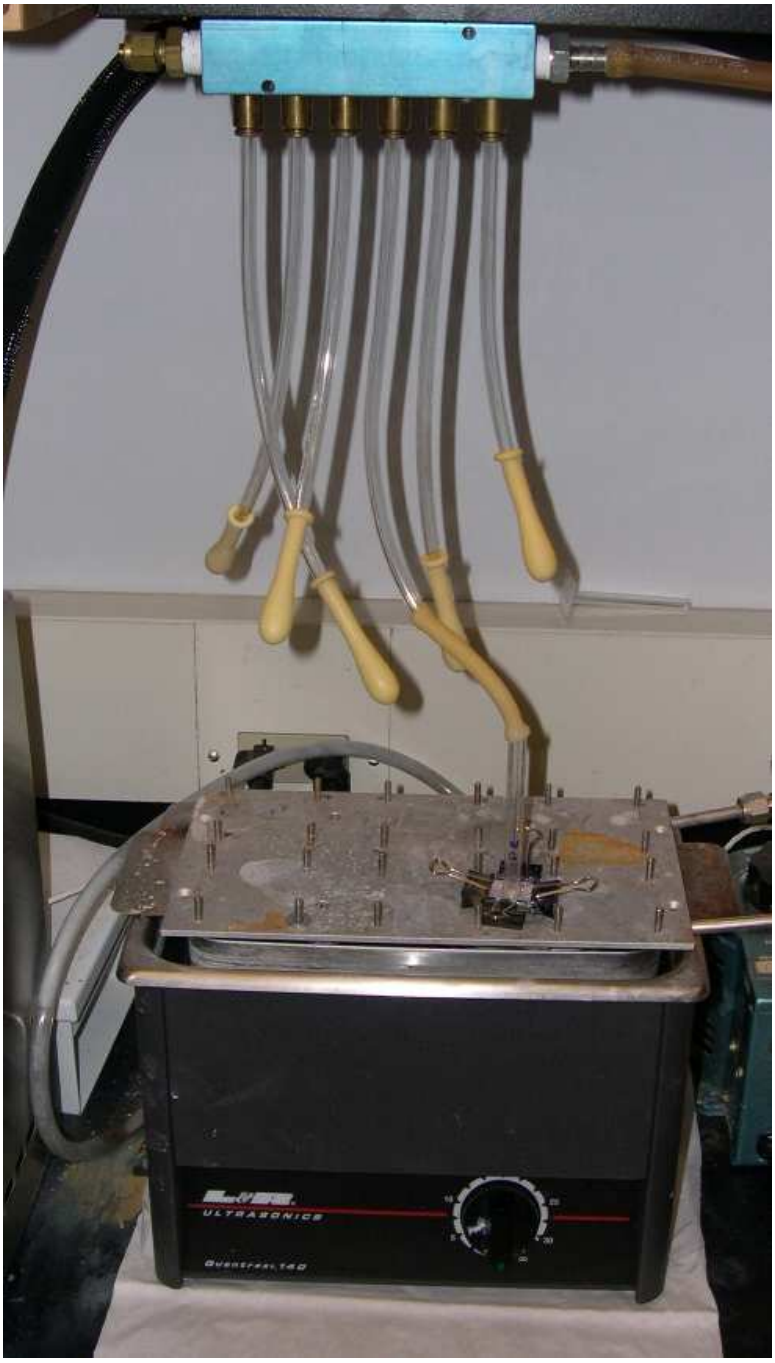

Figure 4.6 Opal deposition stage, including ultrasonic cleaner, assembled cell, and gas delivery system.

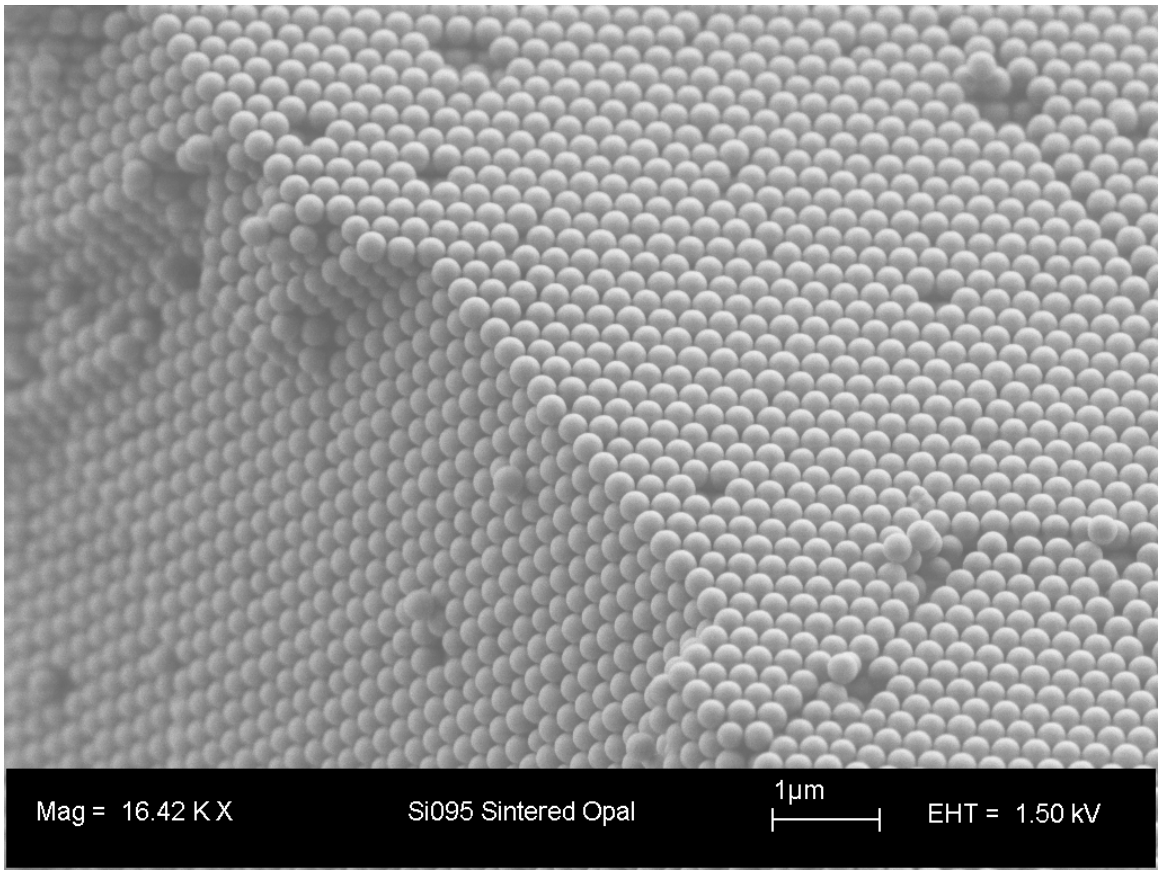

Figure 4.7 200 nm sintered silica opal fabricated using confinement cell technique.

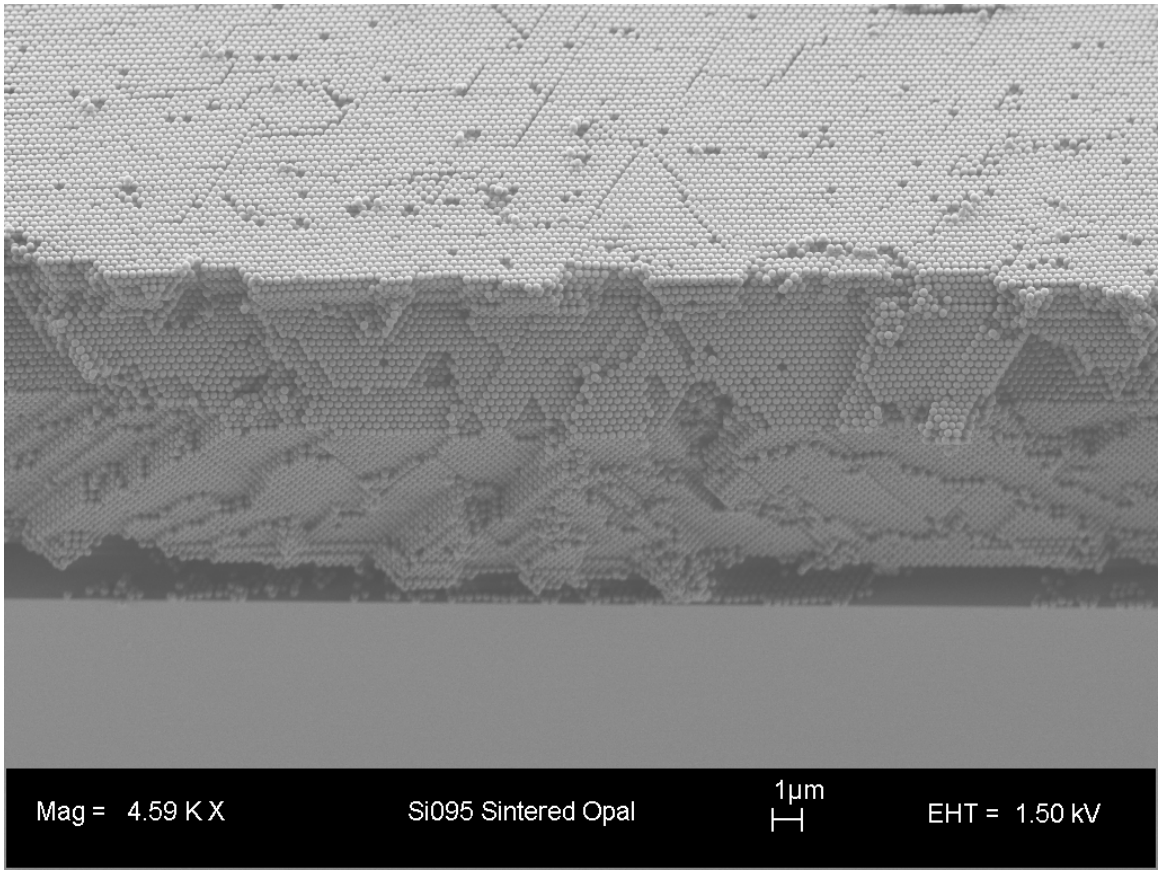

Figure 4.8 Cross-section view of 200 nm sintered opal fabricated using modified confinement cell. (111) fracture planes are evident on the cross-sectional face, confirming that crystal structure is FCC.

4.3 Optical Characterization of Opal-based Photonic Crystals

The photonic band structure of photonic crystals was probed by reflectance and/or transmission measurements over the wavelength ranges of interest. The oriented films that result from confinement-cell grown opals allow characterization of the Bragg peaks that are a result of optical diffraction from the (111) planes. While it is simple to consider this peak as simply Bragg diffraction, it is also a feature that arises due to a photonic band gap in the Γ-L direction, which is the (111) direction in an FCC crystal. A photonic band gap that exists in at least one direction, but not in all directions, is often called a pseudo photonic band gap (PPBG). The calculated photonic band diagram for a silica opal is shown in Figure 4.9, with the PPBG labeled. If we were to consider only diffraction, we can only know the position of this peak, and we would expect that the only reason for this peak to have any measurable width should be due to peak broadening from a number of sources, including the measurement equipment, lattice constant variation in the opal due to some degree of polydispersity of the spheres, defects, or polycrystallinity of the film. We know from calculation of photonic band diagrams that as the dielectric contrast in opal-based structures increases, the Γ-L band gap not only shifts to higher wavelength, but also widens. However, it is useful to compare the peak position to simple diffraction, because it allows a quantification of the a number of parameters, including the starting opal lattice constant and the filling fraction that results from ALD infiltration of the opal.

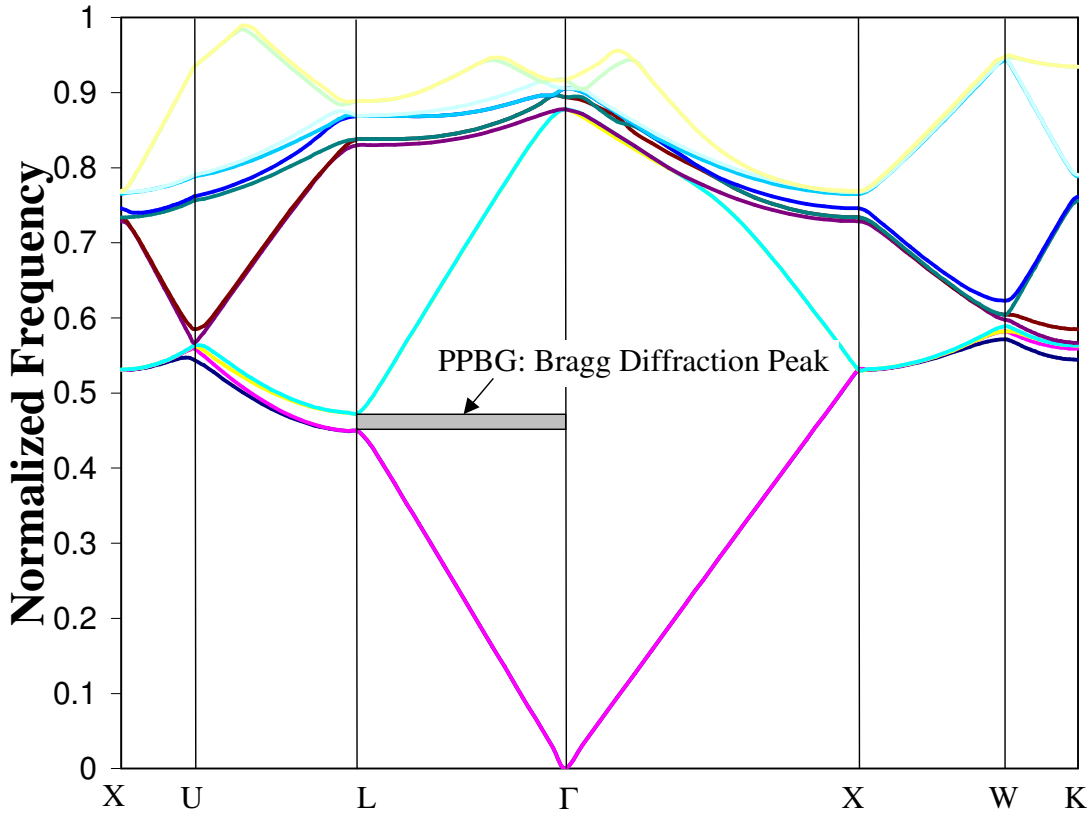

Figure 4.9 Photonic band diagram for a silica opal, with Γ-L PPBG labeled. (Filling fraction of silica= 74%, index of refraction 1.45)

A derivative of the Bragg law allows first order calculation of the primary peak position in a (111) oriented opal-based structure using the following equation, where ε_{avg} is the average dielectric constant, d is the sphere size, and θ is the angle of incidence:

$$\lambda = 2d0.816\sqrt{\varepsilon_{avg.} - Sin^2\theta} \qquad (4.3)$$

Opals grown by the confinement cell method exhibit face-centered-cubic (FCC) arrangement of the silica spheres. Since FCC packing results in a 74% dense structure the average dielectric constant of the opal can be calculated. From equation 4.3, given a known refractive index for SiO_2, the average sphere size for the opal film can be found by identifying the position of the Bragg peak based on reflectivity or transmission data. This peak position changes as the angle of incidence changes, as illustrated by Figure 4.10, which shows the change in reflected color from the surface of 266 nm opal as the viewing angle shifts from normal to ~ 45°. After infiltration, the average refractive index will change based on the filling fraction, *f*. The filling fraction is defined as the fraction of the opal that the material of interest represents. For example, the theoretical maximum amount of infiltrated material is equal to the volume of the FCC interstitial space, which is 26% of the opal volume. The resulting average dielectric constant after infiltrating is therefore:

$$\varepsilon_{avg} = \varepsilon_{Silica}0.74 + (0.26 - f)\varepsilon_{air} + f\varepsilon_{ZnS} \qquad (4.4)$$

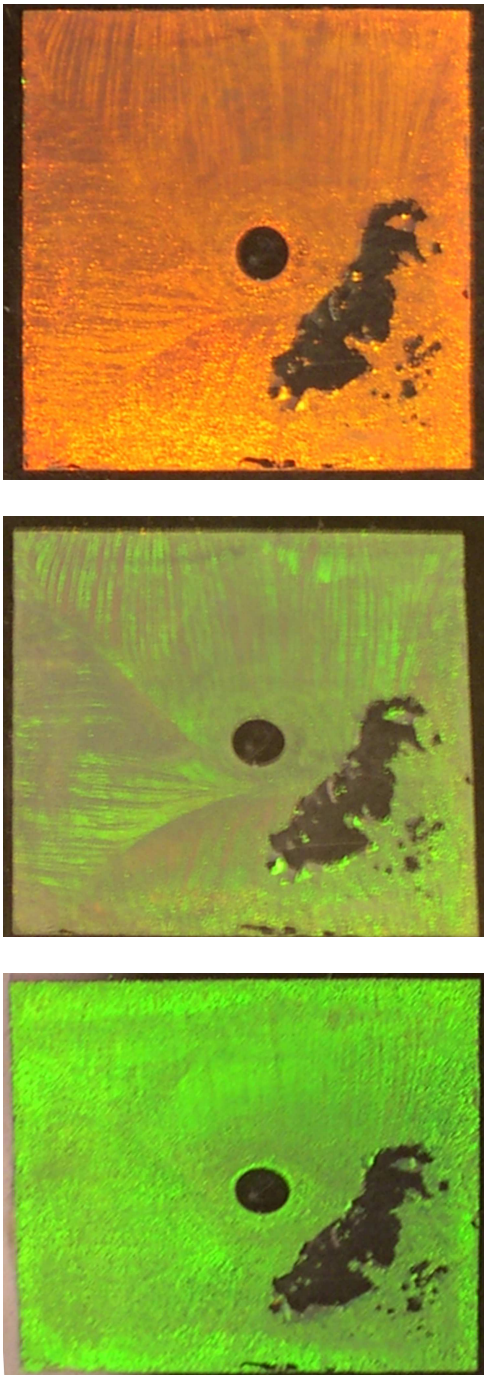

Figure 4.10 Digital camera images of 266 nm opal, illustrating reflected color change as viewing angle was increased. Top image was taken normal to opal surface, middle ~ 22.5 ° from normal, and bottom ~ 45°. Opal size is 2 cm x 2cm.

For infiltrated opals, f is unknown, but the sphere size is known from prior measurements, so combining equations 4.3 and 4.4 allows the calculation of f based on calculation of the average dielectric constant from the shifted Bragg peak position:

$$f = \frac{\varepsilon_{avg} - \varepsilon_{silica}(0.74)) - 0.26}{\varepsilon_{ZnS} - 1} \qquad (4.5)$$

The resulting percent infiltration can be calculated by dividing the calculated filling fraction by the theoretical maximum filling fraction: 26% in the case of FCC opals. In this thesis, filling fraction and percent infiltration are treated as equivalent, and are always quoted as the fraction of the available pore volume filled. Since ALD is a highly conformal growth technique, 100% infiltration of the opal is not possible, and small air pockets should remain in the FCC tetrahedral and octahedral interstitial sites, which has, in fact been predicted to enhance the width of the PBG by as much as 100%.[82] If the size of the available pathways for gas transit into the opal are considered, the smallest dimension is the space between the spheres in a close-packed plane, which will close when the coating thickness reaches 7.75% of the diameter, as illustrated in Figure 4.11. In TiO_2 and multilayer experiments, this value was used to determine the number of ALD cycles needed for different opal sizes. To compare theoretical with experimental filling fractions, Monte Carlo calculations were performed, simulating the filling of the opal with different thickness spherical shells, which revealed that the 7.75% coating thickness corresponds to ~ 86% filling of the void space, as shown in Figure 4.12.[83] In addition, these simulations also allowed comparison of filling fractions with calculated band diagrams.

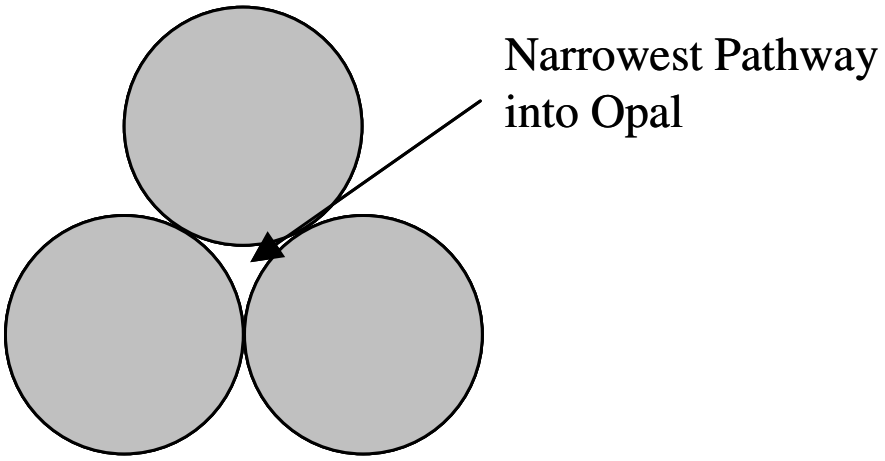

(a)

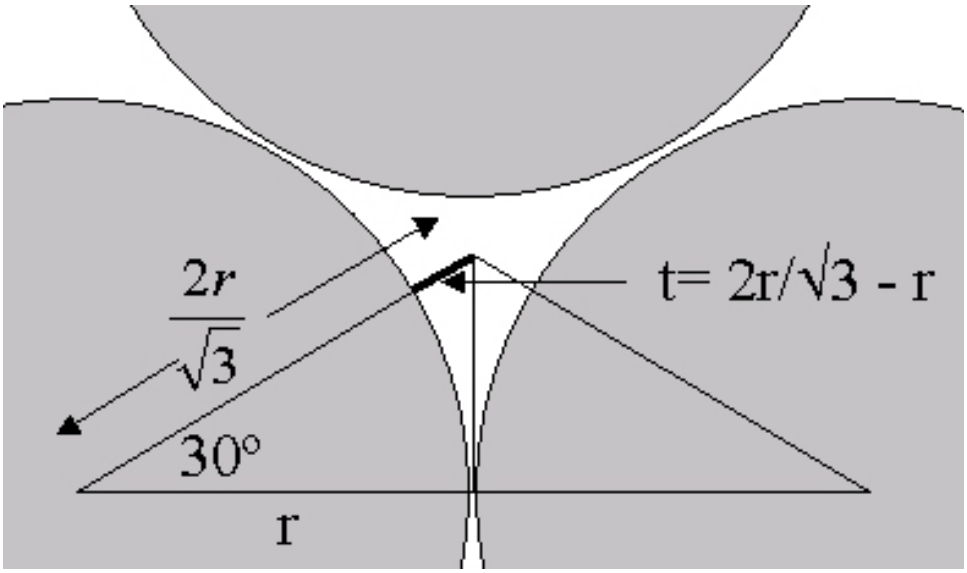

(b)

Figure 4.11 (a) Illustration of narrowest pathway for gas transit into an opal and (b) pathway geometry, showing maximum coating thickness value.

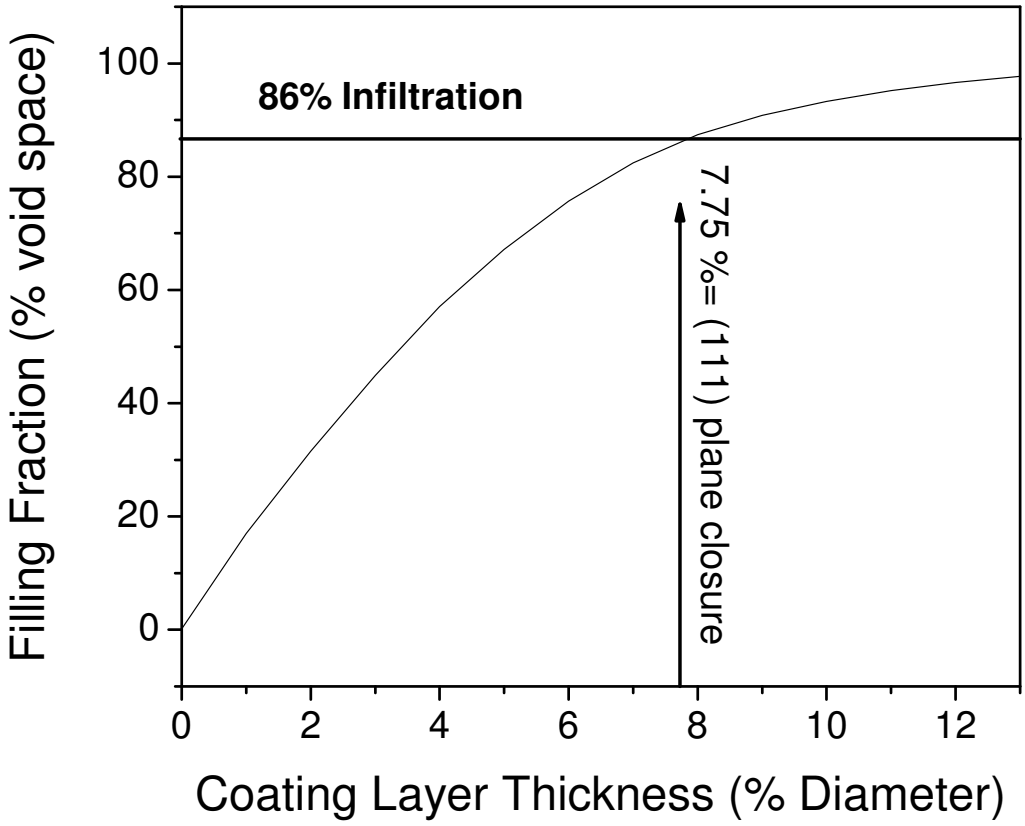

Figure 4.12 Monte Carlo calculation of filling fraction as a function of infiltration layer thickness.[83]

4.3.1 Specular Reflectance and Transmission Equipment

A Beckman DU640 UV-vis spectrophotometer was used for measuring reflectivity and transmission of opals, infiltrated opals, and inverse opals, as shown in Figure 4.13. This system has both xenon and halogen lamps and is capable of measuring wavelengths from 190 to 1100 nm. For reflectivity measurements, a Harrick Scientific variable angle specular reflectivity accessory was used, as shown in Figure 4.14, mounted in the spectrometer. Near-normal measurements were collected at 15° incidence.

Figure 4.13 Beckman DU640 UV-vis spectrophotometer

Figure 4.14 Variable angle specular reflectivity adapter for spectrophotometer

4.4 Photoluminescence Measurements

Photoluminescence measurements were performed on two systems. The first system was a Jobin-Yvon Spex "Fluorolog" system located at the U.S. Army Research Laboratories in Adelphi, MD, which allowed for continuous wave excitation of phosphors. The second system was a custom assembly that consisted of a pulsed nitrogen laser excitation source and a monochromator combined with a photomultiplier detector. All measurements were performed at room temperature.

4.4.1 Spex Fluorolog Spectrofluorometer

This PL system was based on a lamp excitation source, monochromators, and a cooled photomultiplier tube detector all integrated in a standalone unit. The excitation source consisted of a 450 watt xenon lamp. The lamp output was passed through an excitation monochromator to select the proper excitation wavelength, the output of which was then directed to the sample at normal incidence. The PL output from the sample was collected at 22.5 degrees from normal incidence by an emission monochromator, after passing through a 400 nm high pass filter to remove any stray UV light. The output of the emission monochromator was directed into a cooled photomultiplier tube, the output of which was collected by computer.

Angular dependent PL was measured using this system, combined with two fiber probes. One probe collected the output of the excitation monochromator and directed it to the sample surface at ~ 45° incidence, and the other probe was used to collect the PL at different angles and send the signal back to the emission monochromator. These probes

were used outside of the normal sample holder portion of the spectrofluorometer. The geometry of the angular dependent PL setup is shown in Figure 4.15.

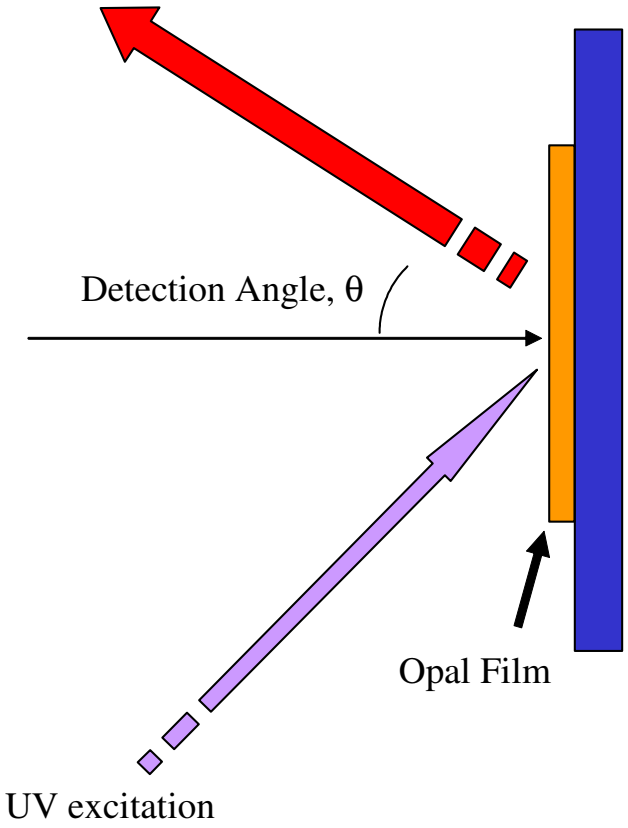

Figure 4.15 Geometry of angular dependent photoluminescence measurements.

4.4.2 Pulsed Excitation System

For measurement of PL from partially infiltrated ZnS:Mn opals and ZnS:Mn/TiO_2 multilayer opals, a pulsed laser PL system was used. This system consisted of a Laser Physics LN1000 nitrogen laser, a sample holder, fiber collector, an Acton Research Spectra Pro 500i emission monochromator, and a Hammamatsu photo sensor module. The photo sensor was a cooled GaAs photocathode-based photomultiplier tube, with sensitivity from 380 - 890 nm. The nitrogen laser output was 600 psec. 2 MW (max) pulses of 337 nm UV light with a maximum repetition rate of 20 Hz. The laser was triggered externally using a Spiricon Chopper Sync II. This trigger signal allowed use of a EG&G 5208 2 phase lock-in amplifier. The samples measured were excited at 45° incidence, and the resulting emission was collected at normal incidence using a collimating lens coupled to an Acton Research fiber probe using the setup shown in Figure 4.16.

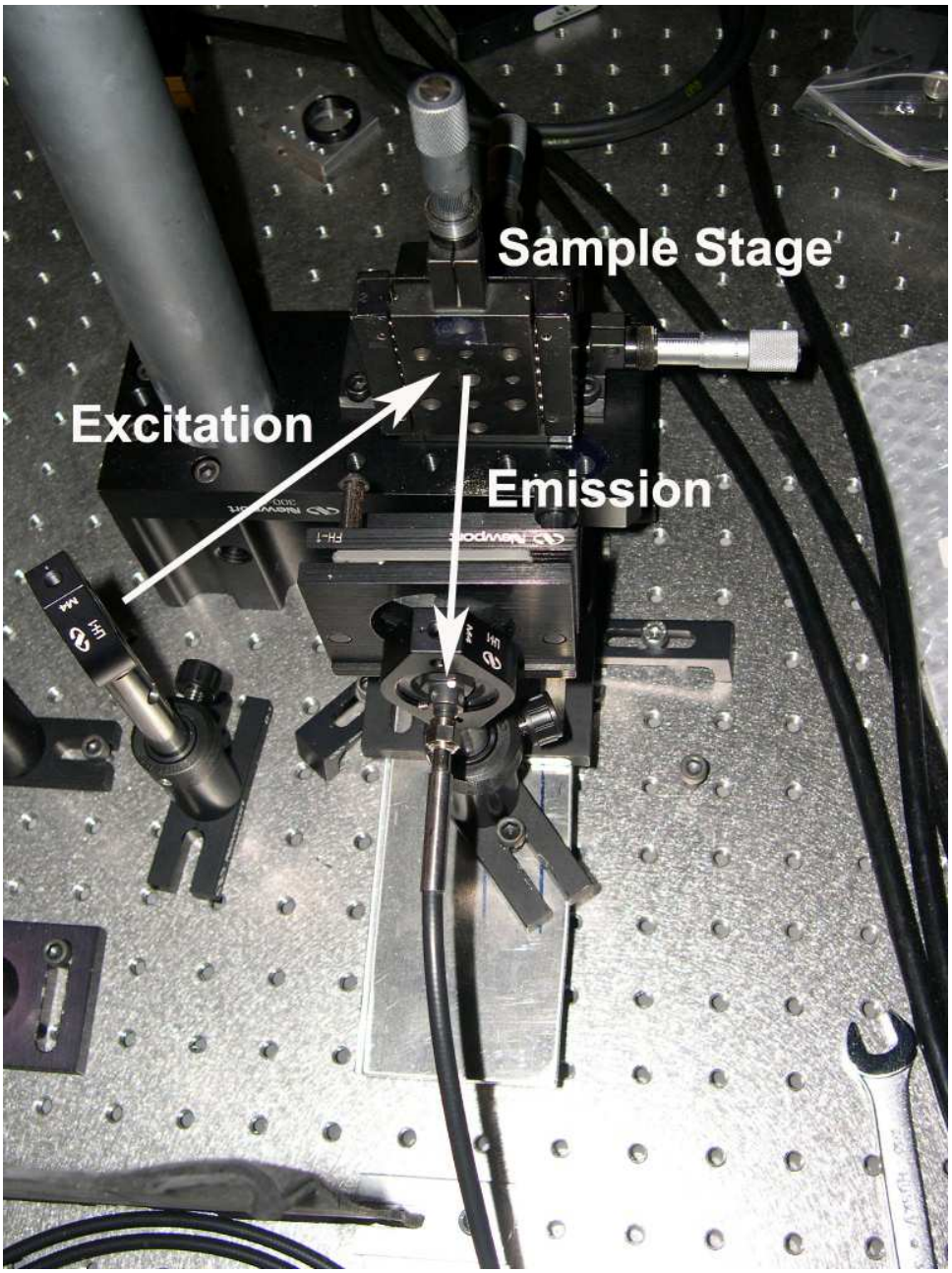

Figure 4.16 Photoluminescence measurement setup for pulsed nitrogen laser excitation.

4.5 Other Experimental Techniques

All SEM images were acquired using a LEO 1530 scanning electron microscope. Surface roughness was calculated from images acquired using a Park Scientific Instruments Autoprobe CP atomic force microscope operating in contact mode. X-ray diffraction data was acquired using a Philips diffractometer. Infiltrated opals were milled using a Gatan 600 Duomill Ar^+ mill, operating at 4 KV with a 0.5 mA specimen current, with 15° angle of incidence. Photonic band diagrams were calculated using the plane wave expansion method (using MIT's MPB program), or by the finite difference time domain method using custom designed code. [24, 84]

4.6 Opal Infiltration Equipment

4.6.1 Commercial ALD System: Microchemistry, Ltd. F120

The F120 ALD tool produced by Microchemistry, Ltd. was used for deposition of all ZnS:Mn films, and for preliminary infiltration studies of TiO_2 infiltrations. This system is located at the US. Army Research Laboratories located in Adelphi, MD. Figure 4.17 is a photograph of the reactor, viewed from the reactant delivery direction. The green cables are the thermocouple connections for monitoring the temperature at various locations within the reactor. The metal box on the top is the furnace containing the reactor tube. Figure 4.18 shows the inside of this box from the top, showing six heating zones along the length of the box. These heating zones allow selectivity of solid source reactants, and the substrate temperature. The reactor is capable of supplying 6 different precursors during a run. The reactor is divided in half, with three delivery tubes per side,

which means that three different sets of precursors can be used. For example, during deposition using a two reactant deposition, the reactants must be located on opposite sides of the reactor. Solid source reactants are used by placing them in the delivery tubes, in the appropriate temperature zone, as illustrated in Figure 4.19, which is a schematic of the reactor, detailing events that occur during a reactant pulse. Liquid sources and gas sources can also be used by connecting the source directly to the delivery tube. Thermoelectric cooling allows liquid precursor temperature control.

ZnS:Mn was grown in this reactor at 500° C using a $ZnCl_2$ solid precursor, and H_2S gas. Pulse lengths ranged from 220 msec. to 2.2 sec., and purge lengths ranged from 550 msec. to 2.2 sec., and vacuum levels within the reactor were approximately 1 torr. Nitrogen flow rates during purges were 1000 sccm. Mn^{2+} doping was accomplished using a $MnCl_2$ solid precursor. A doping pulse that consisted of both $ZnCl_2$ and $MnCl_2$ was applied to the film every 100 ALD cycles for films thicker than 30 nm, and every 32 cycles for thinner films.

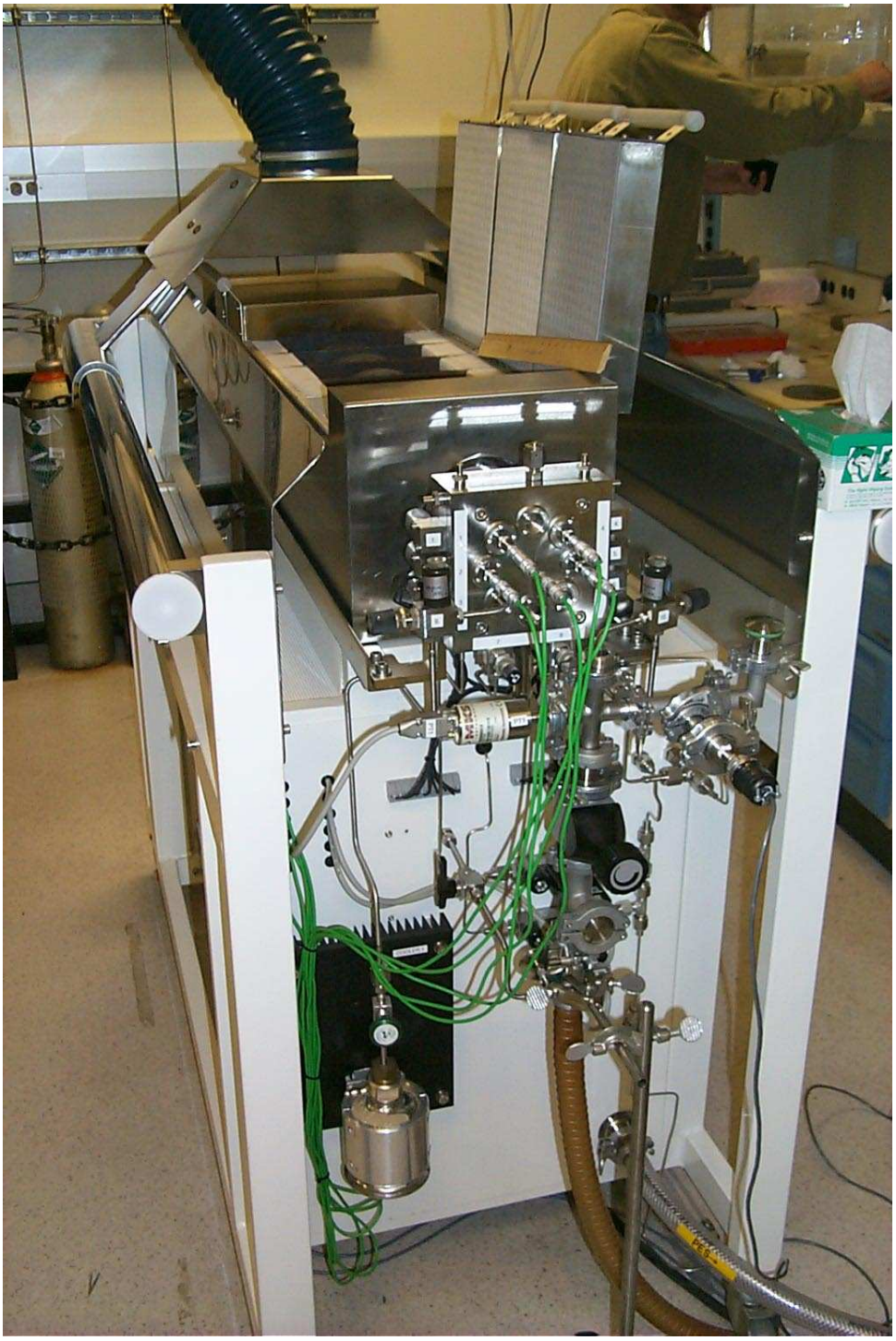

Figure 4.17 Microchemistry, Ltd. F120 ALD reactor

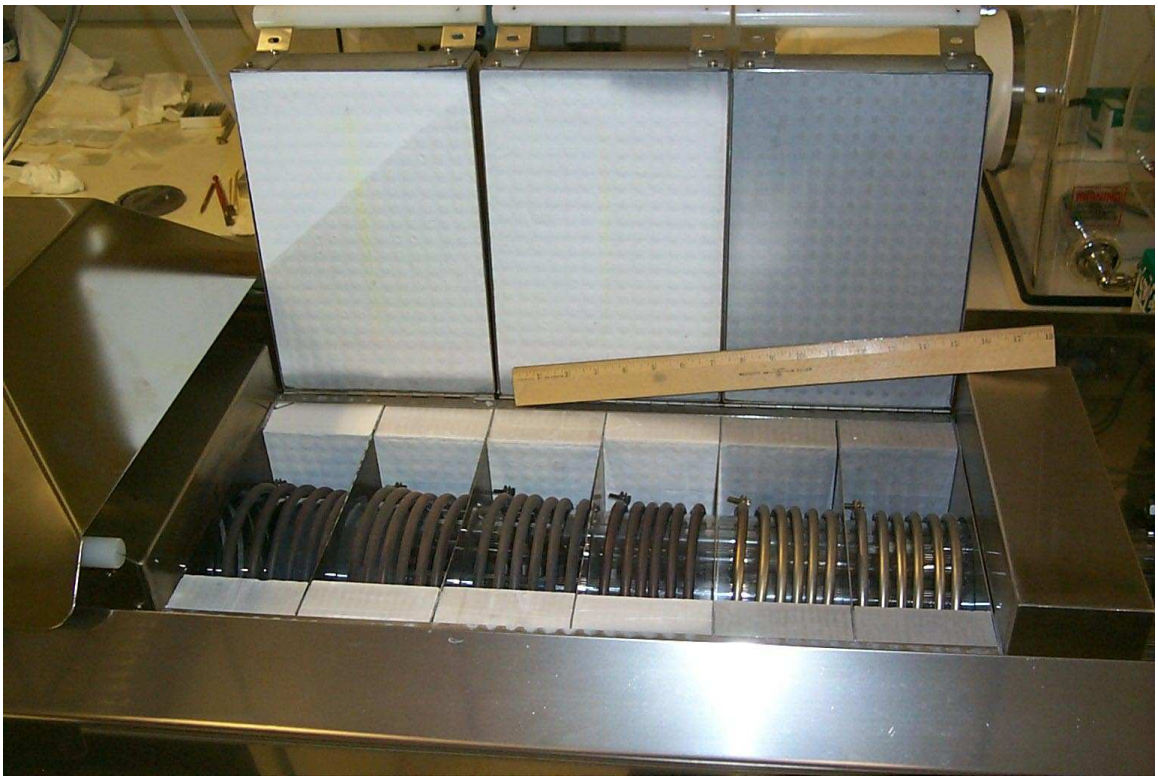

Figure 4.18 F120 ALD reactor, with furnace section open, revealing six temperature zones.

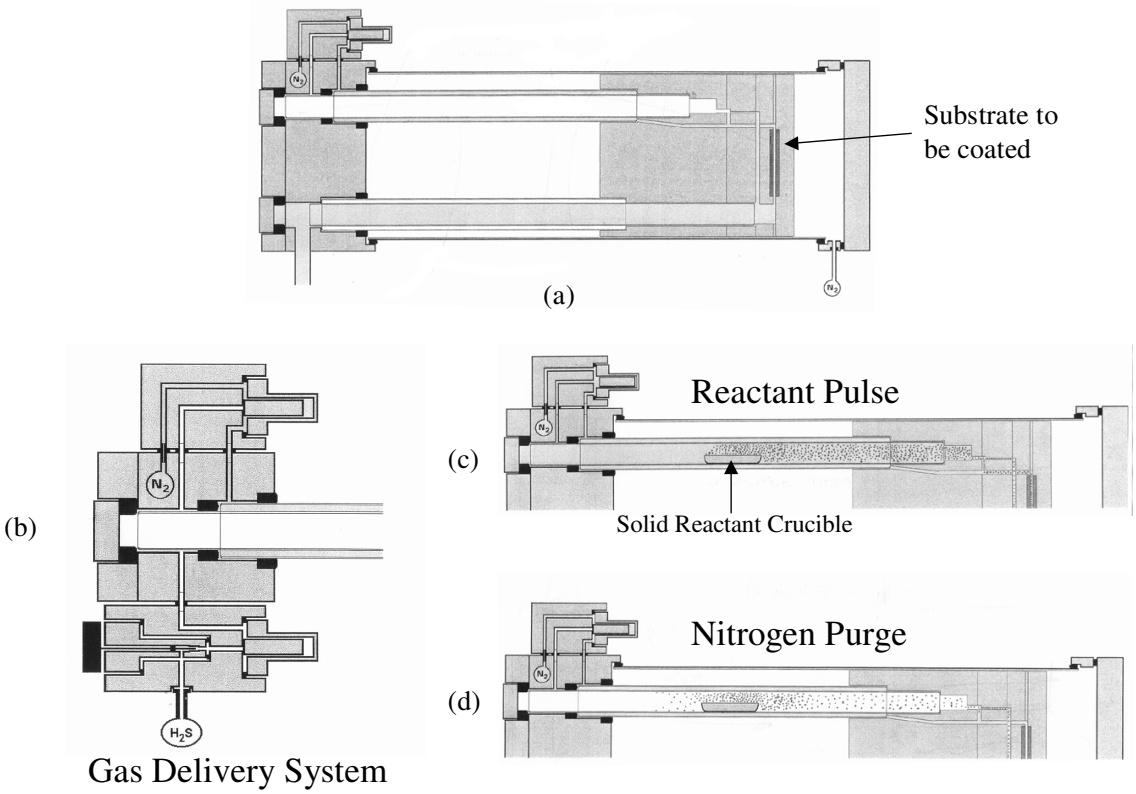

Figure 4.19 F120 ALD deposition tool schematic of reactor and precursor delivery sections. (a) detail of whole rector. (b) gas delivery system, (c) detail of reactor during a solid source pulse, and (d) detail of reactor during nitrogen purge [85]

4.6.2 Custom Built TiO_2 ALD Reactor

For ALD infiltration studies on location, a custom reactor was designed and built specifically for deposition of TiO_2 using $TiCl_4$ and H_2O liquid precursors. Figure 4.20 is a photograph of the system. Figure 4.21 shows a schematic of the reactor, which consists of a rotary vane pump, a Thermolyne tube furnace with a single zone that houses the sample deposition area, a liquid precursor delivery system, and a nitrogen purge. The reactor is capable of deposition of TiO_2 from 80° C to 600° C, and can be used to heat treat samples after deposition. The tube furnace is specified to have a 6" wide region with a ±0.3° C temperature profile, and a 12" region with ±3° C temperature profile. The substrates were placed on a 4" quartz boat and were positioned 5" from the center of the furnace, toward the exhaust side. The temperature deviation in this 4" region was measured to be ±0.15° C at 100° C.

TiO_2 was typically grown within the opal using alternating 4 sec pulses of $TiCl_4$ and H_2O, each separated by a 10 s, 225 sccm N_2 purge, while maintaining the substrate at 100˚ C. The vacuum level within the reactor was ~ 500 mTorr during pulses, and 200 mTorr during purges. The precursor gases, derived from room temperature liquid sources, were introduced to a N_2 carrier gas using computer controlled solenoid valves. Post-deposition heat treatment was performed in the ALD reactor with constant N_2 flow of 225 sccm.

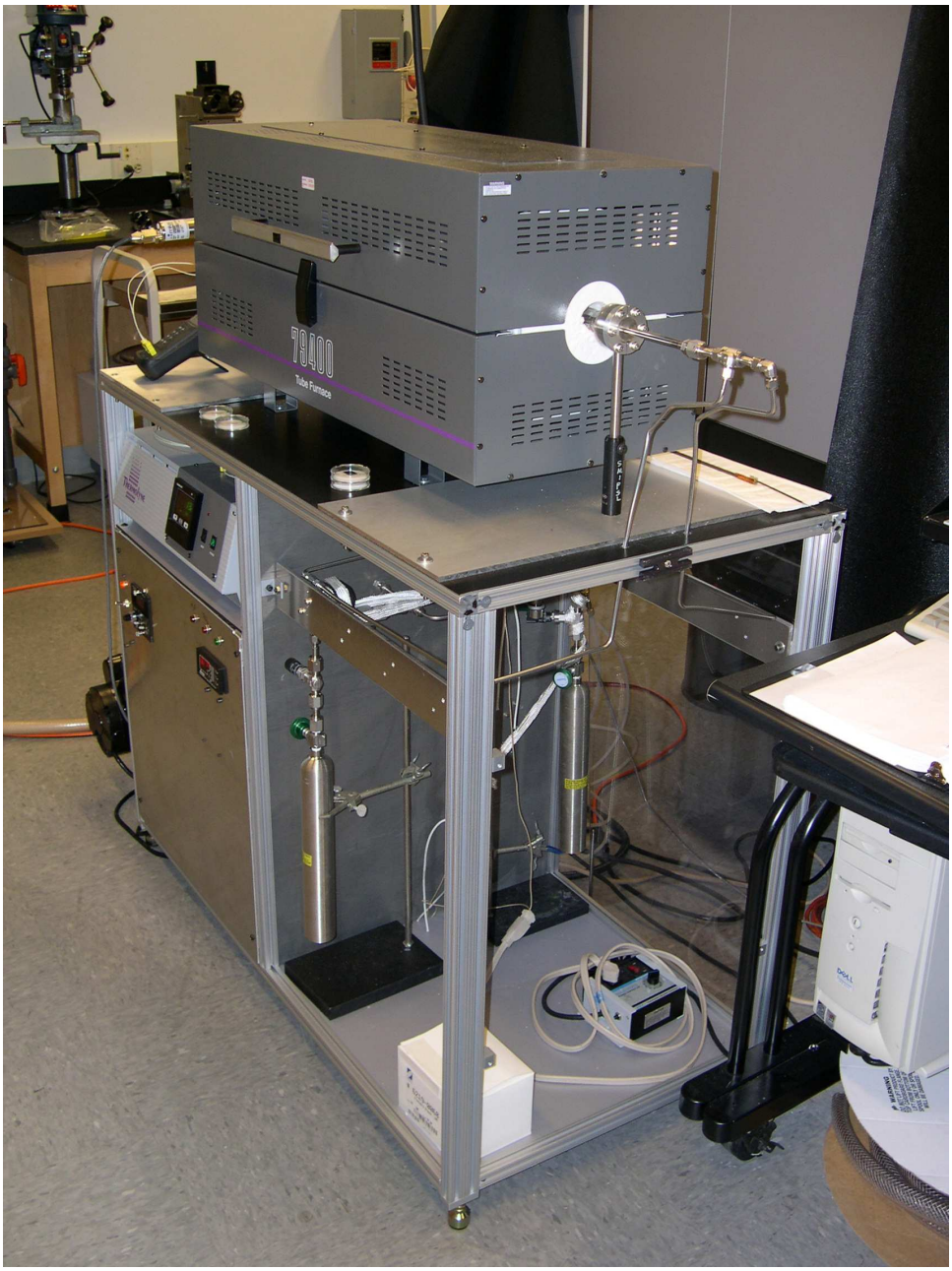

Figure 4.20 Custom built, flow-style, hot wall ALD Reactor.

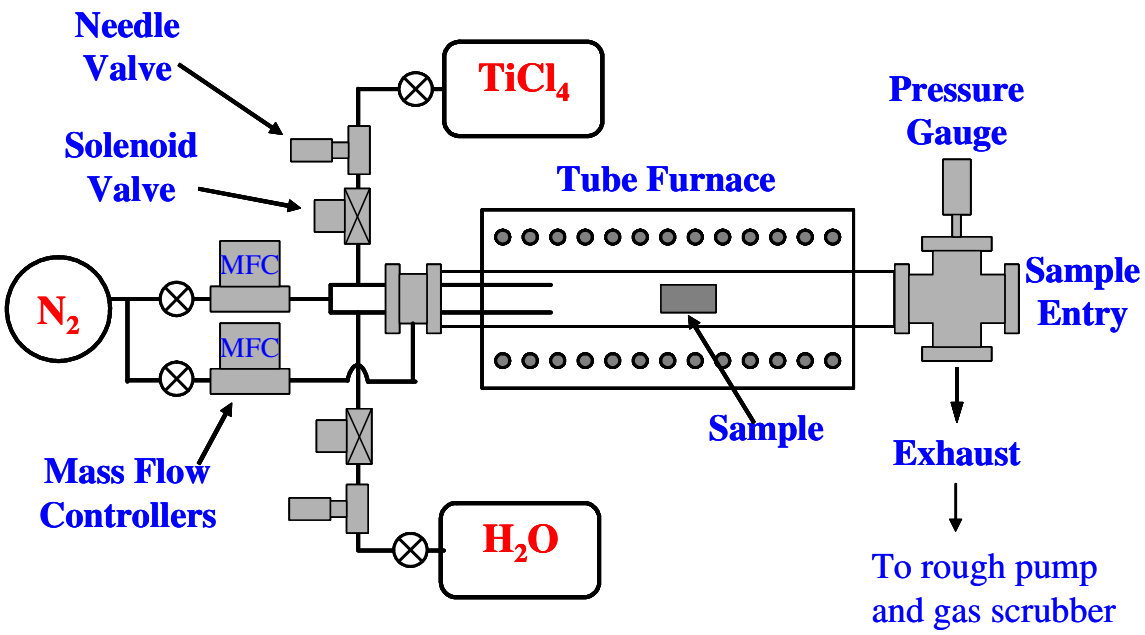

Figure 4.21 Schematic of custom built ALD reactor.

CHAPTER 5

FABRICATION OF ZNS:MN INFILTRATED AND INVERSE OPALS

The infiltration of three-dimensional opal structures with luminescent material was investigated by atomic layer deposition. While the index of refraction of ZnS:Mn is too low (2.3- 2.5) to achieve a full photonic band gap, it is high enough to exhibit PPBGs, and growth of it by ALD is a well understood process. The resulting PPBGs alter the optical density of states enough to influence the reflectivity and the emission characteristics of the infiltrated opal. Demonstrations using ZnS:Mn show that the maximum filling fraction for shell growth infiltration is possible using this technique, yielding filling fractions of 86%, as calculated from the shifts of the Γ-L photonic band gap that resulted after formation of the infiltrated opal. The infiltrated material was demonstrated to be of high-quality crystalline material as assessed by PL measurements. Angular dependent PL measurements also reveal significant modification of the shape of the emission curve by the effects of the photonic crystal. Intentional partial infiltrations were also performed, to demonstrate the level of control over filling fraction as well as band gap fine-tuning that ALD offers, and its potential for use in fabrication of multi-layer infiltrations.

5.1 High Filling Fraction Study

Two phases of ALD runs were performed using a Microchemistry F-120 ALE reactor, the first consisted of infiltrations of 300 and 460 nm opals, and the second consisted of infiltrations of a range of opals sized from 160 – 300 nm. These studies were designed to show that ALD allows formation of ZnS:Mn inverse opals of a variety of sizes with filling fractions that correspond to the maximum possible infiltration for shell-growth in a silica opal template, and that the PL emission behavior of these luminescent PCs was modified by the photonic band gaps that were formed.

5.1.1 ZnS:Mn Infiltration by Atomic Layer Deposition

In these studies, ZnS was grown by Atomic Layer Deposition (ALD) using $ZnCl_2$ and H_2S reactants at 500º C in a flow style reactor, as described in Chapter 4. [30, 58] The substrate was first exposed to a $ZnCl_2$ gas pulse, which resulted in the chemisorption of a monolayer of molecules on the surface.[63] The growth surface was next purged with N_2 to remove any excess $ZnCl_2$ and conversion to ZnS was then accomplished by application of a H_2S pulse to the substrate. An additional N_2 pulse to remove excess H_2S and the HCl byproduct completed the cycle. This sequence resulted in a partial monolayer of ZnS (0.78 Å per cycle), which was repeated to precisely grow a film layer-by-layer.[85] For these high filling fraction infiltration studies, the H_2S and $ZnCl_2$ pulse lengths were always kept equal, ranging from 220 ms to 880 ms, with 550 ms purge

lengths. The number of cycles applied to the opals was always more than predicted to be necessary for full infiltration, which led to a layer on the surface of the opal that was often thicker than the infiltrated layer, hereafter referred to as the "capping" layer. To fabricate optically active photonic crystals, Mn^{2+} was added as a luminescent center by combining $MnCl_2$ and $ZnCl_2$ in one long pulse every 100^{th} pulse cycle, as discussed in chapter 3.4.1.

In phase one, ALD runs were performed on opals deposited on quartz substrates. The sphere sizes were larger than the target values for photoluminescence modification using the Γ-L PPBG (as predicted from the photonic band diagrams for ZnS inverse opal), but were used as a demonstration of the capability of infiltration by this method. In the first set of runs, 500 nm of ZnS:Mn was deposited on 460 nm opals and 100 nm of ZnS was deposited on 300 nm opals. Standard thin film growth conditions as given by the F120 manual were initially used, consisting of 220 ms pulses and 550 ms purges at 500ºC. Precursor pulse times were then varied from 220 to 880 ms to optimize opal filling. Examination of cross-sections of infiltrated opals in an SEM revealed that pulse times of 660 ms and purge times of 550 ms produced the best results. In phase two, the deposition conditions were held constant at the values established in phase one, but the opal sphere sizes were reduced to the 160 – 300 nm range, and the coating thicknesses were reduced to 47 nm for opals below 300 nm, and to 70 nm for larger opals. Also, opals grown on silicon substrates were used to allow for better HF etching characteristics.

When viewed with the naked eye, the resulting films exhibit uniform angular dependent colors, indicating that the infiltration was homogeneous across the opaline film. Inverted structures were obtained by immersing the infiltrated opals in dilute (2-

5%) HF solution for 2 hours. Since the films were lightly sintered, the sphere contact points formed flow channels throughout the structure, which allowed the HF to penetrate the lattice, etching all of the spheres. Also, the HF was able to penetrate the ZnS layer, reaching the silica spheres without having to remove any of the capping layer. After rinsing and drying, successful inversion was evident by the noticeable color change of the reflected light from the surface of the opal. The resulting infiltrated and inverse films were characterized using XRD, SEM, FIB, specular reflectance, and photoluminescence.

5.1.2 Structural Characterization: Scanning Electron Microscopy and XRD

The SEM studies for the 460 nm opal are shown in Figures 5.1 and 5.2. Figure 5.1 shows a cross section of a cleaved opal, and Figure 5.2 the image of a trench that was cut in the opal surface using FIB. The images of the infiltrated opal show that the ZnS:Mn penetrates into the opal to a depth of several microns. The micrographs also illustrate that the coating is conformal, with low porosity, but polycrystalline, suggesting that discrete islands of ZnS grow on the surfaces of the spheres, instead of forming a continuous film. This was expected, since the silica spheres are not ideal for single crystal growth; they are amorphous. This growth mechanism was also observed during high temperature ALD infiltration of TiO_2 and will be discussed in chapter 6. In addition, the micrograph shows small uncoated regions centered in the spherical holes that are a result of the connectivity between the spheres after sintering. The amount of ZnS:Mn deposited was predicted to be 500 nm, and the measurement bar in Figure 5.1 shows a thickness of 400 nm for the capping layer. The coating thickness inside the opal was found to be on the order of the

maximum shell filling thickness for the sphere size, 35 nm, as indicated in the SEM image.

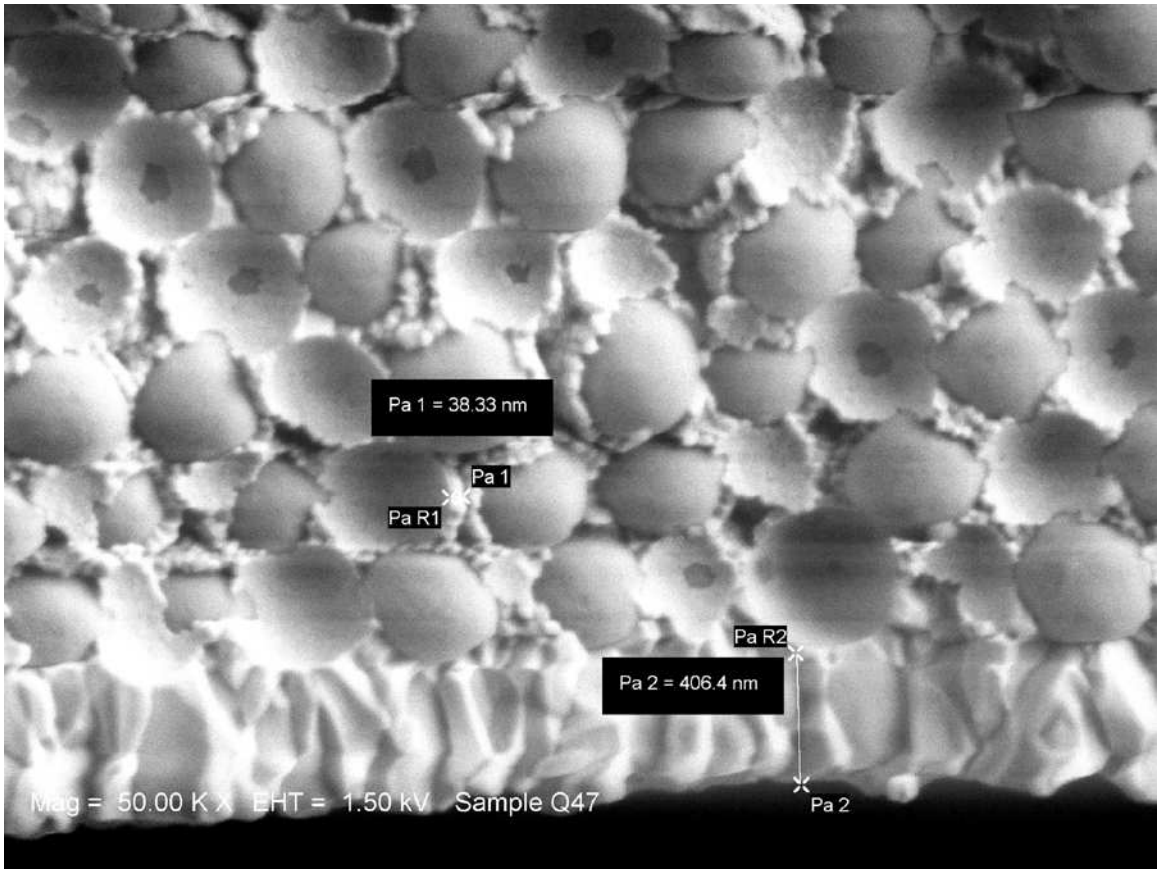

Figure 5.1 ALD run 1 – 460 nm ZnS:Mn infiltrated opal.

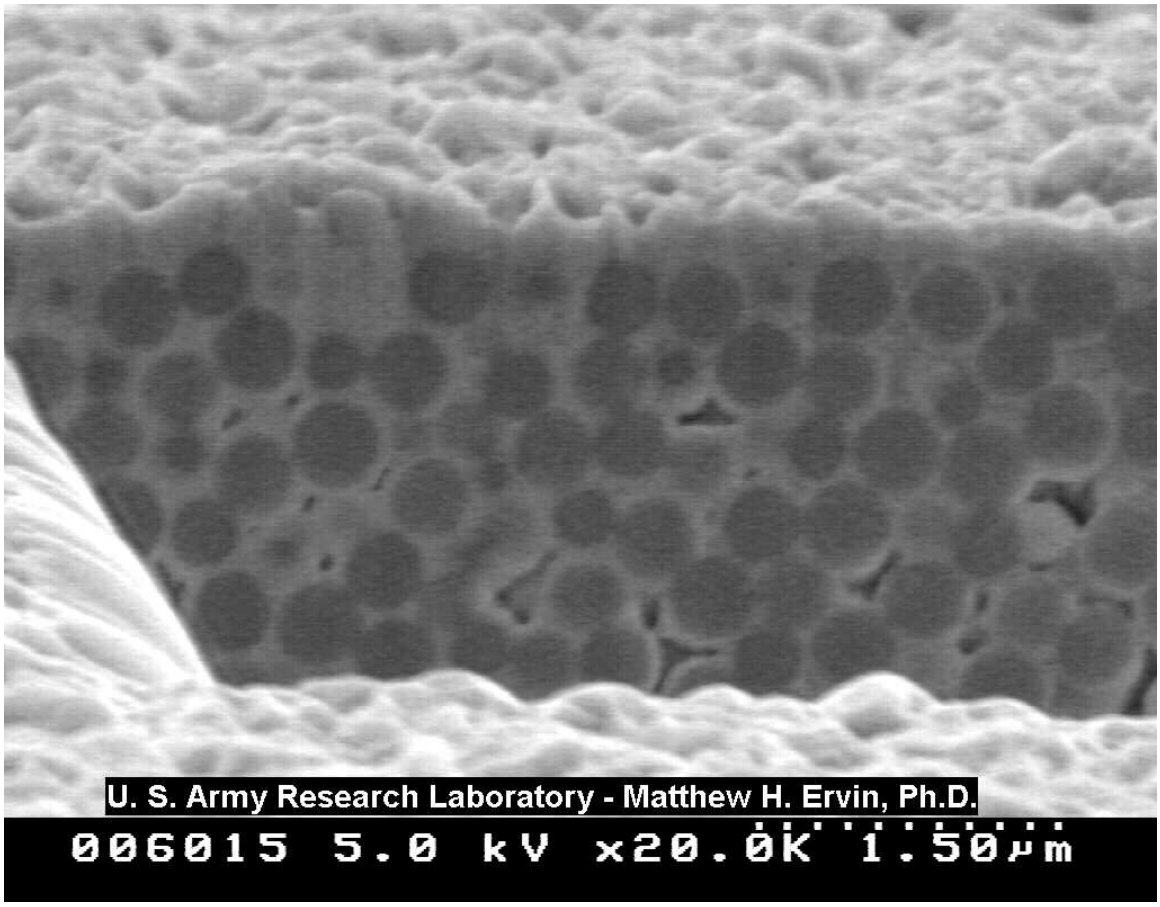

Figure 5.2 ALD run 1 – FIB trench cut in infiltrated 460 nm opal.

Figures 5.3 – 5.6 show the results of SEM studies on smaller sized infiltrated and inverse opals. Figure 5.3 is a cross section of a cleaved 240 nm opal that has been tilted to show the ordering of the top layer of the opal. Figure 5.4 is an SEM image of the cross-section of a fractured piece of a 300 nm infiltrated opal. This image shows that ZnS:Mn has fully infiltrated the structure. Figure 5.5 is a cross section of a cleaved inverse opal, after the 220 nm diameter silica spheres were etched with HF. In the image, the dark regions are the air holes that result from removal of the spheres, and the light region is the remaining ZnS:Mn honeycomb-like structure. While infiltration of 300 nm or larger opals resulted in full penetration, it was later discovered that for inverse opals fabricated from spheres in the 200 nm size range, hollow structures were formed, with several micron thick layers on the top and bottom. Figure 5.6 is a lower magnification SEM image of a fractured 220 nm inverse opal. This image clearly shows formation of a hollow inverse opal "chip". However, 20 sphere layers is a suitable thickness for a photonic crystal, so while it would be optimal if complete filling had been observed, the depth of penetration achieved was sufficient to form a high quality photonic crystal. The reason for this incomplete filling is that the pulse times were too short for full saturation of the opal interior surface, and these experiments did not attempt long enough pulses to get full infiltration of opals in the 200 nm size range. This occurrence was also found in ALD TiO_2 infiltration studies, and was solved by increasing the pulse and purge times to significantly longer lengths (~ 10 s) until full penetration was achieved as discussed in Chapter 6.

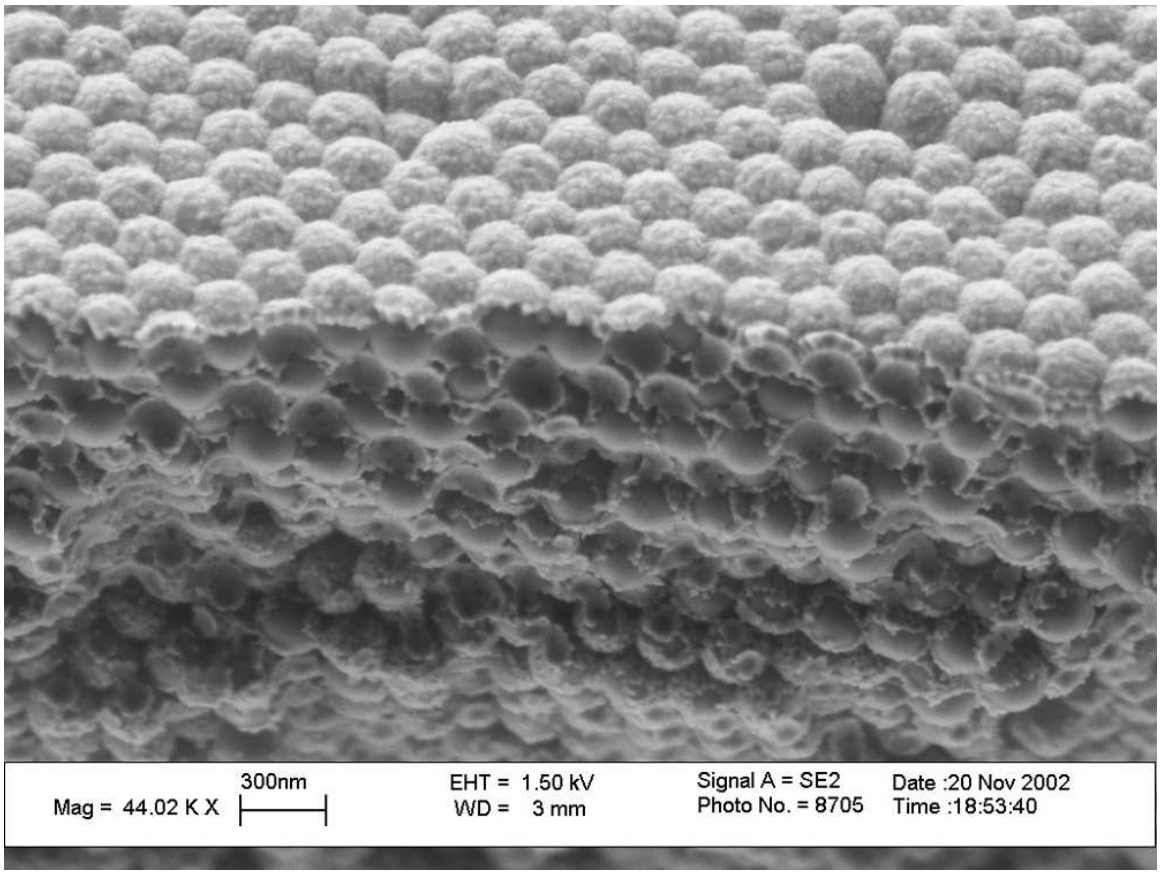

Figure 5.3 Tilted cross section of cleaved 240 nm opal

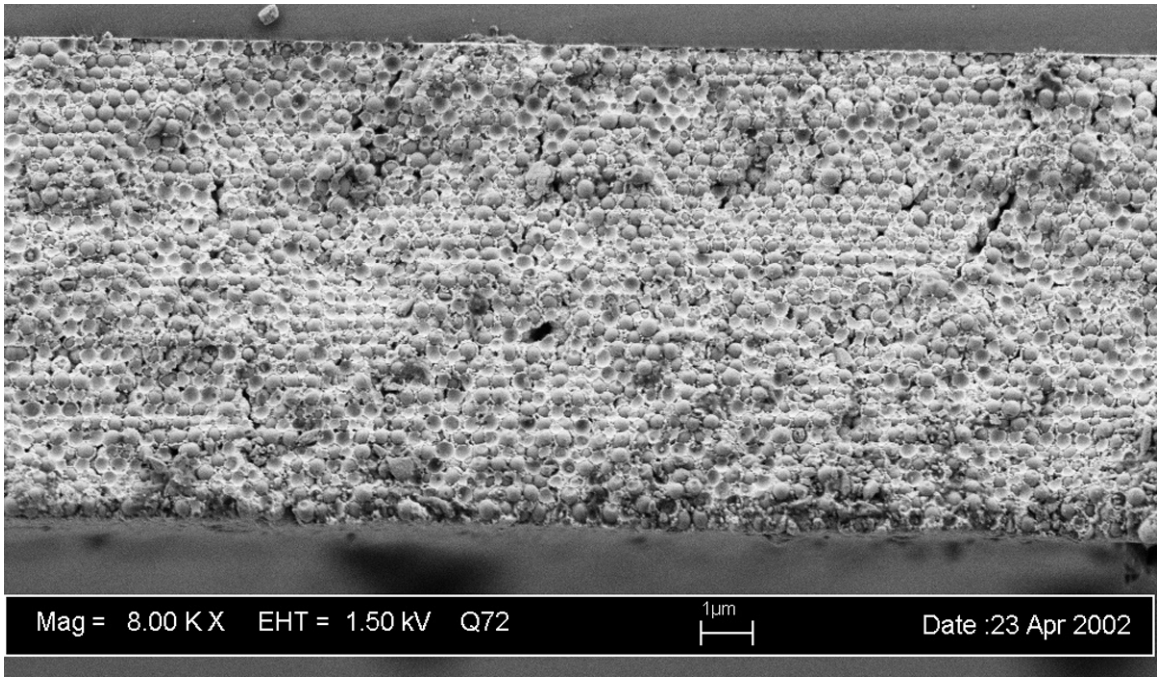

Figure 5.4 300 nm ZnS:Mn-infiltrated opal.

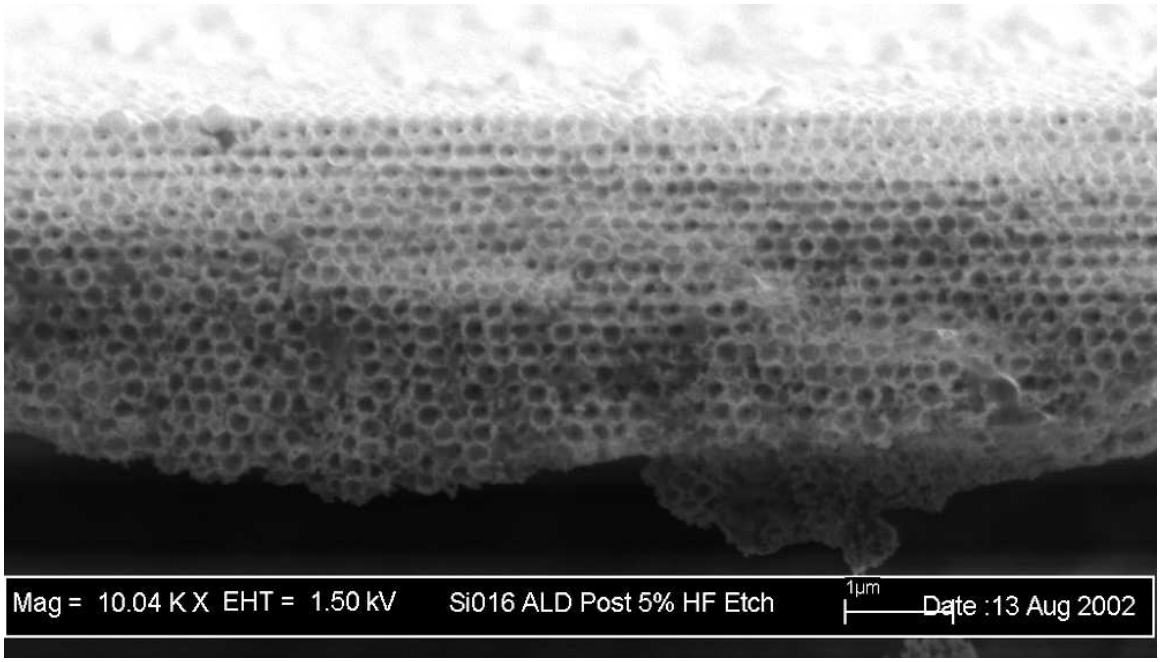

Figure 5.5 220 nm HF-etched ZnS:Mn inverse opal.

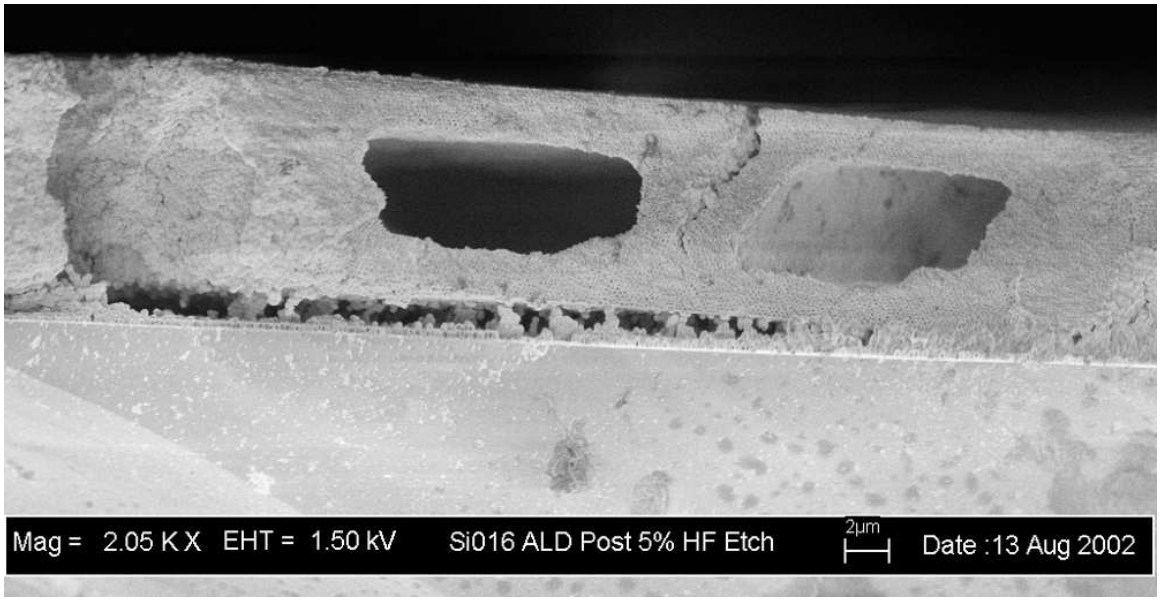

Figure 5.6 220 nm HF-etched ZnS:Mn inverse opal cross-section, lower magnification.

To confirm the formation of crystalline ZnS:Mn, XRD was performed. Figure 5.7 shows typical x-ray data for a 330 nm infiltrated opal. The data indicates that the hexagonal wurtzite phase has formed. The indexed peaks all correspond to this phase.

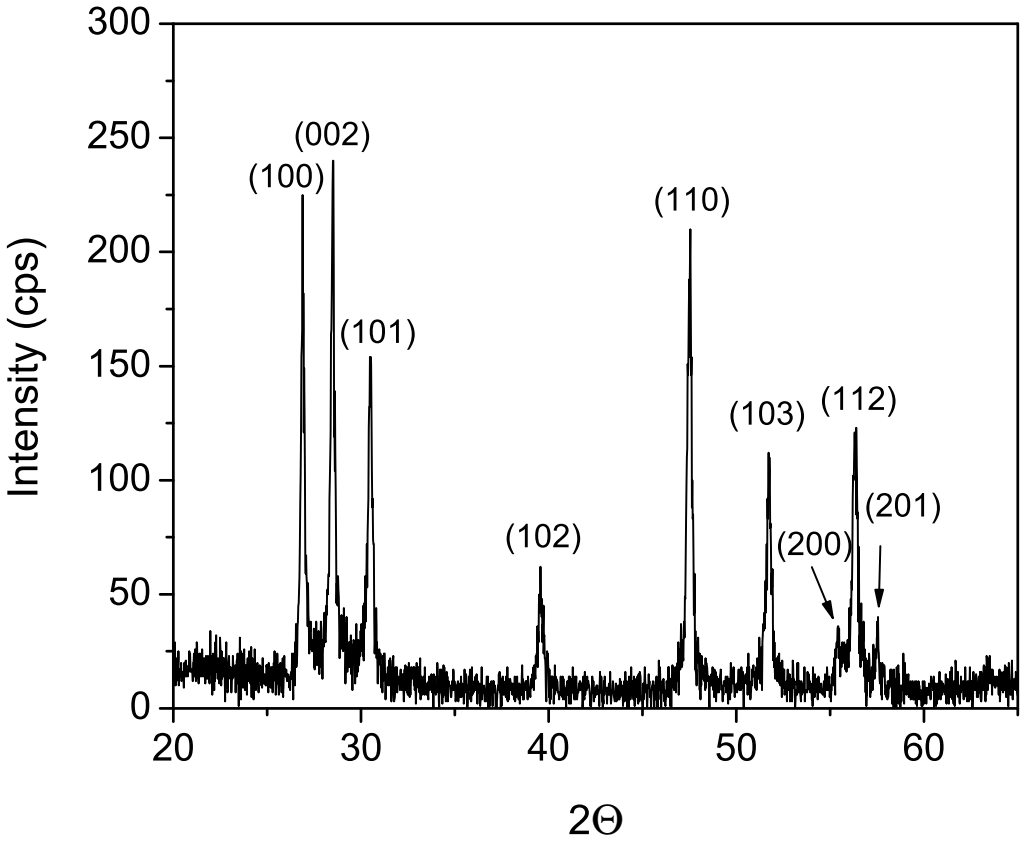

Figure 5.7 X-ray diffraction data for a 330 nm ZnS:Mn infiltrated SiO_2 opal.

5.1.3 Photonic Band Gap Characterization: Specular Reflectance

The (111) Bragg peak position was determined from specular reflectance measurements taken before and after infiltration, and after etching. This peak corresponds to the first stop band at the L-point in the photonic band structure, between the 2nd and 3rd bands. The filling fraction was calculated using equation 4.5, by using the bulk value for the refractive index of silica and measured values from ZnS:Mn thin films deposited under the same conditions, but on planar substrates. The resulting ZnS:Mn index was slightly lower than bulk ZnS values, for example 2.40 and 2.42 for ALD and bulk films, respectively, at 500 nm.[69] Figure 5.8 shows the measured 15° incidence specular reflectance for a 300 nm opal as-deposited (unsintered), after infiltration, and after etching (inverse opal). This data is also shown in Figures 5.9 – 5.11, which compare the reflectivity curves with their respective calculated band diagrams. The reflectivity for the sintered opal shows a strong narrow peak at ~650nm, consistent with the gap shown in the photonic band diagram for a 300 nm opal. After infiltration, the primary peak shifts to ~850 nm and widens, consistent with the shift shown by the calculated diagram, but at a slightly longer wavelength. In addition, higher energy peaks were observed that coincide with the upper level "flat" bands where a PPBG is starting to form. For the inverse opal, the primary peak position decreases to ~725 nm, becomes more sharply defined, but again the peak is at a wavelength slightly longer than the midgap predicted by the photonic band diagram. Again, higher energy peaks are present; this time coincident with a definite PPBG. As anticipated, since the Bragg peak positions were at longer

wavelengths than the photonic band diagrams predicted, the infiltrated and inverse opals had unrealistic filling fractions of slightly over 100%.

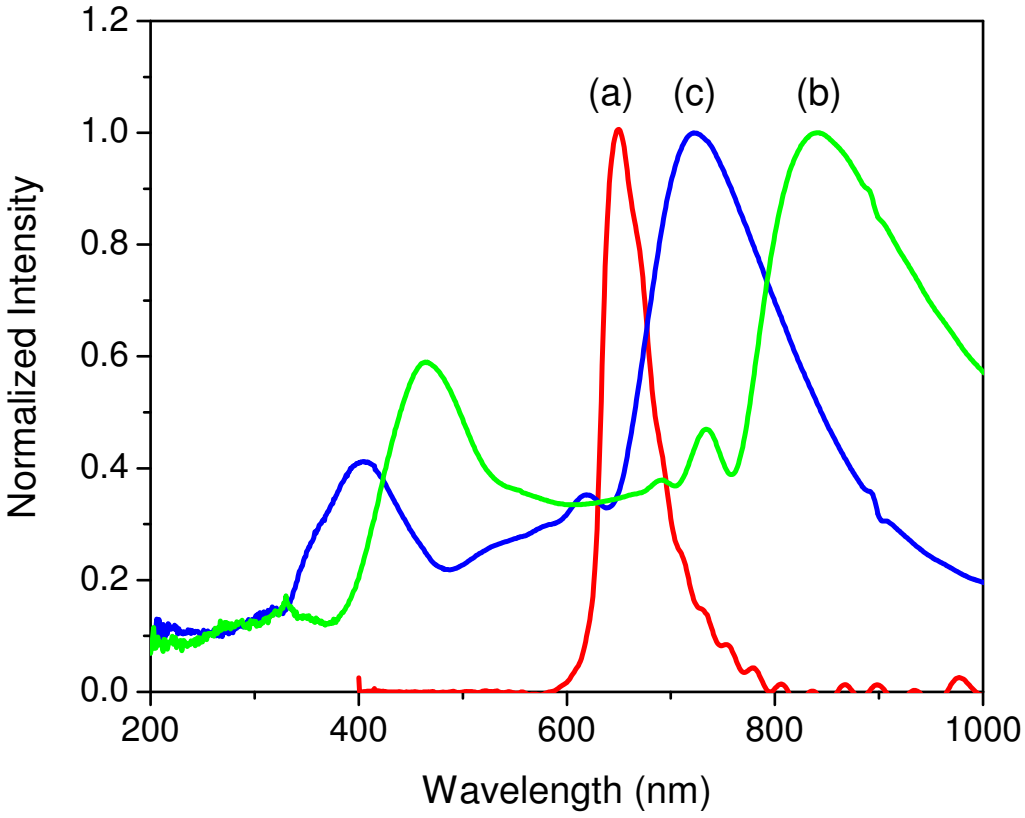

Figure 5.8 Specular reflectivity for 300 nm (a) as deposited opal, (b) infiltrated opal, and (c) inverse opal.[58]

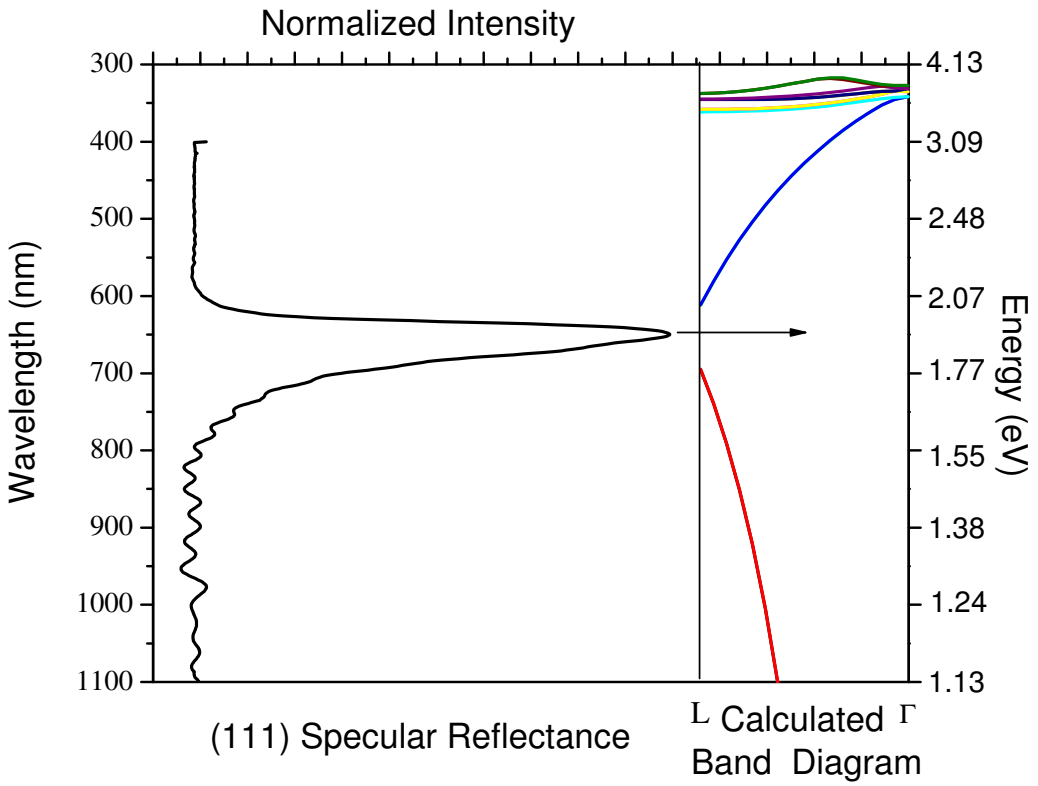

Figure 5.9 Specular reflectivity and calculated photonic band diagram for 300 nm bare opal.

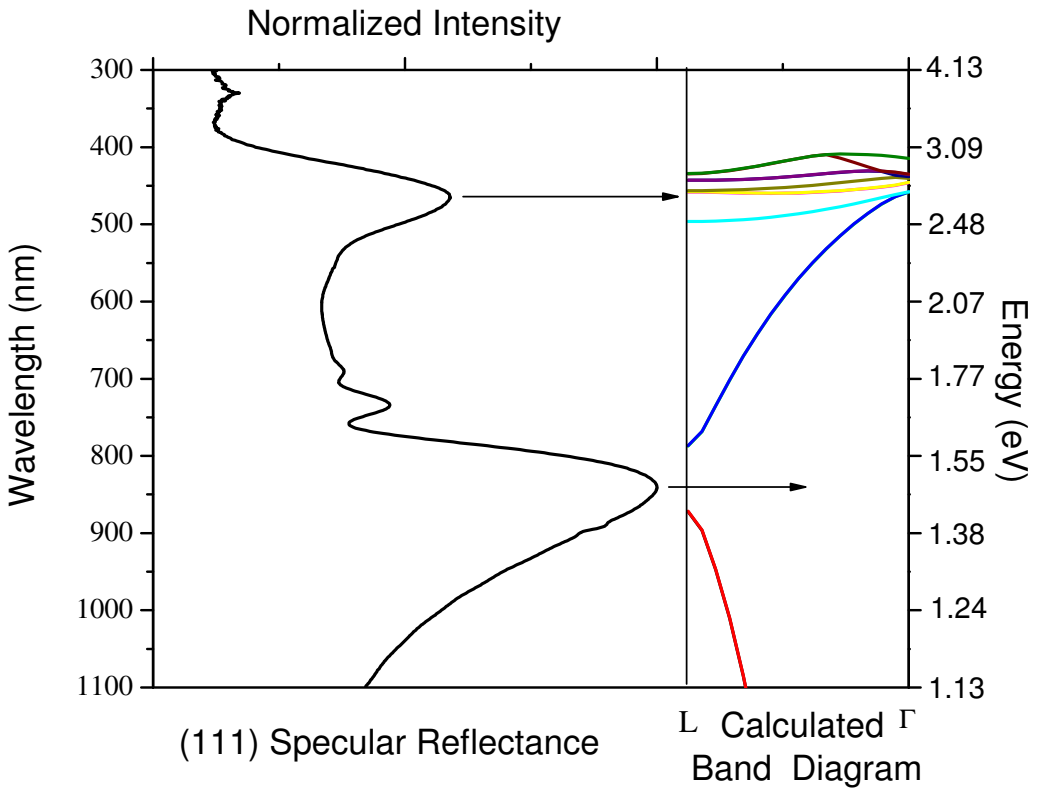

Figure 5.10 Specular reflectivity and calculated photonic band diagram for 300 nm ZnS:Mn infiltrated opal.

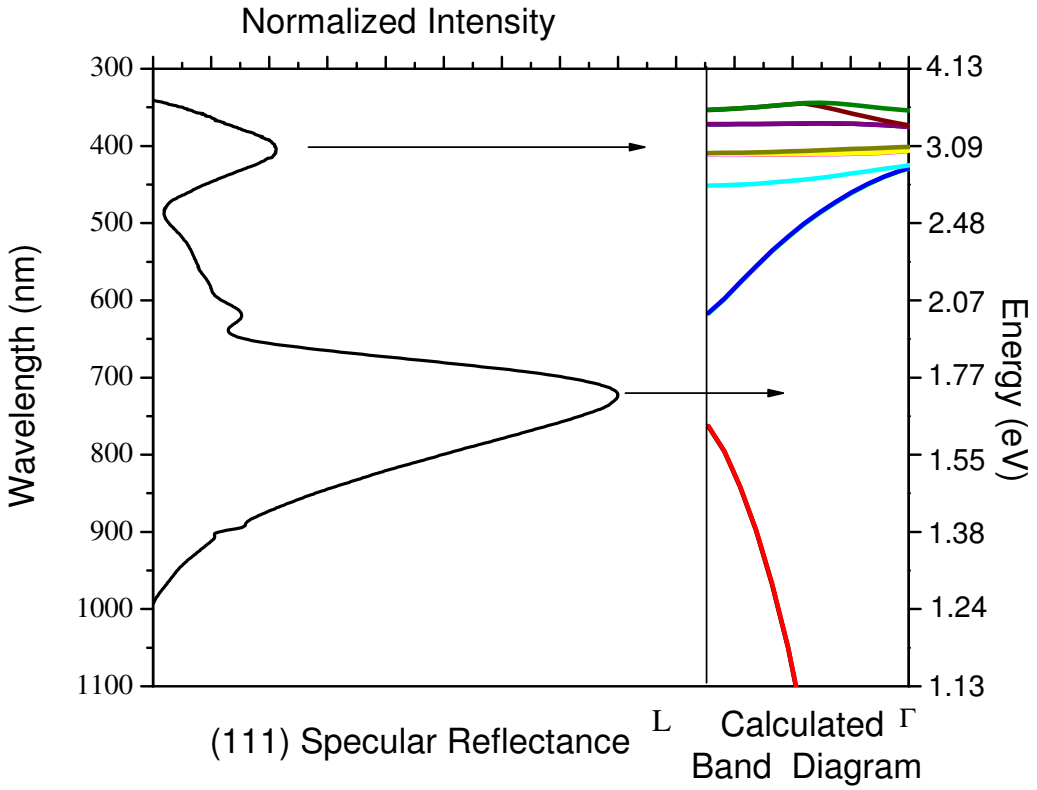

Figure 5.11 Specular reflectivity for 300 nm ZnS:Mn inverse opal compared with calculated photonic band diagram.

As shown in Figure 5.12, when the positions of the Bragg peaks from all measured opals as a function of sphere size are compared, the trend line indicates an average fill fraction of 90%, which is slightly above the maximum predicted shell-growth filling fraction of 86% As the sphere sizes decrease, there is an increased deviation from the trend line, resulting in unrealistic filling fractions (>100%). This is attributed to peak broadening and shifting effects that result from the capping layer on top of the opal that occurs if the amount of material deposited using ALD exceeds the maximum filling fraction of the underlying opal. Thin film interference effects from the surface layer then begin to affect the reflectivity measurements. Initially the ALD infiltration amounts were not scaled for each sphere size, and the effect was found to increase as the sphere sizes decreased. For example the 160 nm opals were coated with the same amount of ZnS:Mn as the 240 nm opals, so they would have reached full infiltration earlier in the run than the larger opals, and there is a trend toward greater apparent filling fractions (false results) as the sizes decrease.

Removing all or a portion of the capping layer using an ion mill revealed the correct position of the Bragg peak, as illustrated in Figure 5.13. The sample studied was a 200 nm opal that was infiltrated with 50 nm of ZnS:Mn. The maximum infiltration layer thickness should have been 15.5 nm, far less than was deposited. The reflectivity data for the as-infiltrated opal shows a broad peak at 589 nm. The peak has flattened out, and shifted to a position that would indicate a filling fraction of > 90%. However, milling the sample for 10 minutes caused the reflectivity data to change significantly. The resulting data shows the expected characteristics of a correctly infiltrated opal. It now has a well-defined Γ-L peak at 535 nm, corresponding to a filling fraction of 83% of the available

pore volume, as well as a flat band peak at 345 nm, and the spectra has the same features as the data collected from partial infiltrations (presented in section 5.2), where the capping layer effect is minimized. From this understanding of the effects of over-deposition, it was found that by properly controlling the deposition, ZnS infiltrated opals were formed whose reflectivity data agrees better with the calculated photonic band diagrams as well as the Bragg equation.

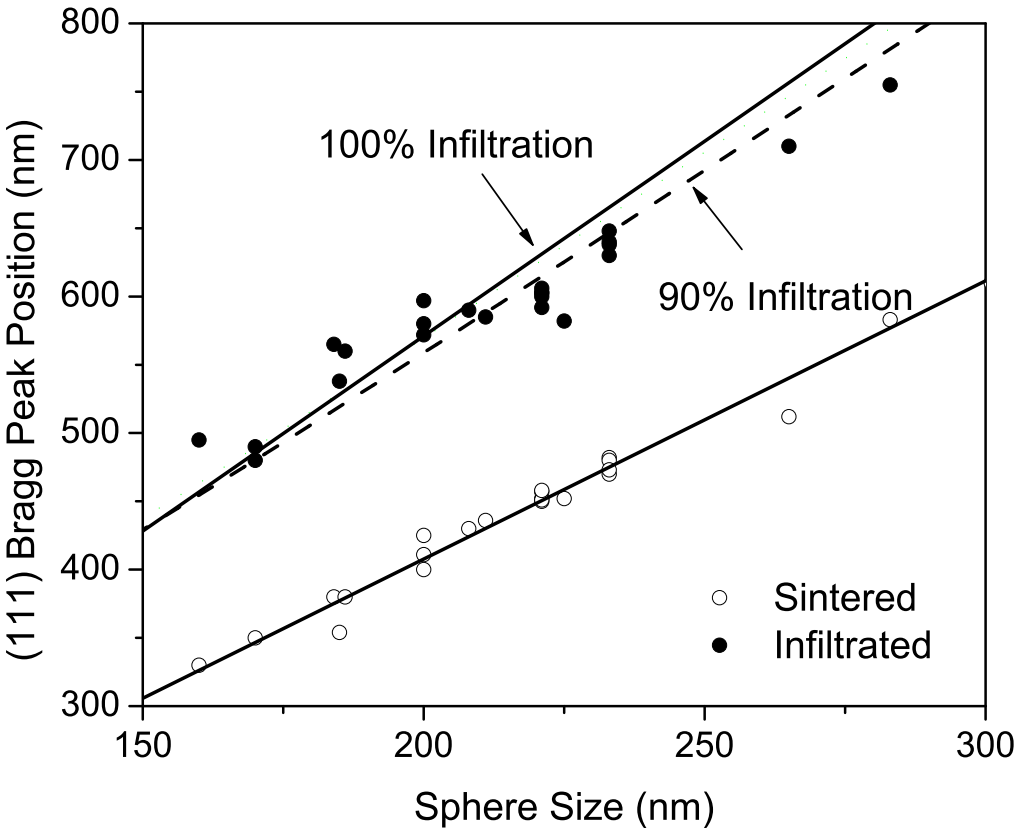

Figure 5.12 Bragg peak position shifts and infiltration % trend lines as a function of sphere size for ZnS:Mn infiltrated opals.[58]

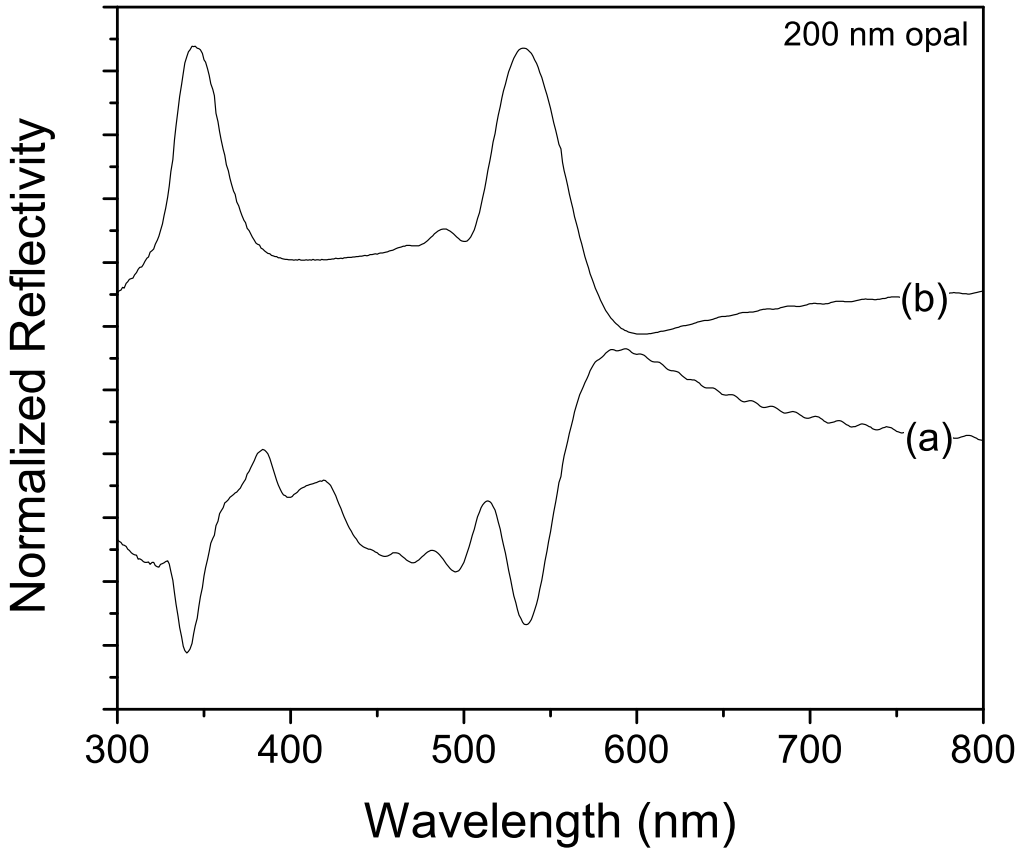

Figure 5.13 Specular reflectivity from 200nm opal after (a) infiltrating with 50 nm layer of ZnS:Mn and (b) after ion milling for 10 min.

5.1.4 Photoluminescence Measurements: Modification of Spontaneous Emission

The photoluminescence of ZnS:Mn infiltrated and inverse opals was measured using both ZnS band edge excitation at 330 nm, and direct Mn^{2+} activator excitation at 390 nm. These measurements were performed using the Jobin-Yvon Fluorolog system described in Chapter 4. Band edge excitation is a good indicator of crystal quality of the host lattice (ZnS). Direct excitation was also used for examination of luminescence modification by the photonic crystal, because it exhibits a broader emission peak, and the lower energy of the excitation photons allows for deeper penetration into the opal, since the ZnS absorption coefficient is much lower for this energy.

Figure 5.14 shows a typical PL spectrum of a ZnS:Mn infiltrated 225 nm opal excited by 330 nm radiation. The luminescence intensity was measured to be as strong or stronger than that observed from co-deposited ZnS:Mn thin films. The broadband PL peak at 585 nm is due to Mn^{2+} emission, and the blue peak at 460 nm is due to self-activated luminescence from Cl^- defects, resulting in donor-acceptor emission, arising as a result of the $ZnCl_2$ precursor.[86] The peak intensities are comparable to a standard ZnS:Mn thin film, indicating good crystallinity. Figure 5.15 shows a typical direct excitation PL spectrum from a 225 nm infiltrated opal. The luminescence peak is broad, ranging from ~500 – 750 nm, and reaches a maximum at 585 nm. The PL exhibited twice the number of counts per second for 585 nm emission under direct excitation compared to band edge excitation.

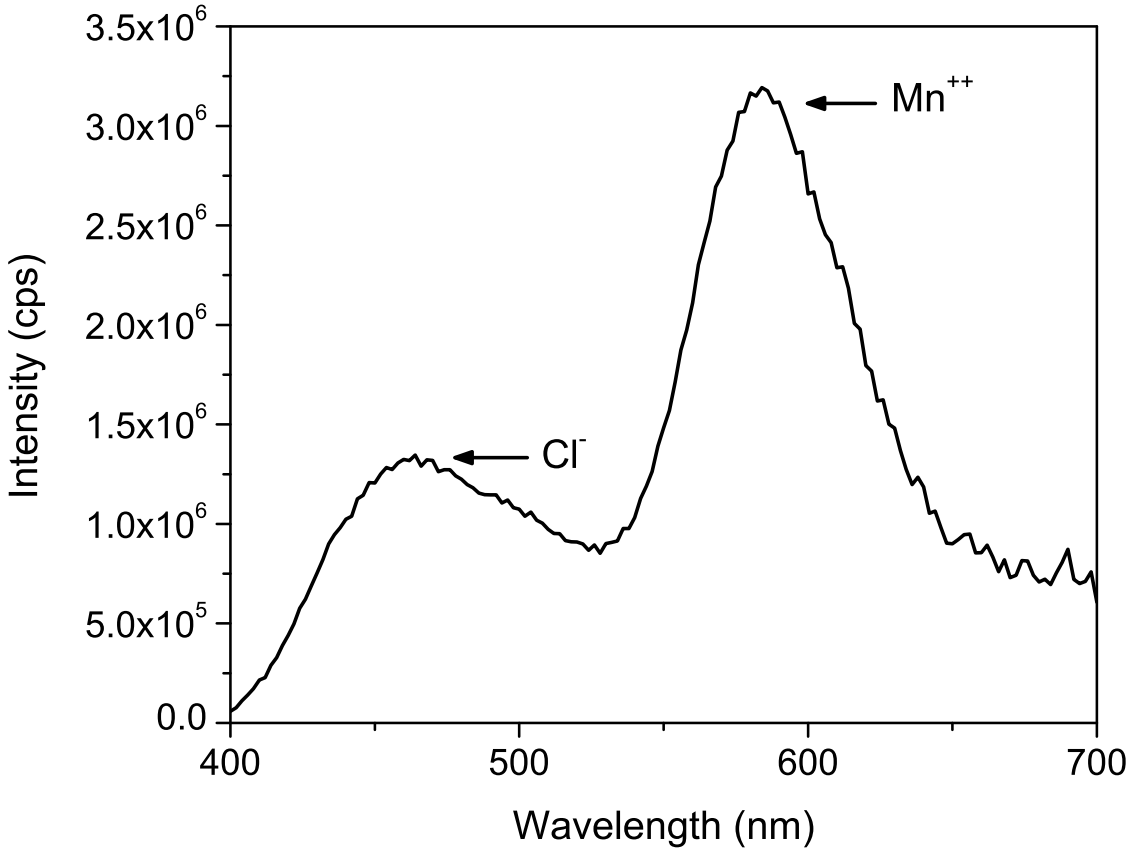

Figure 5.14 Photoluminescence measured from band edge excitation (330 nm) of a ZnS:Mn infiltrated 225 nm opal.

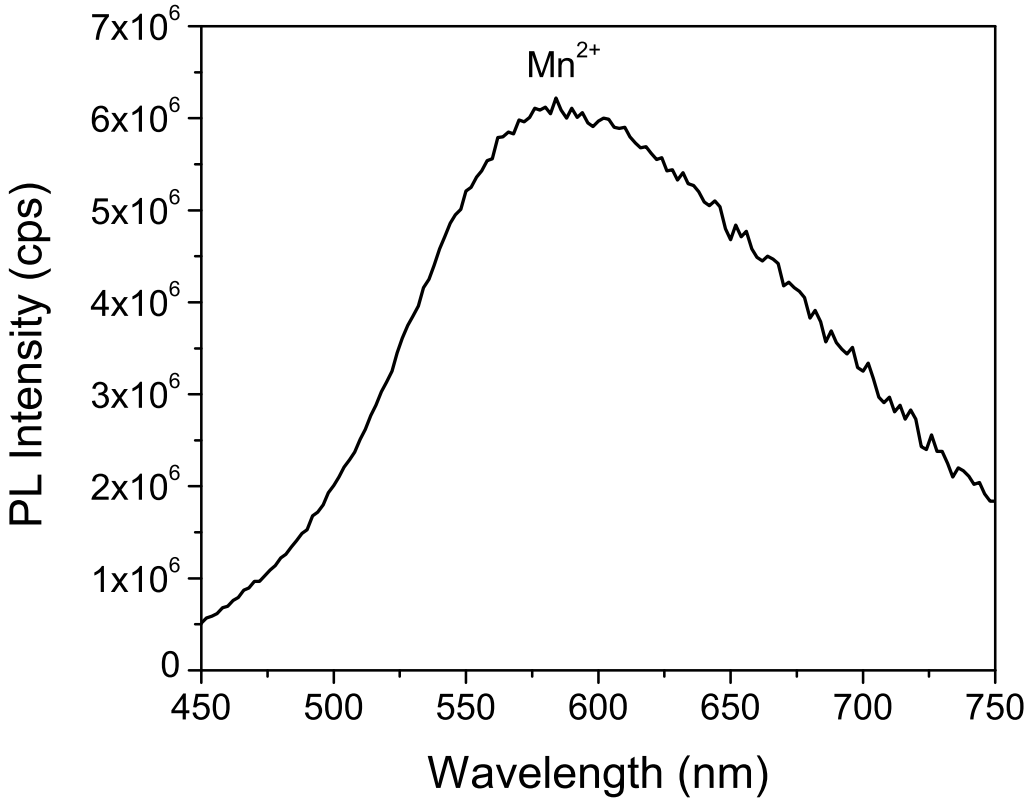

Figure 5.15 Photoluminescence measured from direct excitation (390 nm) of a ZnS:Mn infiltrated 225 nm opal.

Using the fiber collection system described in Chapter 4, angular dependent PL measurements were next performed, to characterize the modification expected in the photoluminescence due to the shift in photonic density of states by the photonic crystals. Figure 5.16 shows the angular dependent PL data for a 200 nm ZnS:Mn infiltrated opal, excited at 330 nm. Angular dependent specular reflectivity data was also measured, and is included for comparison. The spectral characteristics of the PL and the reflectivity clearly changed dramatically as the angle was increased. Examination shows that the PL modification is coupled with the change in density of states revealed by the reflectivity measurements. For example, as discussed below, the features in the PL, such as dips, flat regions or peaks, are coincident with similar features in the reflectivity.

The intensity of the 585 nm peak was reduced when θ was shifted to 30˚, which is consistent with the shifting of the PPBG on top of the peak as shown by the corresponding shift in the reflectivity. When the angle was increased to 40° and 50˚, the effect on the PL is consistent with the shift of the (111) pseudo-PBG to 540 nm, as the valley at this wavelength is noticeably deeper. Also at 30˚, the PL shows a dip that lines up with the 510 nm PPBG. The dip in the PL shifts to ~460 nm for θ = 50˚, and again was coincident with the PPBG found from the reflectivity measurements. For θ = 60°, the Cl^- defect peak was sharpened, bracketed by two regions of high reflectivity.

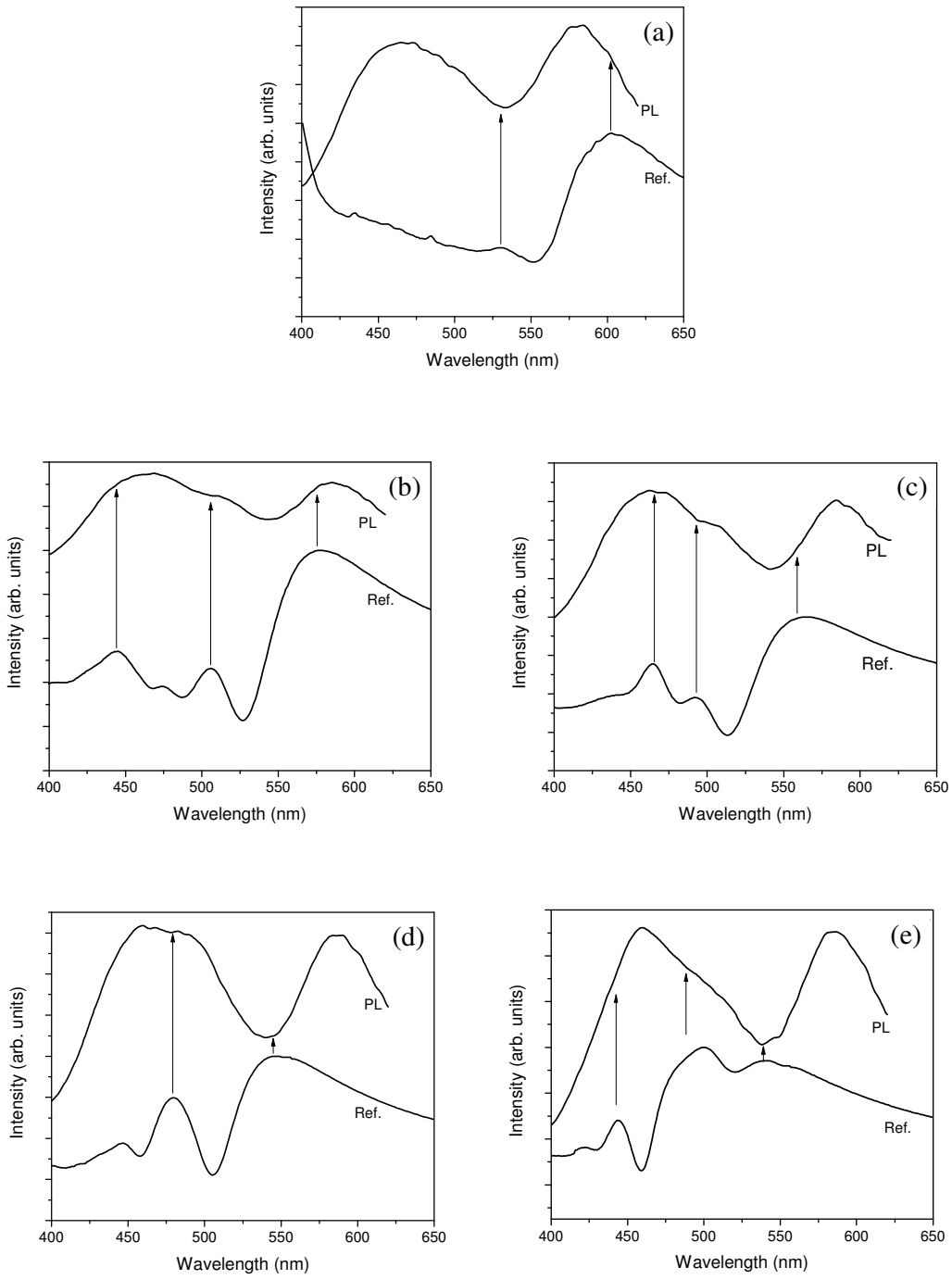

Figure 5.16 Angular dependent PL of ZnS:Mn infiltrated opal, compared with angular dependent reflectivity for collection at angles of (a) 0° (b) 30° (c) 40° (d) 50° and (e) 60° from normal incidence. (330 nm excitation)

Figure 5.17 illustrates the PL and reflectivity results for the same opal when excited at 393 nm. It was anticipated that the decreased absorption in the ZnS would allow for deeper penetration of the excitation, and should reveal more luminescence suppression by the photonic band gaps. Typically, the PL that results from a thin film of ZnS:Mn under direct excitation of the Mn^{2+} ion results in a broad peak at 585 nm, as previously shown in Figure 5.15. However, the Γ-L PPBG for the 200 nm opal is coincident with this emission peak, and the data confirms that the PC suppresses emission at 585 nm. Comparison of the degree of suppression indicates that suppression of spontaneous emission was more pronounced in the direct excitation than in the band edge excitation PL measurements. Again the changes in the shape of the PL correspond to the peaks and valleys in the reflectivity data.

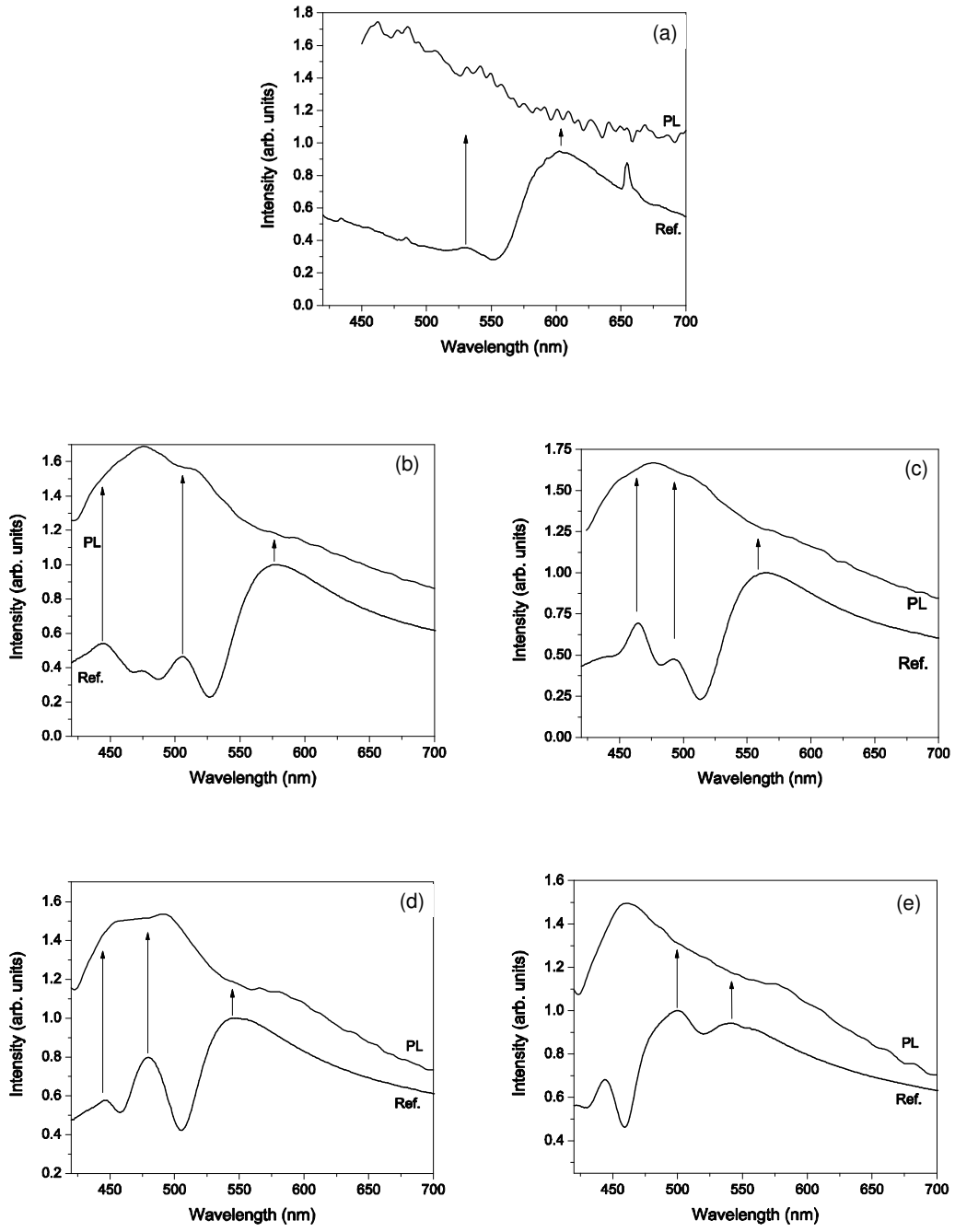

Figure 5.17 Angular dependent PL of ZnS:Mn infiltrated opal, compared with angular dependent reflectivity for collection at angles of (a) 0° (b) 30° (c) 40° (d) 50° and (e) 60° from normal incidence. (393 nm excitation)

Figures 5.18 and 5.19 show angular dependent PL for the same sample, after forming the inverse opal, when excited by 330 nm UV light. Reflectivity measurements indicated that the (111) PPBG occurs at a shorter wavelength, ~520 nm for normal incidence, so the 460 nm peak PL was expected to be affected instead of the 585 nm peak. Figure 5.18 shows the entire PL spectrum, for angles 0, 10 and 30 degrees, and Figure 5.19 shows only the 460 nm emission for the same angles. At $\theta = 0^{\circ}$, the reflectivity peak occurs between the 460 and 585 nm PL peaks, so no modification was observed. However, as the angle was increased to 10° the PPBG shifted closer to the 460 nm peak, and as a result, an 18% reduction in the normalized peak height was observed. The 30° measurement shows the shift of the PPBG position to ~485 yielded an additional reduction resulting in an overall 44% reduction in normalized peak intensity at 460 nm.

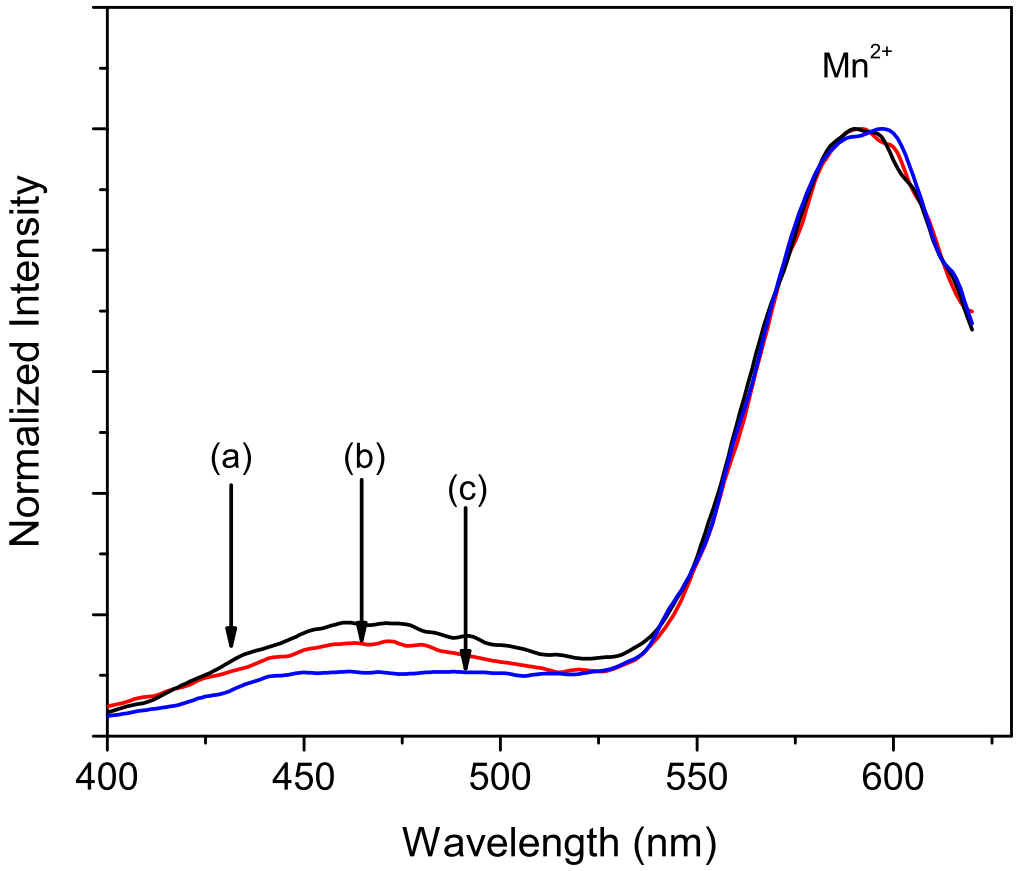

Figure 5.18 Angular dependent photoluminescence from 200 nm ZnS:Mn inverse opal, 330 nm excitation. Collection at angles of (a) 0° (b) 10° and (c) 30° from normal incidence. Data normalized to 585 nm emission peak.

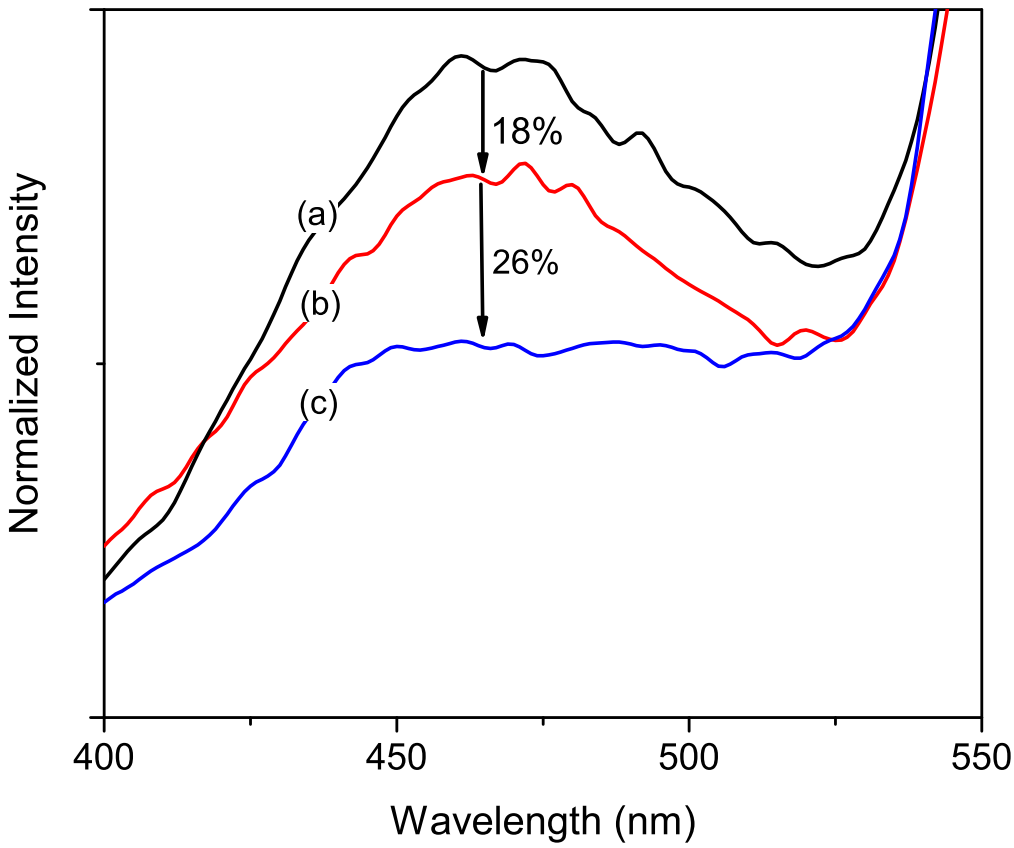

Figure 5.19 Angular dependent photoluminescence from 200 nm ZnS:Mn inverse opal, scaled for viewing 460 nm luminescence peak. Collection at angles of (a) 0° (b) 10° and (c) 30° from normal incidence, with positions of maximum reflectivity peak indicated.

Angular dependent PL was next measured on the same sample, for 393 nm excitation, and the resulting data is summarized in Figure 5.20. There is a pronounced dip in the PL for the normal incidence collection, the solid red curve in the figure. This dip corresponds to the (111) PPBG observed in the reflectivity measurements. As the angle was increased, the dip was pronounced, and the PL curve shifted to shorter wavelengths. At 10 and 20°, the effect of the PBG is still apparent, but by 40°, the PL curve has returned to the shape normally found for 393 nm direct excitation. The shift of the PPBG position is indicated by the vertical dotted lines in the figure.

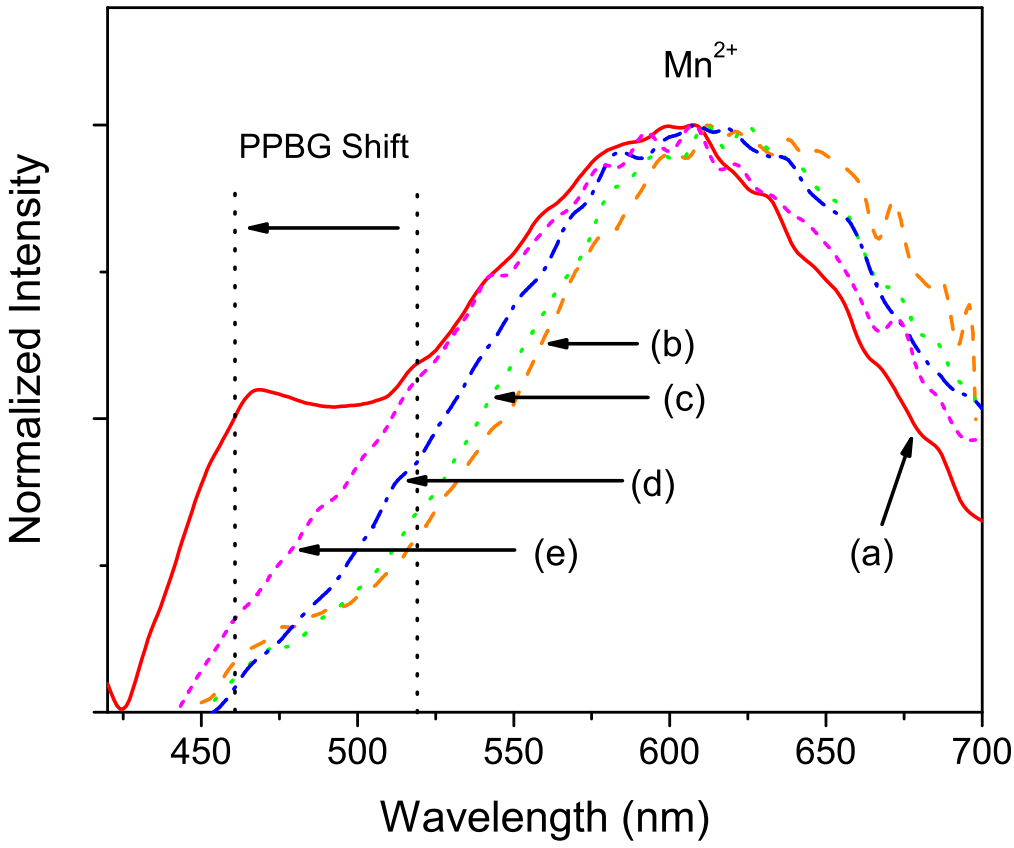

Figure 5.20 Angular dependent photoluminescence, 200 nm ZnS:Mn inverse opal, 393 nm excitation. (a) 0° (b) 30° (c) 40° (d) 50° and (e) 60° from normal incidence.

5.2 Photonic Band Gap Tuning: ZnS Infiltration Control

In addition to full infiltration, a study of partially infiltrated opals with ZnS:Mn was performed. The motivation of this study was to observe the evolution of the PBG as a function of infiltration amount, and to build the skill set required for formation of two and three layer composite luminescent photonic crystals. In order to make these structures, the infiltration must be highly conformal, leaving room for the second infiltration layer. Also, Mn^{2+} doping was more difficult since the standard doping sequence of a doping pulse every 100^{th} cycle had to be modified for depositing the fewer cycles required for 2.5 nm films. Thus, the doping pulse sequence was modified, and consisted of a 3 s pulse that included both $MnCl_2$ and $ZnCl_2$, applied every 32 cycles for films ≥ 5 nm, and of a single pulse of 1.5 sec. applied in the middle of the deposition for 2.5 nm thick layers (after 16 cycles). These experiments were also performed in the F120 ALD tool. Opals with sphere sizes of 330 nm, and 440 nm were used, and each size of opal was infiltrated with 2.5, 5, 10, and 20 nm thick layers of ZnS:Mn whose thickness was projected from the planar growth rate of 0.78 Å per cycle. The resulting particle sizes of the growing films were analyzed by measurement of the width of the (0 0 2) XRD peaks. The Scherrer equation yields particle size estimations of 9.2, 16.3, 19.2, and 24.8 nm for the four infiltrations, in order of increasing deposition thickness. These estimations are likely off by a factor of 2-3, but they confirm the resulting increase in particle size with increasing film thickness.

5.2.1 Photonic Band Gap Tuning: Specular Reflectance

The specular reflectance from deliberate partial infiltrations of a 330 nm silica opal with 2.5, 5, 10 and 20 nm thick ZnS:Mn layers are shown in Figure 5.21, for 15˚ from normal incidence. In the as-sintered condition, the peak at ~710 nm corresponds to the (111) Bragg diffraction peak, which arises due to a pseudo photonic band gap in the Γ-L direction. From calculations of the photonic band behavior of a stepwise ZnS-infiltrated opal, it was found that as the shell layer thickness increased, the PPBG is predicted to first shift to a longer wavelength, then disappear when the shell thickness reaches ~ 3% of the diameter, and reappear again, at an even longer wavelength, as shown in Figure 5.22. This occurs because at a given filling fraction, the effective refractive index of the void space (including the infiltrated material) will equal that of the silica spheres, the opal will become optically uniform, and the photonic band gap will disappear. This behavior was also predicted by Blanco, et. al., where they calculated a different position for the gap closure for CdS infiltration (n= 2.4) theoretical models where the filling is homogenous (21% filling of void space) and the filling is conformal (38.4% filling).[26]

The unnormalized specular reflectivity in Figure 5.21 confirms this progression, as the Γ-L peak shifted to longer wavelengths after a projected 2.5 nm coating (0.7% of diameter), shifting to 737 nm, and then disappearing after a 5.0 nm coating (1.43% of diameter). The peak reappeared at a 820 nm after a 10 nm coating (2.8% of diameter), and shifted further to 875 nm, becoming more pronounced after a 20 nm coating (5.7% of diameter). These peak shifts correspond to 13.4%, 40.8%, and 64% infiltrations for the 2.5, 10, and 20 nm infiltrations (note: the Γ-L peak has disappeared after the 5 nm infiltration, making filling fraction calculation using the Bragg equation impossible).

Comparison of these filling fractions with the Monte Carlo theoretical filling curve in Chapter 4 (Figure 4.12), allows the actual coating thicknesses to be estimated; these were found to be 2.64, 9, and 15.5 nm, respectively. The data shows that the disappearance of the PPBG occurs between 13.4 and 40.8% infiltration at approximately 30-35%, which is roughly between the homogenous and shell-growth infiltration model predicted by Blanco (ZnS's refractive index is only slightly less than CdS's). This could indicate that the infiltration layers are not entirely conformal, rather that the volume is partially filling homogeneously. However, for the TiO_2 infiltrations discussed in Chapter 6, the PPBG also disappeared at a shorter wavelength than the conformal model predicts, while SEM analysis suggested that the infiltrations are extremely conformal. Likewise, generation of the dielectric function required to calculate the band diagram for infiltration shells with small thickness to sphere diameter ratios is difficult. A high resolution grid must be used to represent the infiltrated material, or it is likely that the overall dielectric constant will be underestimated. It is possible that the shell growth dielectric function generated for this calculation underestimated the dielectric constant, resulting in an overestimation of the required infiltration amount for disappearance of the Γ-L PPBG.

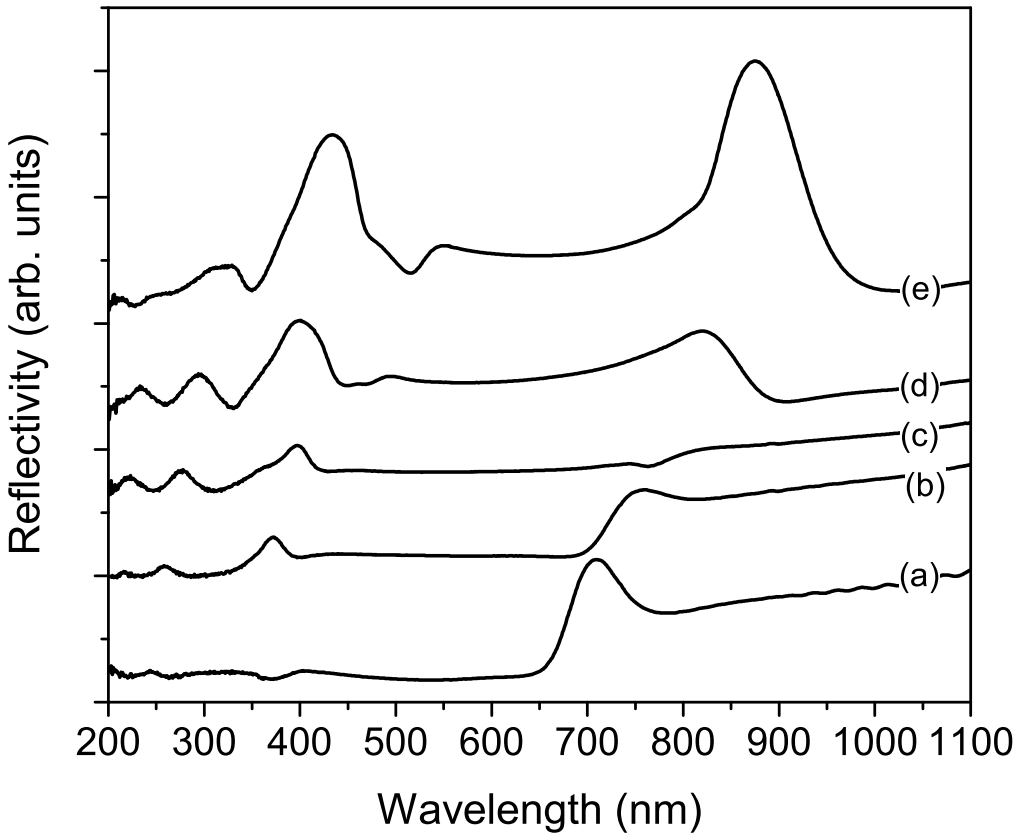

Figure 5.21 Specular reflectivity evolution during infiltration of a 330 nm opal. (a) as-sintered, and infiltrated with (b) 2.5, (c) 5, (d) 10, and (e) 20 nm of ZnS:Mn.

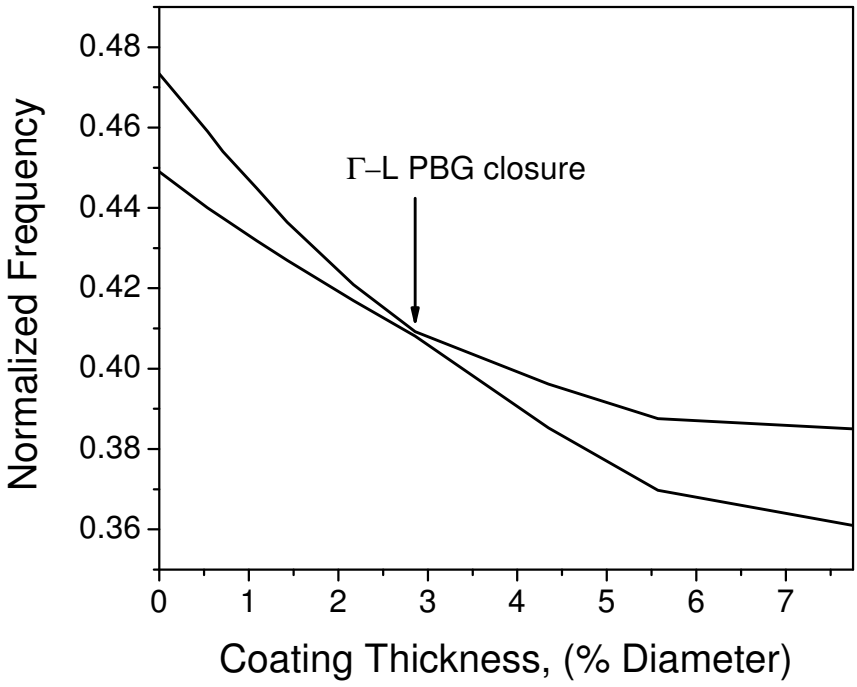

Figure 5.22 Calculated Γ-L band gap width as a function of coating thickness for shell growth (PWE method).

The same reflectivity measurements were performed on the 440 nm opal, as shown in Figure 5.23. The first layer was predicted to be 2.5 nm, and yielded a shift of the primary diffraction peak from 954 nm to 983 nm, yielding a filling fraction of 8%. When compared with the theoretical filling model, this is equivalent to a coating thickness of 0.5 % of the diameter, or 2.2 nm, slightly less than predicted. As previously discussed, the 330 nm opal displayed a effective coating thickness of 2.6 nm. While this is perfectly within the realm of experimental error, it is also likely that the increase in the ratio of the sphere diameter to the coating thickness resulted in a more uniform infiltration in the 440 nm opal, which would yield a lower effective coating thickness. The 5 nm infiltration resulted in the disappearance of the Γ-L peak, as before, and the 10 and 20 nm infiltrations resulted in peak shifts to beyond 1100 nm, past the limit of detection for the Beckman DU-640. However, each filling increment yielded an increase in the flat band photonic band gap peak intensities (the data is not normalized). These peaks were located at the same photon energy as the ZnS:Mn emission peak (~ 400 – 650 nm), allowing demonstration of the modification of spontaneous emission using PL measurements of these samples, as discussed in the next section.

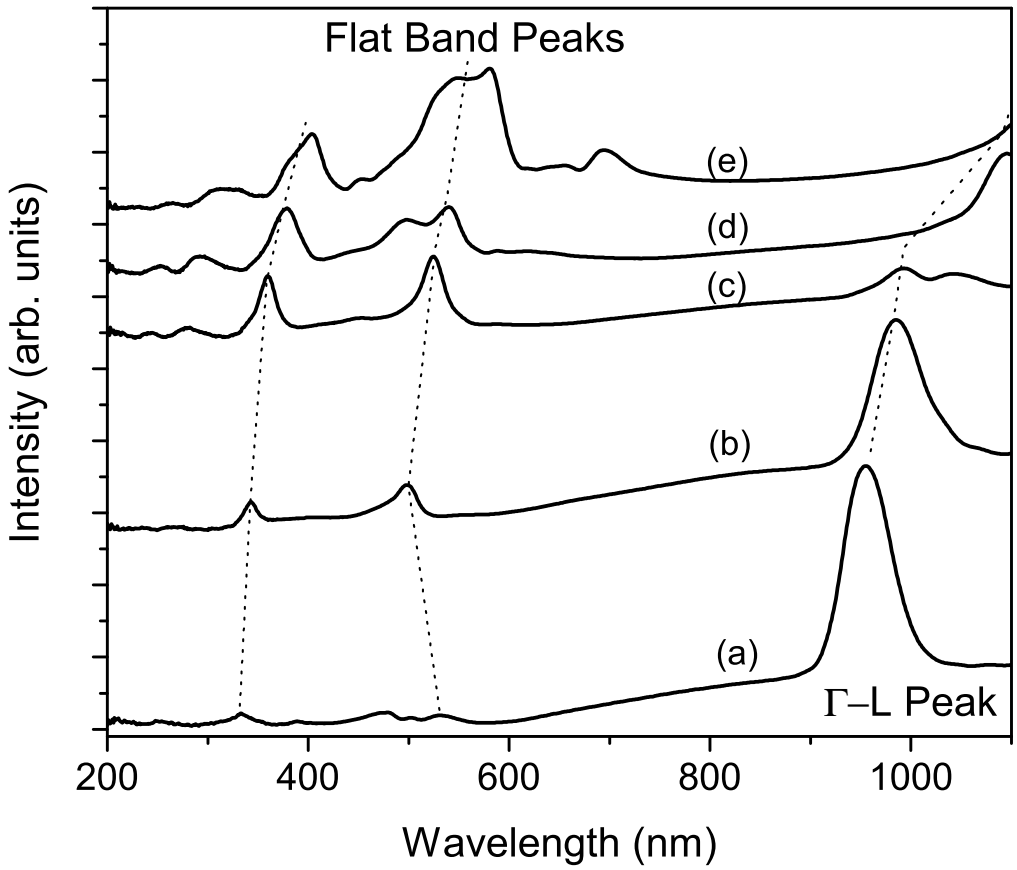

Figure 5.23 Specular reflectivity for 440 nm (a) sintered opal, and after infiltration with (b) 2.5, (c) 5, (d) 10, and (e) 20 nm of ZnS:Mn. (Spectra are not normalized, but shifted for comparison)

5.2.2 Photoluminescence: Spontaneous Emission Modification

Photoluminescence of the stepwise infiltrated opals was measured using 45º incident 337 nm pulsed UV excitation using the setup as described in Chapter 4. Figure 5.24 shows the resulting PL for a 440 nm opal that was infiltrated with 2.5, 5, 10 and 20 nm of ZnS:Mn, with the reflectivity data (normalized to the flat band peak). This size opal was designed to develop peaks in the specular reflection that were located favorable for demonstration of modification of photoluminescence using the flat band peaks. After infiltration with 2.5 nm of ZnS:Mn, the emission behavior indicated by the solid red curve was measured. It shows the typical 460 nm and 585 nm emission peaks, with the 585 nm peak intensity lower in magnitude than the 460 nm peak. The reflectivity peak located between the two peaks at 500 nm, has a low intensity, as previously shown in Figure 5.23 for the unnormalized data. Infiltration with 5 nm of ZnS:Mn yielded the emission characteristics shown by the dashed green curve. The 585 nm peak increased relative to the 460 nm defect peak, and the reflectivity peak shifted to 525 nm and increased in magnitude. For the 10 nm infiltration, the 585 nm peak was significantly reduced relative to the 460 nm peak, and the reflectivity data showed two flat band peaks, located at 500 and 540 nm, as indicated by the dotted blue curve. After 20 nm of ZnS:Mn infiltration, the 585 relative peak flattened out, when compared to the 460 nm peak, as shown by the short dotted magenta curve. It may be reasonable to postulate that the decrease in the 585 nm peak intensity is an effect independent of the photonic band behavior of the material, such as doping irregularities, or increased concentration of Cl^- defects with the increased film thickness. However, this will be more fully discussed in Chapter 7, where during formation of a multilayered structure using the same sample, the

relative height of the 585 nm peak was increased while at the same time shifting the flat band peak to longer wavelengths than the emission peak. The increase in the peak height when comparing the 2.5 to 5 nm infiltration is likely due to increased effectiveness of the modified Mn^{2+} doping routine with the increased film thickness. The 2.5 nm infiltration received only one doping pulse, while the 5 nm infiltration had 2.

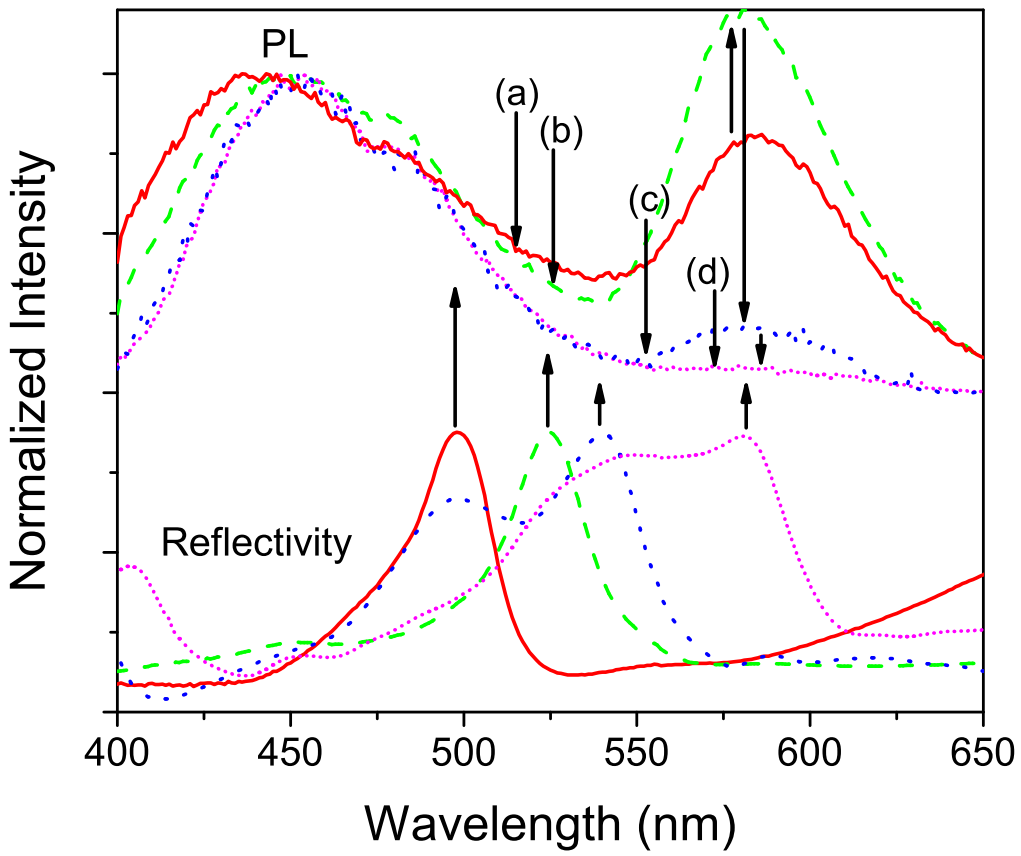

Figure 5.24 Photoluminescence data for stepwise infiltrated 440 nm opal, compared with 15° reflectivity data. (a, solid) 2.5 nm ZnS:Mn, (b, dash) 5 nm ZnS:Mn, (c, dot) 10 nm ZnS:Mn, and (d, short dot) 20 nm ZnS:Mn infiltrations.

CHAPTER 6

FABRICATION OF TIO_2 INFILTRATED AND INVERSE OPALS

The ALD infiltration study was next extended to TiO_2, a candidate material for use in PCs, because its refractive index (n) can exceed 2.8 and 2.65 (λ=500 nm) for the rutile and anatase phases, respectively, as previously shown in Figure 3.4. [40, 55, 69, 70] The infiltration methods used to date have resulted in filling fractions of at most 50% of the available pore volume, not enough to form a full PBG. In addition, these opals were infiltrated either by solution precipitation, or by nanoparticle co-sedimentation, neither of which offered precision in the placement of the high dielectric material. Infiltration by ALD holds promise for attaining inverse "shell" opals that exhibit filling fractions very close to the optimum 90% of the pore volume.

6.1 Experimental Details

For this study, TiO_2/SiO_2 infiltrated and TiO_2 inverse opals were formed by ALD infiltration of silica opals in a hot-wall reactor. Two systems were used for ALD growth, including the same Microchemisty, Ltd. F120 tool that was used for ZnS:Mn growth (Chapter 5), and a custom built TiO_2-specific system, both of which were described in Chapter 4.

ALD growth was performed by alternating pulses of $TiCl_4$ and H_2O precursors, each separated by a N_2 purge.[78] From planar growth studies, a growth rate of ~ 0.98 Å/cycle was found for deposition at 100° C. [74] After application of the necessary

number of pulse/purge cycles, for opals that were infiltrated at 100° C, the ALD reactor was heated to 400° C and held for 2 hours to convert the amorphous TiO_2 film to polycrystalline anatase. As with the ZnS:Mn inverse opals discussed in chapter 5, the silica spheres were removed using a 2% HF solution. However, the TiO_2 infiltration proved to be far more dense than the ZnS:Mn, making removal of the spheres impossible without opening a pathway to the silica though the deposited film. So, prior to etching, an ion mill was used to remove the thin TiO_2 capping layer from the surface of the infiltrated opal, thus exposing the silica spheres and facilitating their removal. Following deposition, specular reflectance, transmission, x-ray diffraction, and scanning electron microscopy (SEM) were used to characterize the structures.

6.2 Preliminary Studies Using F120 System

The ZnS:Mn infiltrated opals in chapter 5 revealed that for opals sized ~ 200 – 250 nm, infiltration did not fully penetrate the film, but rather formed a hollow inverse opal. This was attributed to a combination of problems, dominated by insufficient pulse and purge lengths to fully saturate the surface, but also possibly including pore clogging from due to grain growth at the elevated deposition temperature. The TiO_2 infiltration experiments were initially performed in the same reactor, the Microchemistry, Ltd. F120 tool, located at the U.S.Army Research Laboratory in Adelphi, MD. For these depositions, incomplete infiltration was also observed, to a more severe degree than for the ZnS:Mn infiltrations. The first depositions were performed with the standard TiO_2 recipe as provided in the F120 manual, which was 220 ms $TiCl_4$ pulses, followed by a

550 ms N_2 purge, a 550 ms H_2O pulse, and another 550 ms N_2 purge, with a deposition temperature of 500° C. Opals sized from 190 – 265 nm were infiltrated, resulting in poor infiltration, with only the very top layer of the opal having any significant filling. For the 190 nm opal, the Γ-L peak was found to shift from 414 nm to 425 nm, indicating that only 6% of the void space was infiltrated. For the 200 nm opal, the peak shifted from 444 nm to 455 nm, again only displaying 6% infiltration. For the 265 nm opal, the peak shifted from 584 nm (measured at 8° from normal incidence) to 589 nm (measured at 15° from normal incidence), which again corresponds to 6% void infiltration, as shown in Figure 6.1. As expected, with such a low filling fraction of TiO_2, it was impossible to make an inverse opal by removal of the silica spheres with HF. When attempted, the films disintegrated.

The second set of TiO_2 infiltrations in the F120 reactor were performed after discovery of the "hollow chip" infiltration problem with ZnS, so it was anticipated that increasing the pulse and purge times would improve the TiO_2 infiltration. Consequently, the pulse and purge times were all increased to 2 seconds. In addition, runs were performed at 100° C, as well as 500° C. The resulting infiltrations were greatly improved over those with very short pulse lengths, at both temperatures but still exhibited reflectivity behavior that was consistent with an incomplete infiltrated opal. For these samples, there was typically one large, broad peak that was consistent with where the Γ-L peak should shift to for an infiltrated opal with a high filling fraction of TiO_2, as well as a sharper peak at short wav. However, there were also other peaks in the spectra at shorter wavelengths that suggested that the interior of the opal had a different diffraction peak, i.e. different filling fraction of TiO_2, from the outside layers. Another improvement from

the short pulse/purge run was that the inverse opal was successfully formed by etching the opal in HF. Figure 6.2 shows reflectivity data for 210 nm sintered, infiltrated, and inverse opals.

Figure 6.2 illustrates that the Γ-L peak was initially at 470 nm, prior to infiltration. Infiltration with TiO_2 caused the formation of a broad peak centered at 600 nm, as well as two small peaks at 500 and 460 nm, which arise from incomplete infiltration. A strong set of peaks also form from 330 nm to 422 nm, due to both the existence of flat bands in the dispersion relation (group velocity anomaly) and PPBGs of higher order. These peaks were present in the fully infiltrated samples discussed in section 6.3, so they arise from the fully infiltrated portion of the opal. However, the complex situation of an infiltrated opal film with incomplete infiltration makes the optical properties difficult to comment on with 100% certainty. Typically, incomplete infiltration was indicated by the presence of one or two peaks in the reflectivity spectra close to the original position of the Γ-L peak of the sintered opal. These peaks are not predicted to exist by the calculated photonic band diagrams.

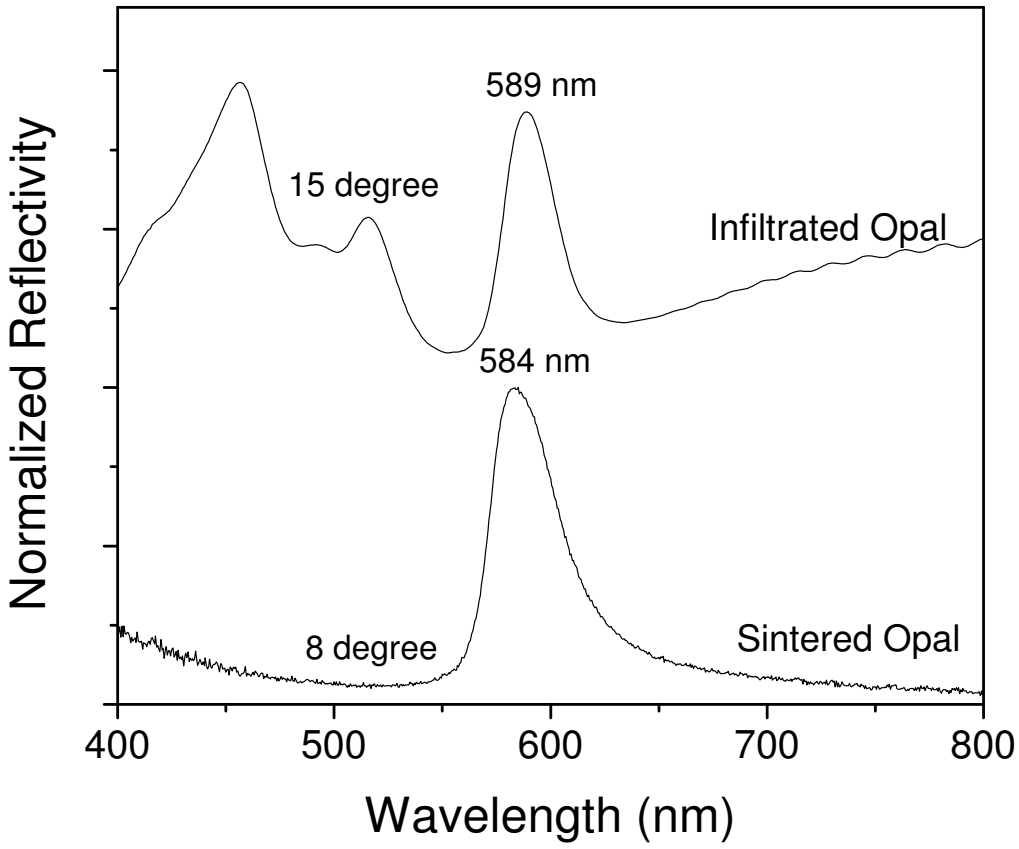

Figure 6.1 Reflectivity measurements for 265 nm opal (8°) and infiltrated opal (15°), formed by ALD of TiO_2 at 500° C, with 220 ms $TiCl_4$ pulses, 550 ms H_2O pulses, and 550 ms N_2 purges, in the F120 ALD reactor.

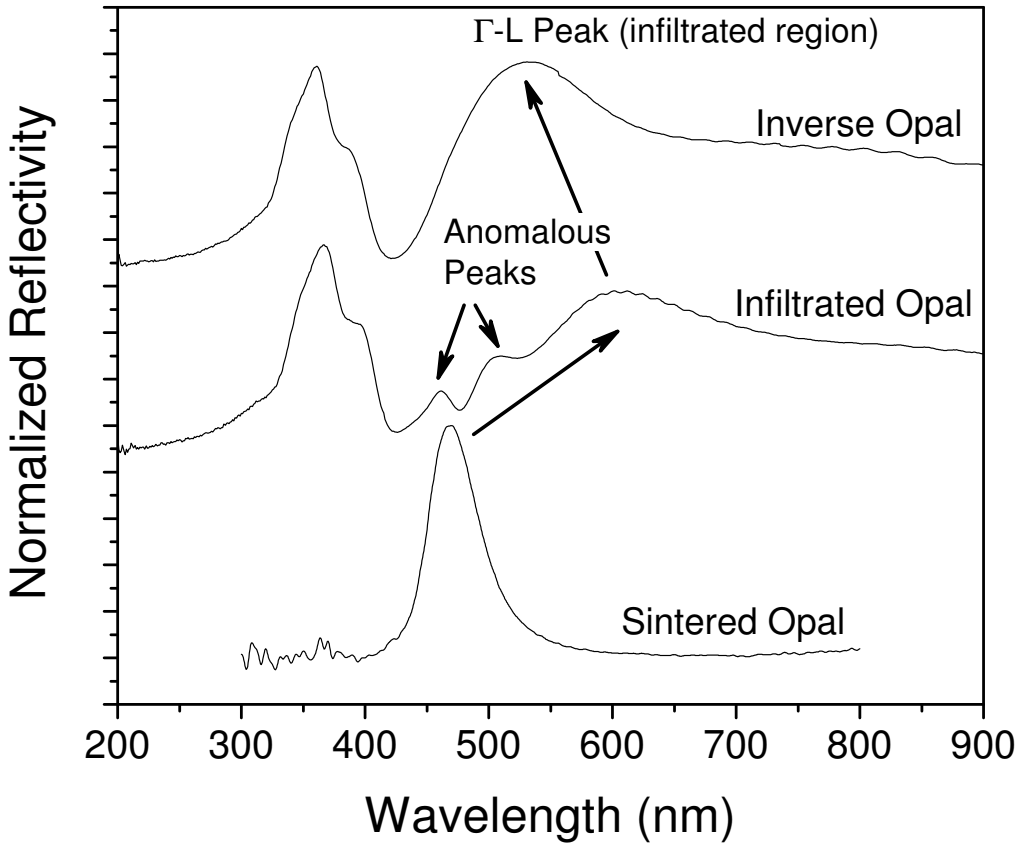

Figure 6.2 Reflectivity measurements for 210 nm opal, infiltrated opal, and inverse opals, formed by ALD of TiO_2 at 500° C, with 2 second pulses and purges.

The deposition temperature was next reduced to 100° C, while still maintaining pulse and purge lengths of 2 seconds. After deposition, the infiltrated opals looked much better than those infiltrated at high temperature, exhibiting more uniform and brighter diffraction colors. However, reflectivity measurements revealed that the opals were still incompletely infiltrated, and the two peaks previously observed between the Γ-L primary and the flat band peaks were still present, as shown by Figure 6.3. However, the broad peak corresponding to the Γ-L photonic band gap created by the fully infiltrated region of the opal was much more well defined than for the opal infiltrated at 500° C. These experiments revealed that obtaining a fully infiltrated opal would require more versatility than the F120 system offered, so a custom system was built for growing TiO_2.

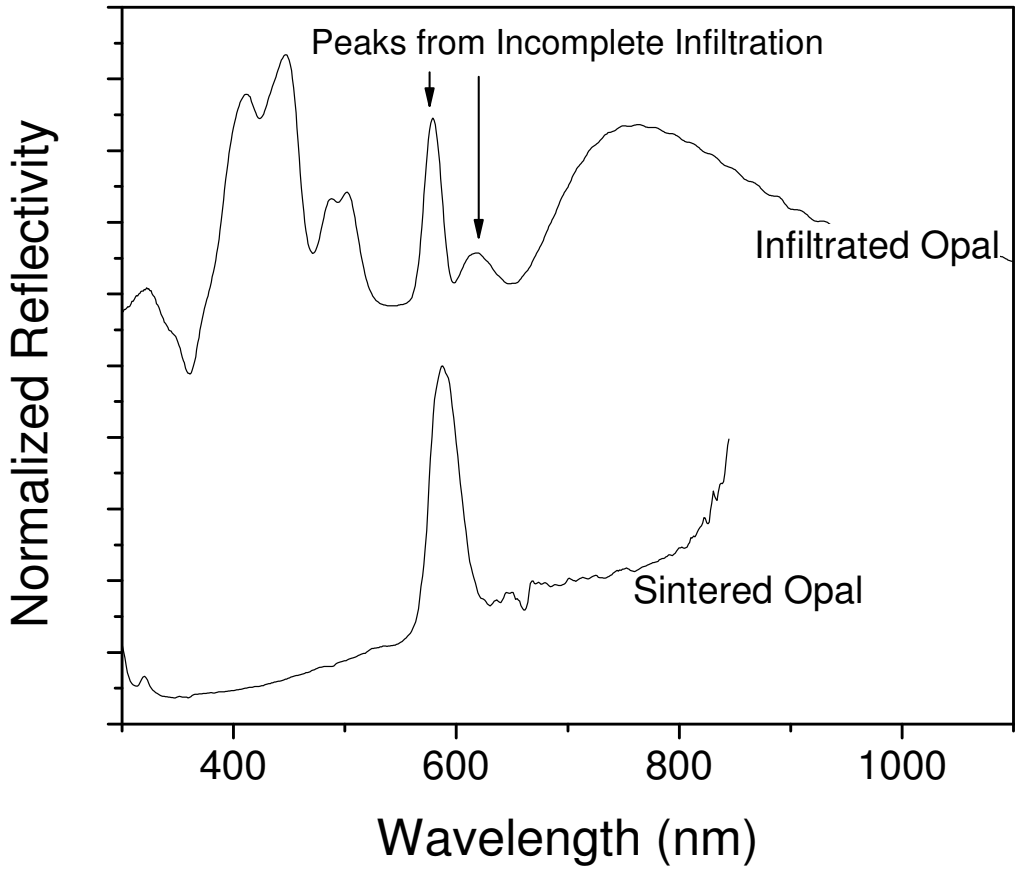

Figure 6.3 Reflectivity measurements for 265 nm opal and infiltrated opal formed by ALD of TiO_2 at 100° C, with 2 second pulses and purges.

6.3 Low Temperature Infiltration

The custom ALD reactor as described in Chapter 4 was used for low temperature infiltration studies. The decision to deposit at low temperatures was driven by the need to minimize surface roughness within the photonic crystal. Surface roughness negatively affects the optical properties of the structures (increases optical loss, for one), and makes multi-layered infiltrations difficult, one of the main goals of this thesis. Also uneven growth within the opal pore volume limits the ability to fully infiltrate the opal, and yields porosity. Since previous studies by Aarik, *et. al* revealed that growth of TiO_2 at 100° C yielded very smooth films, with low optical losses, this temperature was chosen for ALD infiltration. [87] Initially, planar growth experiments were performed in order to characterize various parameters such as growth rate and surface roughness, as well as testing the system to ensure that self-limiting growth was occurring. [74]

From atomic force microscopy (AFM) studies of the planar films, TiO_2 coatings yielded RMS roughness values of 0.2 nm at 100˚ C, 2.1 nm at 300˚ C, and 9.6 nm at 600˚ C.[60] Thus, to promote even filling and extremely smooth interfaces, very low temperature deposition was found to be essential. The level of improvement in film smoothness is shown by Figures 6.4 and 6.5, which are SEM images of planar ALD film cross sections, deposited at 100° C, and 500° C, respectively. The same level of improvement was found for the infiltration of opals, as shown in Figures 6.6 and 6.7, which are SEM images of the opal surfaces infiltrated with TiO_2 at 100 ° C (partially infiltrated to show conformal coating) and 500° C, respectively. The opal infiltrated at low temperature clearly has been coated with a conformal layer of TiO_2, as indicated by

the shape retained by the remaining air channels, and there is very little surface roughness. However, the opal deposited at 500° C clearly has poor surface quality. It is impossible to even tell that the structure is an opal.

High temperature growth is undesirable because instead of forming a continuous film, an island growth mechanism occurs during deposition. [78] The film does not grow uniformly across the surface of the sphere, or substrate as would be the case if growth was epitaxial, but rather tends to form by nucleation and growth of many small crystallites. Figure 6.8 is an SEM of the (111) surface of a 433 nm opal that was infiltrated with a very thin layer of TiO_2 at 600° C, illustrating the occurrence of island growth. The resulting small crystallites enlarge with further deposition, yielding surfaces as shown in Figures 6.5 and 6.7. Surface roughening during ALD has been attributed to surface migration of intermediate reaction products, as well as to gas phase reactions (reaction above the substrate, instead of on it). [78] Because of this, the film grows by enlargement of nucleated islands both normal to and parallel to the substrate, yielding a rough, textured surface. This decreases the growth rate of the film, for example in the case of the opal in Figure 6.8, the deposition should have yielded a ~10 nm film, based on planar film growth studies.

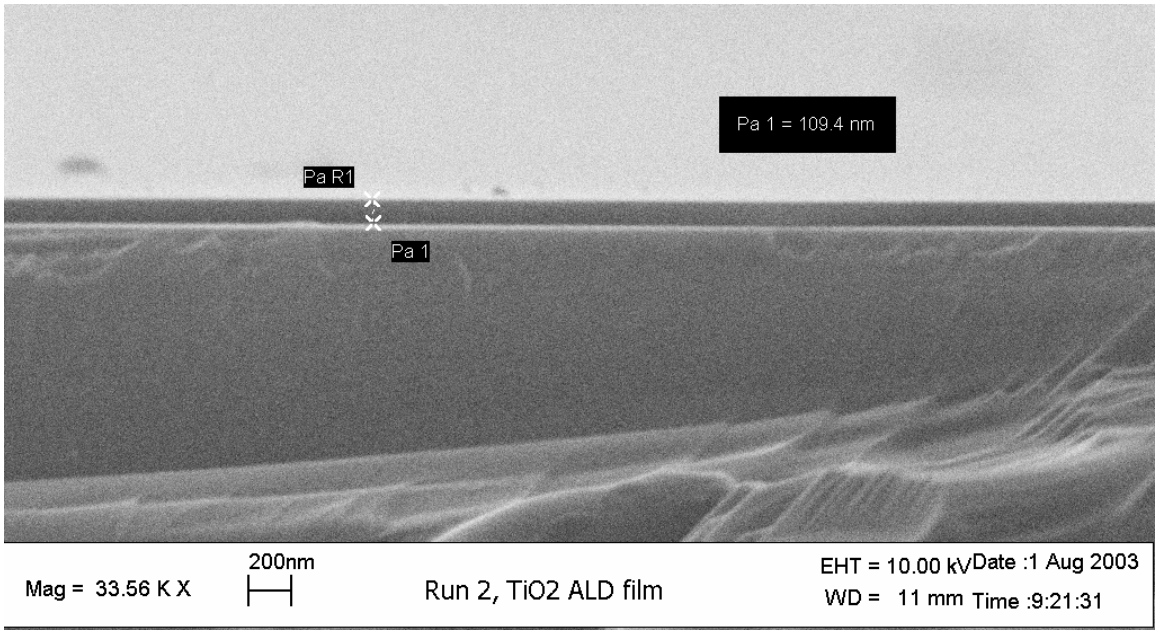

Figure 6.4 ALD planar TiO_2 film deposited on a bare silicon wafer at 100° C, ~ 100 nm thick. Film is bracketed by measurement indicators.

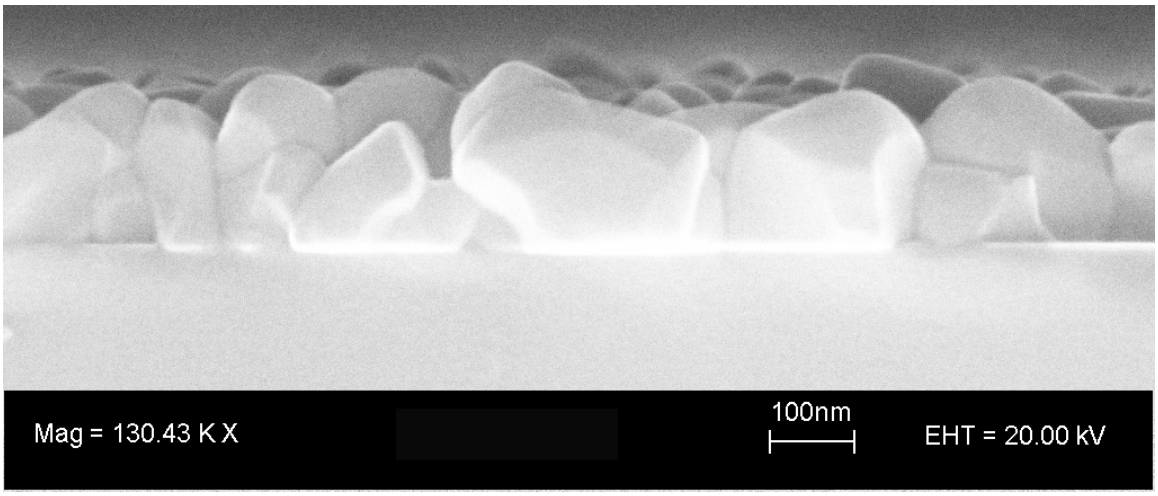

Figure 6.5 ALD planar TiO_2 film deposited on a bare silicon wafer at 500° C, ~ 100 - 200 nm thick.

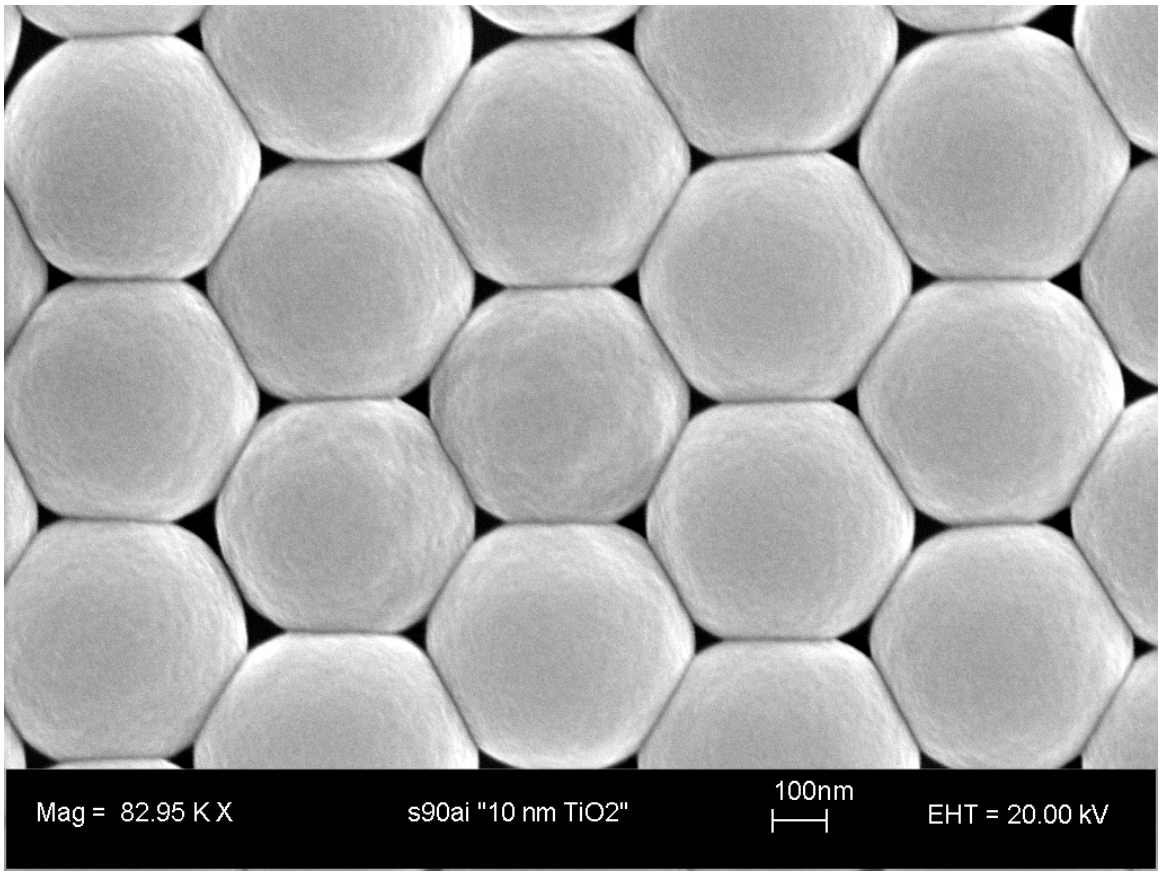

Figure 6.6 Top surface of 433 nm opal partially infiltrated at 100° C with TiO_2.

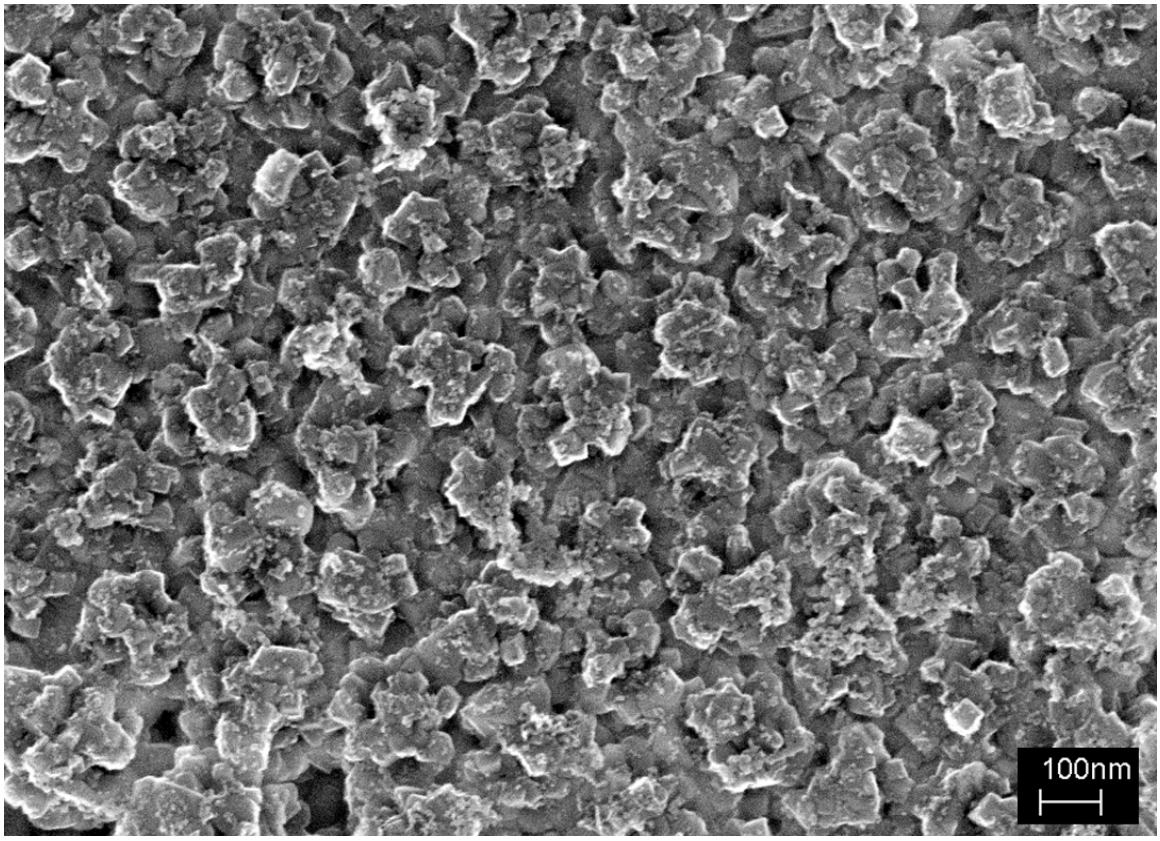

Figure 6.7 Top surface of TiO_2 opal infiltrated at 500° C.

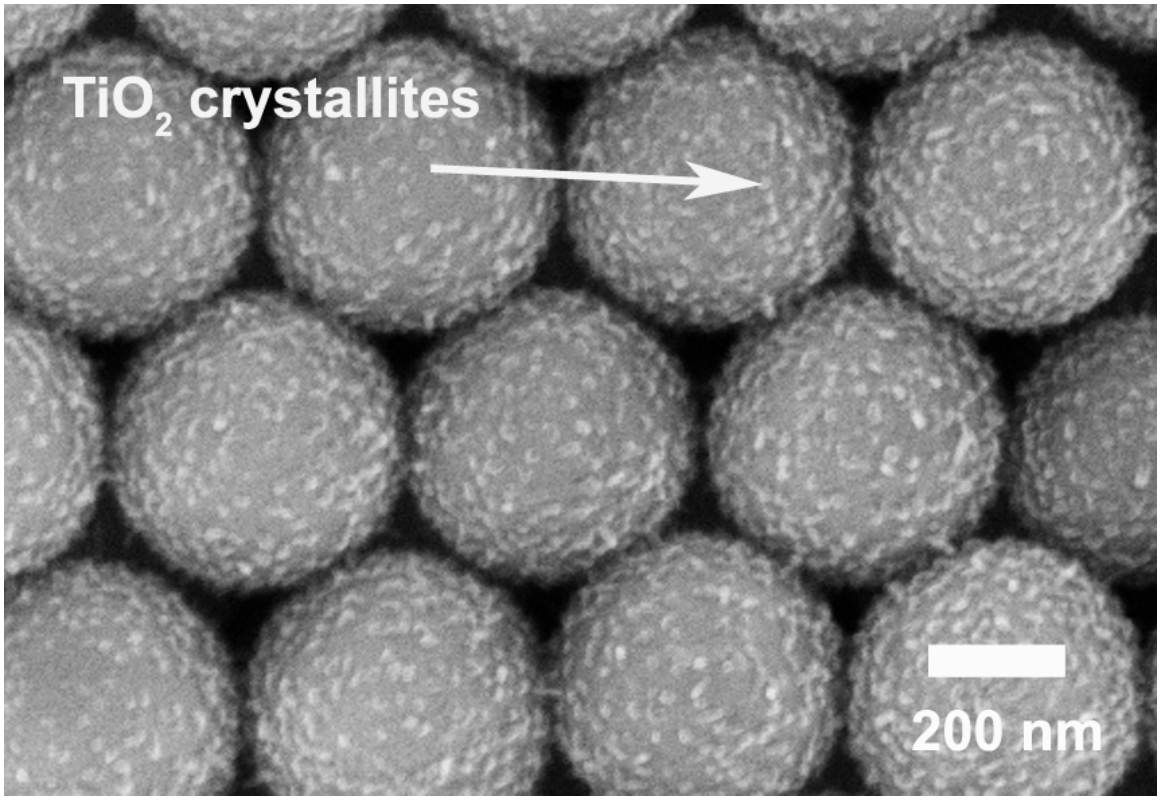

Figure 6.8 SEM of the (111) plane of a 433 nm opal partially infiltrated with ~ 2.5 nm of TiO_2 at 600° C.

While close observation of the crystallites reveals that they have dimensions of about 10 nm, the opal has not been filled with an amount of material equivalent to a 10 nm thick conformal film. From reflectivity measurements, it was found that the Bragg peak for this sample shifted from 935 nm to 979 nm after "10 nm" was deposited. This peak shift corresponds to ~ 11% infiltration of the available pore volume. Comparing this calculation with the Monte Carlo filling fraction as a function of coating thickness curve discussed in Chapter 4, an equivalent film thickness of 2.77 nm, or about ¼ the thickness predicted was found. Clearly the opal has not been infiltrated with a continuous, conformal film, so this number only serves as a qualitative comparison to the amount of material that was predicted to be deposited.

Shifting to low temperature infiltration facilitated complete filling of the opal, which was confirmed from SEM analysis and reflectivity measurements. SEM analysis was the only certain way confirm that infiltration completely penetrated the opal. If the infiltration extended several optical absorption lengths from the surface, as was the case with ZnS (Chapter 5), the reflectivity measurements did not reveal any peaks from the low filling fraction region for TiO_2. Pulse and purge lengths of 2 sec. were used initially, but these proved to be too short for full infiltration, and the structure shown in Figure 6.9 resulted. Clearly there is significant infiltration, but below the surface, there still remained an unfilled volume. After increasing pulses and purges to 4 and 10 sec., respectively, full infiltration was observed, as shown in Figure 6.10, which is an SEM of a 433 nm inverse opal crystal fracture surface, viewed from 45 degree incidence. Further analysis of fully infiltrated opals, including specular reflectivity and SEM images are presented in sections 6.5 and 6.6.

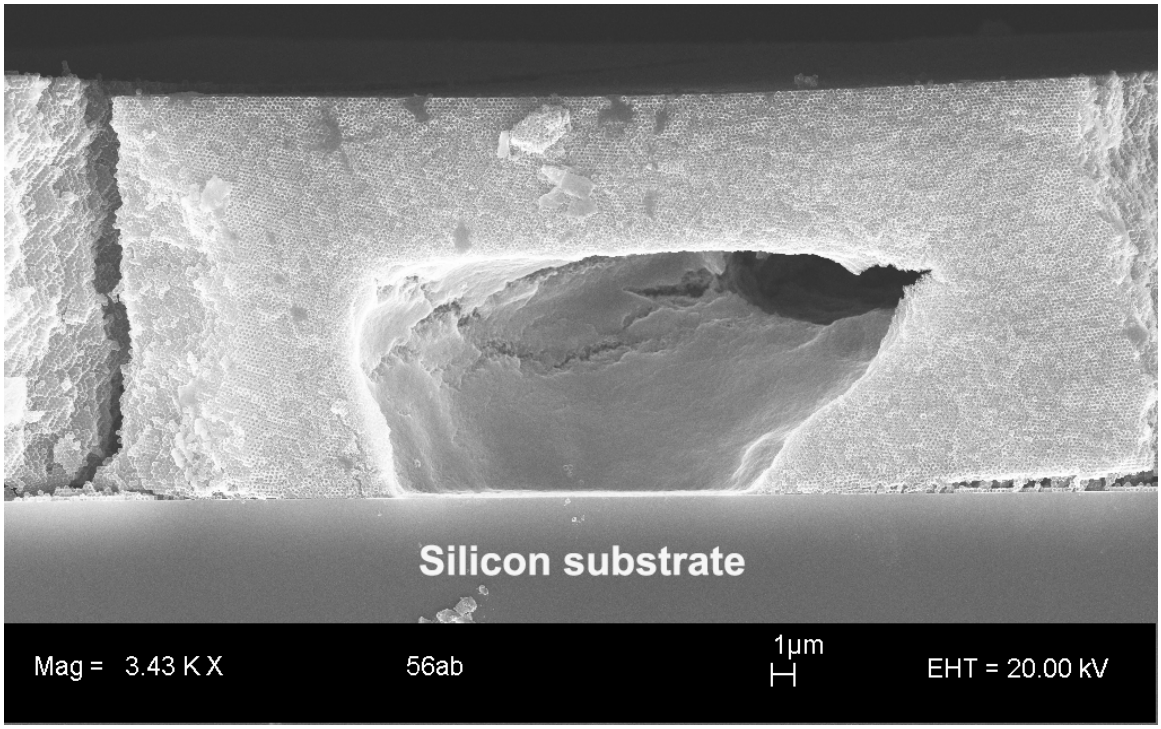

Figure 6.9 SEM image of incompletely infiltrated 200 nm TiO_2 inverse opal and fracture surface.

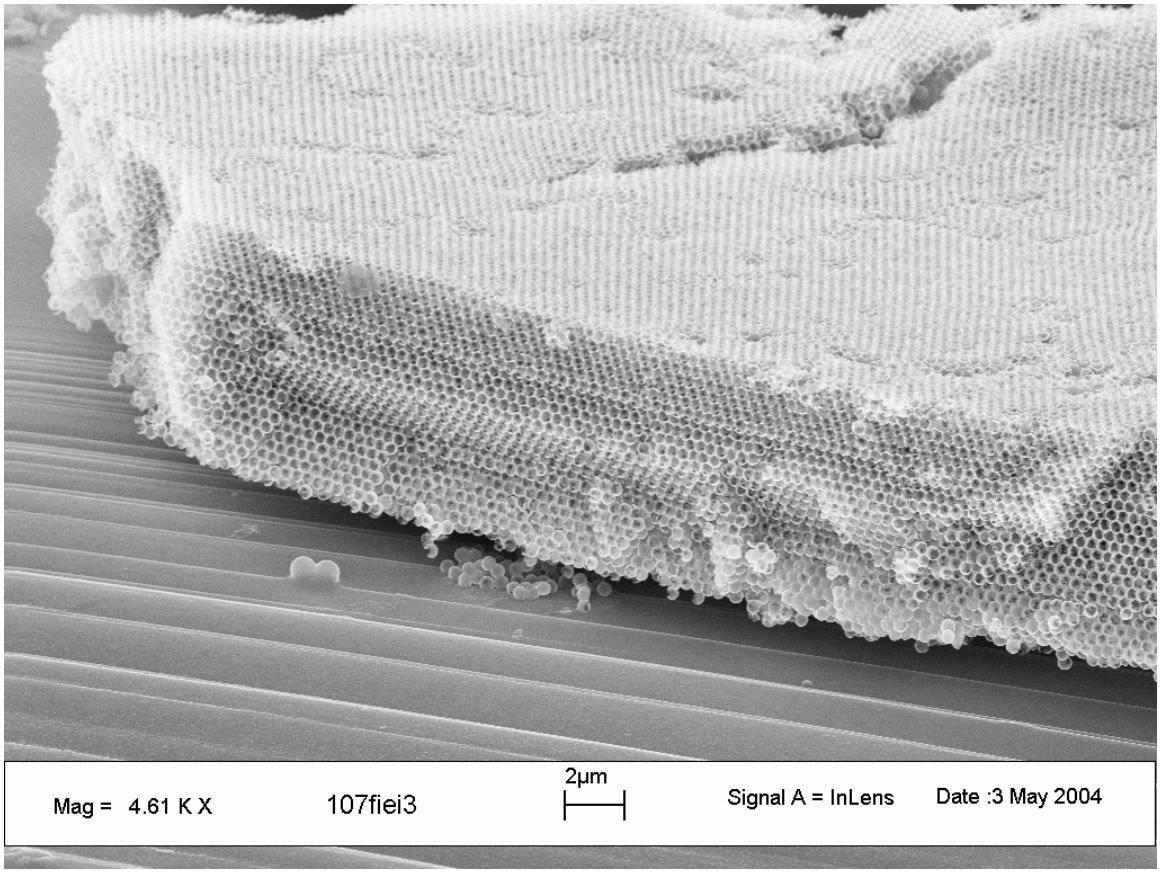

Figure 6.10 Lower magnification SEM image of 433 nm TiO_2 inverse opal and fracture surface.

6.4 Post-Deposition Heat Treatment

Deposition at 100° C resulted in formation of amorphous TiO_2 films, whose refractive index of 2.35 at 600 nm, is significantly below that obtained in anatase or rutile films (see Figure 3.4).[69, 87] This study also revealed that the formation of the inverse opal by etching the SiO_2 spheres requires crystalline TiO_2; otherwise, HF etches the amorphous phase, destroying the sample. Therefore, we developed a technique that combined deposition at low temperature with a subsequent heat treatment to promote formation of the anatase phase while maintaining good infiltration and smooth films. Figure 6.11 shows XRD spectra measured after infiltration, and after a post-deposition heat treatment. The as-infiltrated case shows a very broad peak at 22°, and a strong peak at 69°. The broad peak is characteristic of amorphous material, and arises from both the amorphous SiO_2 spheres and the infiltrated amorphous TiO_2. The sharp peak is from the (400) planes of the (100) silicon substrate. After heat treating the opal for 2 hours at 400° C, in nitrogen, the anatase phase was successfully formed. The peaks in Figure 6.11 that correspond to the formation of the anatase phase are indicated, indexed with the respective crystallographic planes. All peaks were attributed to either the anatase phase, or the silicon phase (substrate).

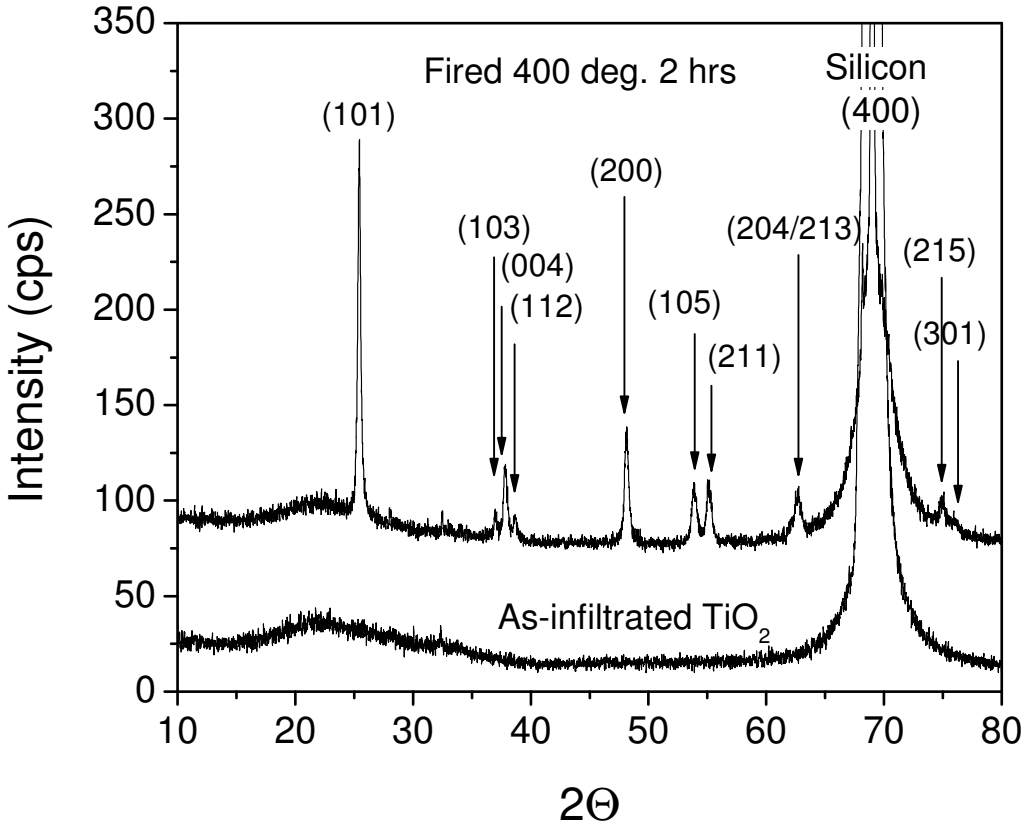

Figure 6.11 XRD data for 100°C 433 nm infiltrated TiO_2 opal (lower curve), and same sample after 400°C 2 hour heat treatment (upper curve).

AFM studies of planar films showed an increase in RMS roughness of only 0.2 nm after conversion to anatase, resulting in a film roughness significantly lower than directly grown anatase (2.1 nm for films deposited at 300° C). The reduction of roughness is evident in the results presented in section 6.5, especially in Figure 6.16. Attainment of 100% rutile phase was difficult, and involved heat treatments at temperatures above 1100° C, which is too high for the SiO_2 opal to survive. However, the anatase phase of TiO_2 has a refractive index greater than 2.85 for wavelengths shorter than 400 nm,[70] and should allow formation of a full PBG for ultraviolet wavelengths, as well as exhibit strong PPBGs in the visible. The anatase phase also exhibits far less birefringence than rutile, which makes both theoretical and experimental analysis easier.

6.5 Scanning Electron Microscopy of Inverse Opals

SEM was used to confirm the successful infiltration of the opal with TiO_2 and to examine the degree of conformality of the resulting films. Figure 6.11 – 6.14 shows SEM images of the (111) top plane of a 433 nm inverse opal, showing a cross-sectional view of the anatase TiO_2 infiltration layer. The sample was prepared by ion milling the sample until the top half of the first layer of air spheres was removed, allowing characterization of the film thickness and conformality. Figure 6.11 is a lower magnification image, showing the long range ordering found, and is tilted slightly. Figures 6.13 and 6.14 are higher magnification images, further illustrating the highly conformal nature of the film, as clearly demonstrated by the presence of small air pockets between the air spheres. Figure 6.15 is an image of a fracture surface of a portion of the opal that has been

cleaved. This image clearly shows that the silica spheres have been removed, leaving a "hollow" TiO_2 inverse "shell" opal. The dark spots on the spherical surfaces are the contact points where the spheres were connected prior to fracture. The surface of the inverse opal is examined in Figure 6.16, a high magnification (~185 kx) image of the spherical shell outer surface, showing a highly conformal film, with anatase grains on the order of 5 - 10 nm in size. Unlike the case for infiltration at high temperatures, the low temperature deposition and heat treatment combination has clearly yielded an inverse opal that is highly conformal, but crystalline, with minimized anatase grain size.

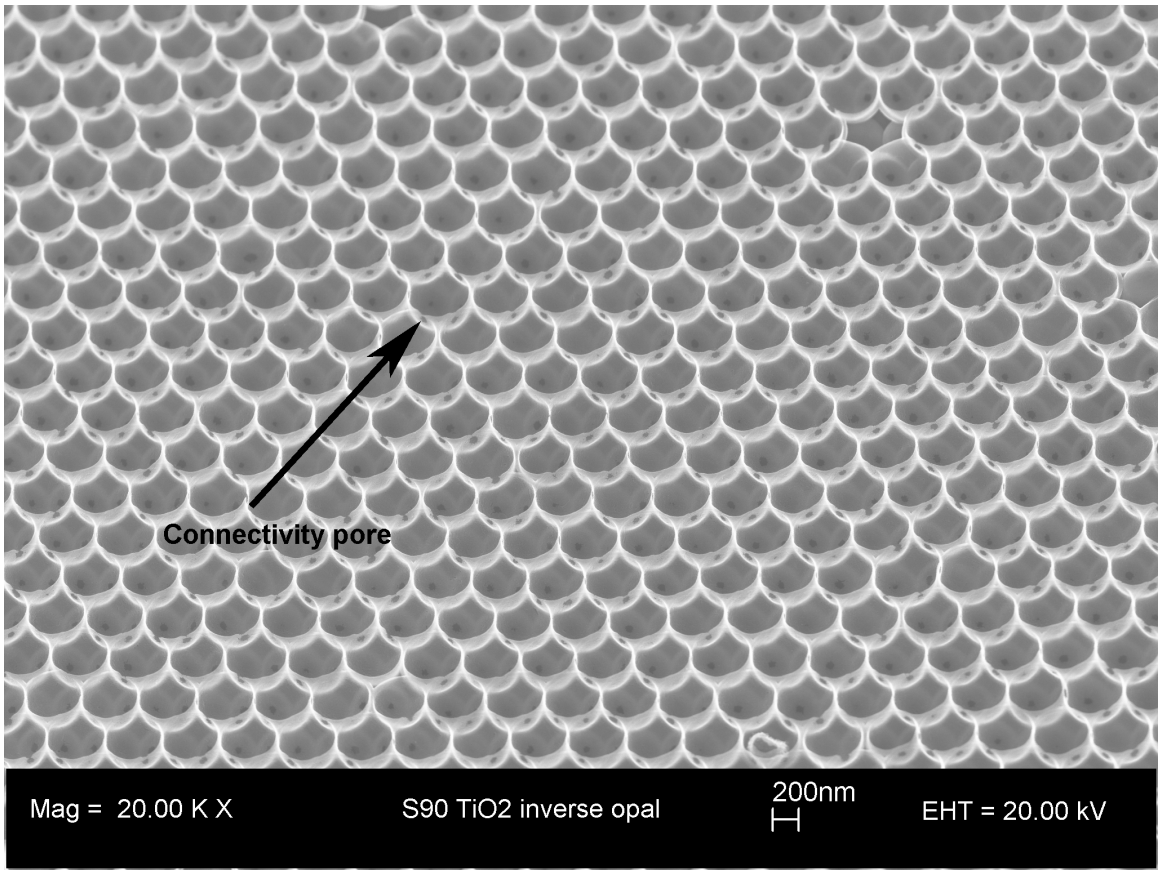

Figure 6.12 SEM of TiO_2 inverse opal surface, tilted slightly.

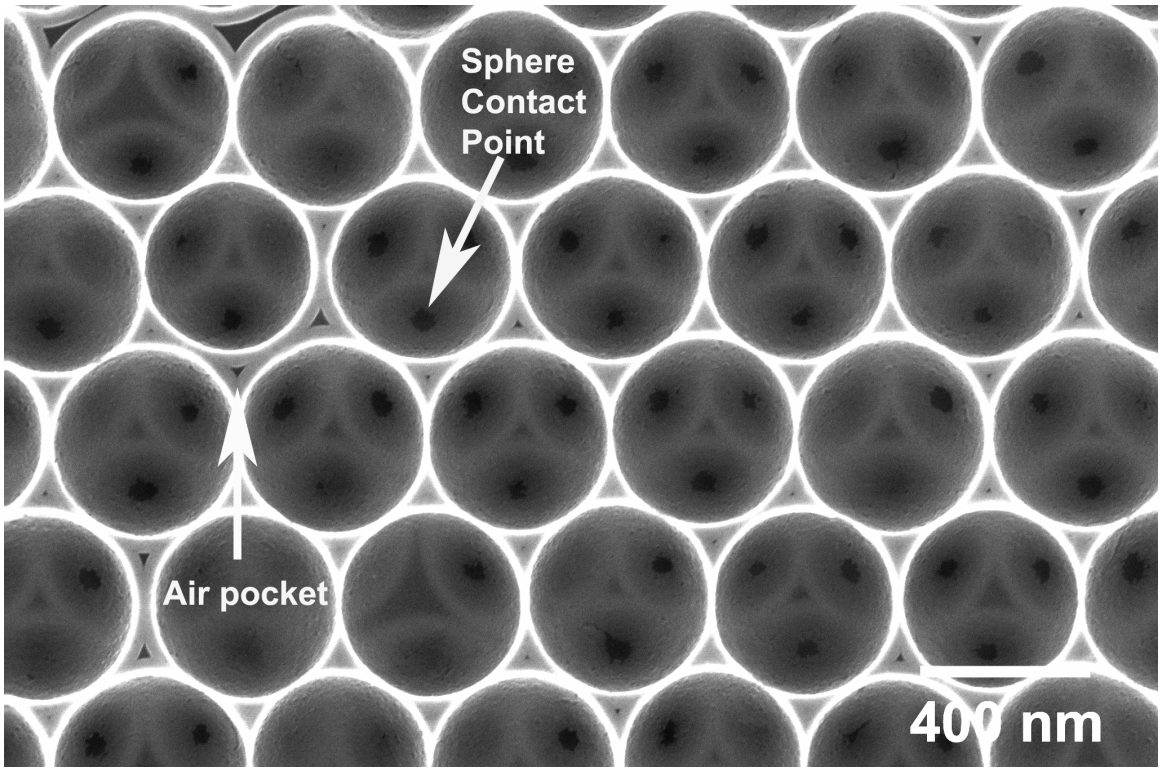

Figure 6.13 SEM image of 433 nm TiO_2 inverse opal, ion milled (111) surface.

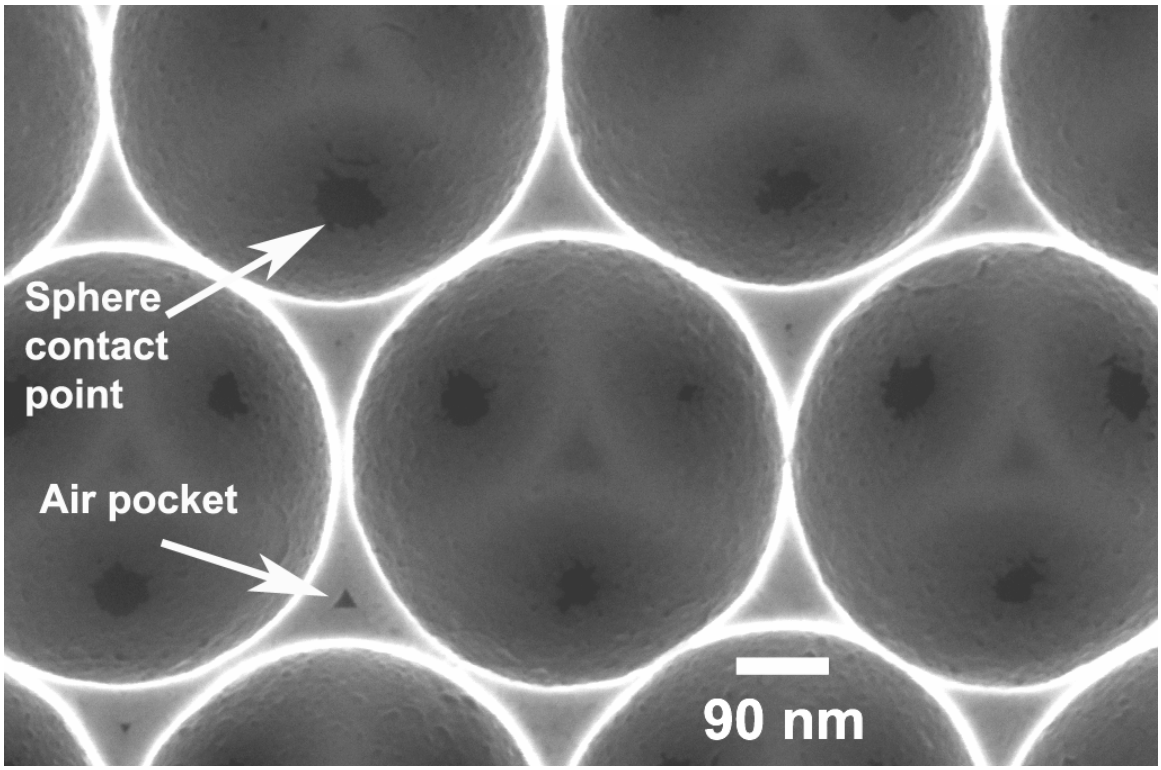

Figure 6.14 SEM image of 433 nm TiO_2 inverse opal, higher magnification ion milled (111) surface.

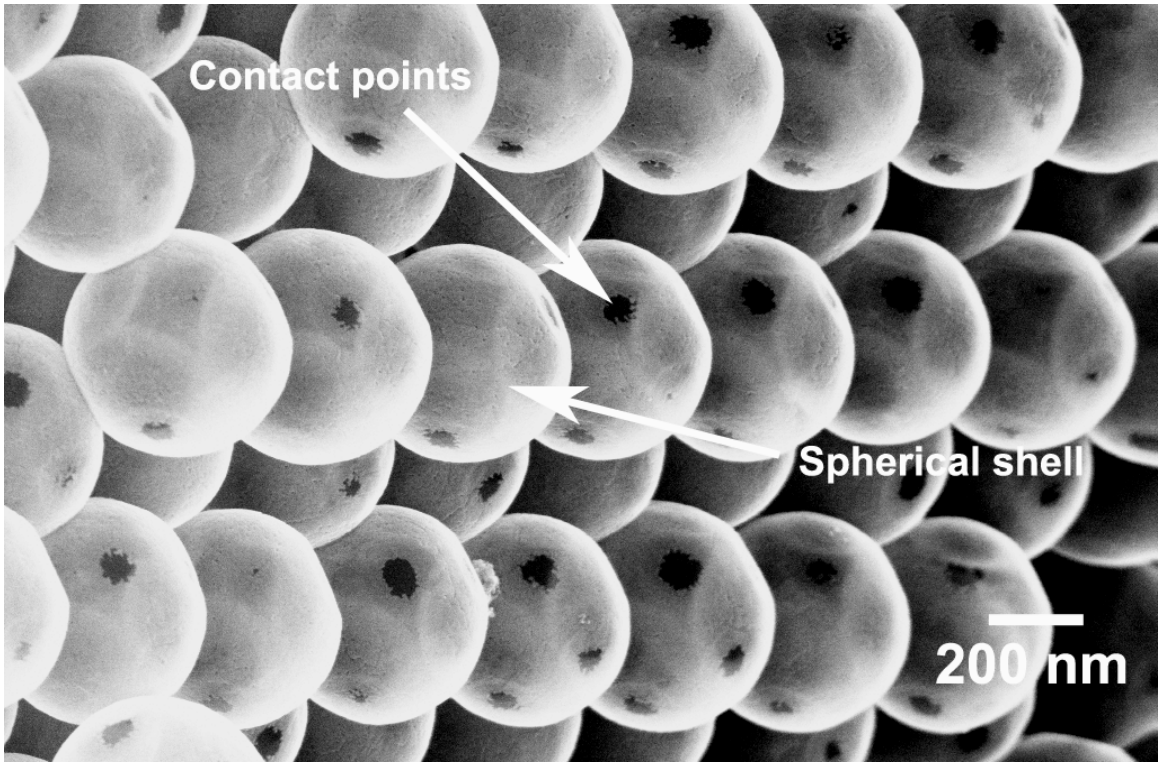

Figure 6.15 SEM image of 433 nm TiO_2 inverse opal fracture surface.

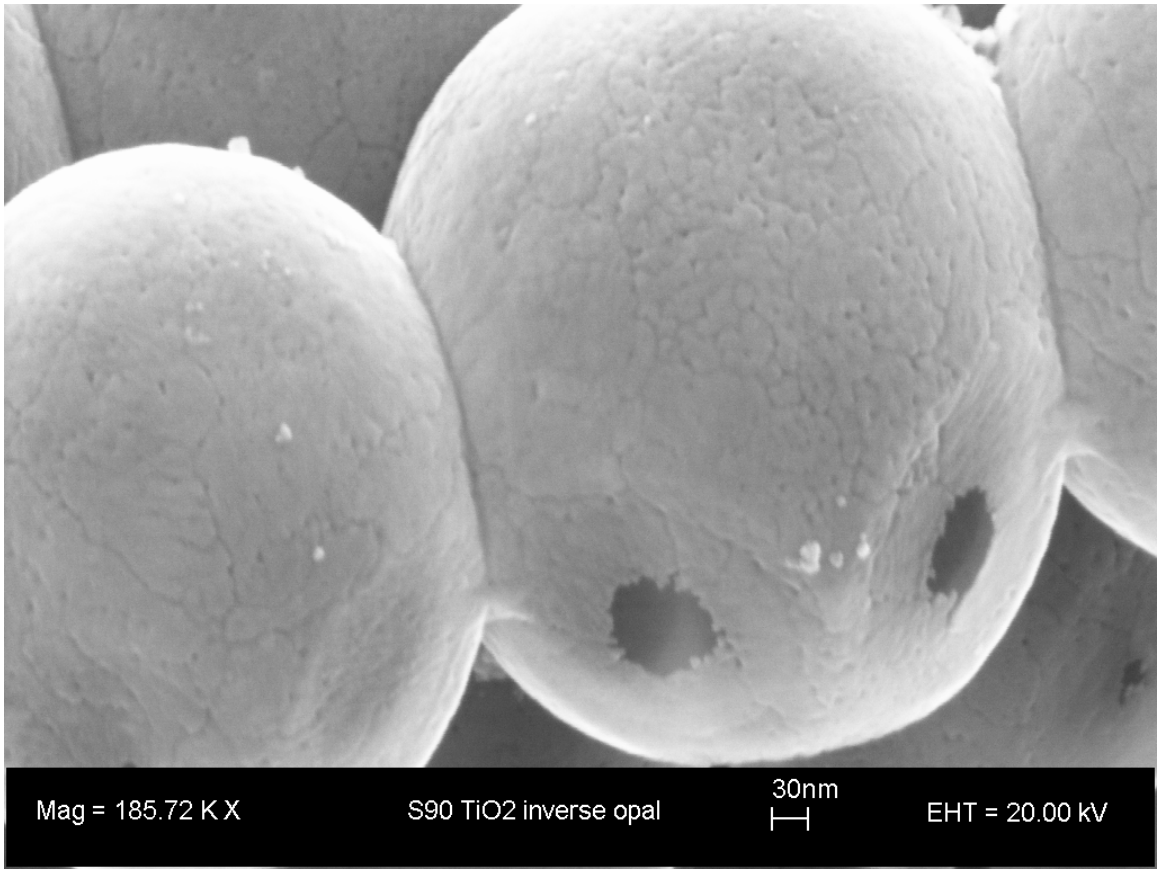

Figure 6.16 High magnification image of 433 nm TiO_2 inverse opal.

6.6 Specular Reflectivity Measurements

As discussed in Chapter 4, the successful infiltration and etching can be followed by examining the shift of the Γ-L PPBG found in specular reflectance and transmission measurements. In these experiments this peak was measured at 15° from normal incidence for reflectivity and normal incidence for transmission. Figure 6.17 shows the reflection spectra measured before infiltration, after ALD infiltration and heat treatment, and after etching during formation of a 266 nm inverse opal. The Γ-L peak shifts from 584 nm to 736 nm after TiO_2 infiltration, consistent with an increase in the average dielectric constant of the opal, and indicating 88% infiltration of the pore volume, as estimated from the Bragg equation adapted for opal structures. Formation of the inverse opal resulted in a shift of the Γ-L peak to 646 nm, consistent with a decrease in dielectric constant. As previously discussed, the theoretical maximum filling using a conformal growth method is ~ 86% of the pore volume, so the results here indicate that maximum filling has been achieved. Although within experimental error, the additional 2% above the theoretical maximum could be due to the presence of defects and lattice constant deviation that allow for more material to infiltrate. Data from progressively filling of an opal with TiO_2 until maximum filling is achieved will be presented in section 6.7.

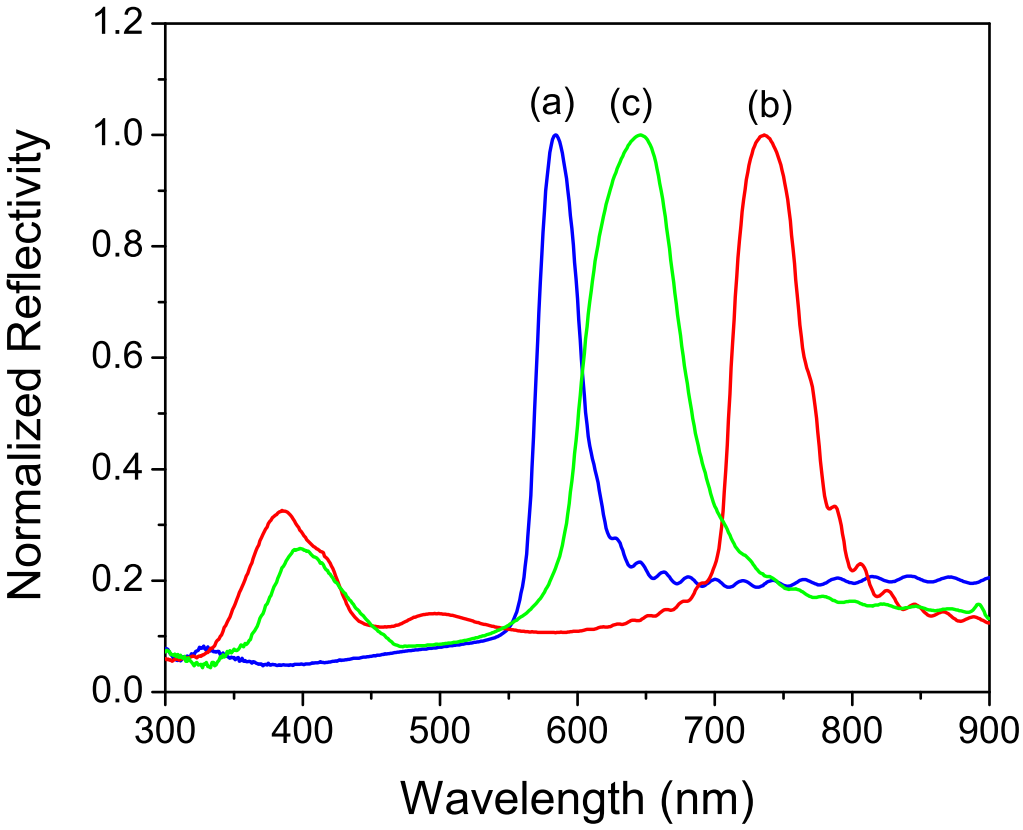

Figure 6.17 Reflectance spectra measured for 266 nm bare, infiltrated, and inverse opals (15° incidence). (a) Bare opal, with 584 nm Γ-L PBG peak, (b) as-infiltrated opal, with 736 nm Γ-L PBG peak, and (c) inverse opal, with 646 nm Γ-L PBG peak.

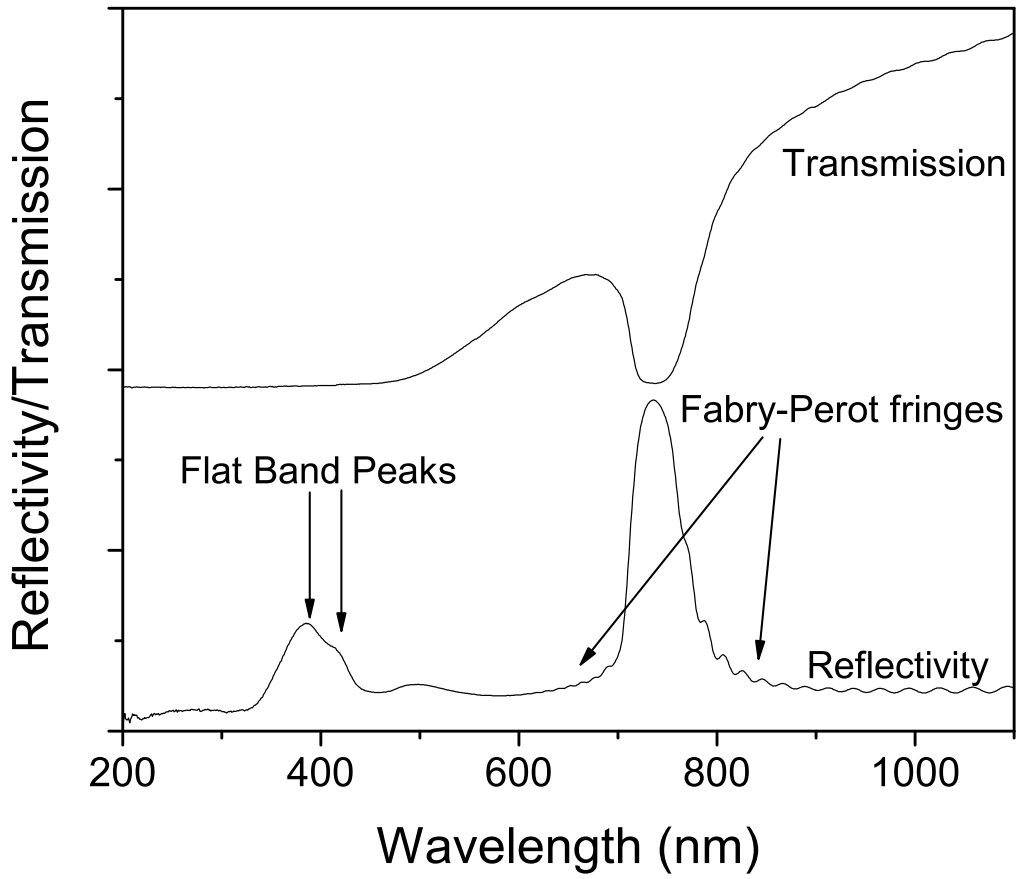

Figure 6.18 Reflectance and transmission spectra measured for a 266 nm infiltrated opal (15° incidence for reflectivity, and 0° for transmission).

Normal incidence transmission through the 266 nm sample was also measured. Transmission data for the infiltrated opal is plotted in Figure 6.18, with reflectivity for comparison, showing good agreement between the two. The FWHM of the transmission dip increased after both infiltration and inversion; from 42 nm for the bare opal, to 83 nm for the infiltrated opal, and to 104 nm for the inverse opal. These values represent gap-to-midgap ratios of 7.11 %, 11.3 %, and 16.1%, respectively. While a rigorous comparison requires more extensive calculations that take into account the divergence of the measurement beam, which should broaden each peak, these values agree well with predicted PPBG widths of 5.3%, 6.43%, and 15.7 % from the calculated band diagrams. The positions of the transmission dips were 590 nm for bare opal, 736 nm for infiltrated opal, and 647 nm for inverse opal, and also showed good agreement with the calculated band diagrams, which have PPBGs centered at 590 nm, 730 nm, and 637 nm, respectively.

In addition to the shift in the Γ-L peak, the development of higher energy PPBGs was again found. After infiltration, a reflectivity peak at 385 nm develops that is ~ 30% of the intensity of the Γ-L peak and is attributed to a higher energy band gap. This photonic band gap was not observed in the transmission data, which is attributed to increased optical absorption below 400 nm. This peak shifts to 398 nm and decreases slightly in relative intensity in the inverse opal. For larger sized opals, we have observed higher order peaks that have intensity comparable to the Γ-L peak, as shown in Figure 6.19, which is the measured reflectivity spectra for sintered, infiltrated, and inverse 330 nm opals, where the infiltration coating thickness was 25 nm, which corresponds to a filling fraction of 73.3% of the available pore volume. The lower intensity of the high-

energy peak for the 266 nm opal is attributed to increased optical absorption of TiO_2 for wavelengths below 400 nm.

In addition, there were no peaks between the high energy peaks (flat band/PPBG), indicating deeper penetration into the opal than was found for the infiltration studies using the F120 reactor. This supports the results found during SEM analysis of the opal cross sections, as shown previously in section 6.5. Also, the oscillations in the reflectivity data shown in Figures 6.17 and 6.18 arise from Fabry-Perot fringes that arise from the finite opal thickness, and are indicators of uniform film thickness. [88] Also, the presence of fringes on the short wavelength side of the Γ-L PPBG, are indicators of low roughness of the air/dielectric interface.

For comparison with experimental data, band diagrams were calculated using the PWE method for the opal, infiltrated opal, and inverse opals. Figures 6.20 – 6.22 show the reflectivity data from the previously discussed 330 nm inverse opal fabrication, compared with the Γ-L portions of the photonic band diagrams. The peaks in the reflectivity agree very well with both the PPBGs in the band diagram as well as the flat band regions. The inverse opal photonic band diagram shows four PPBGs, located between the 2^{nd} and 3^{rd}, the 5^{th} and 6^{th}, the 8^{th} and 9^{th}, and the 10^{th} and 11^{th} bands. The reflectivity data shows peaks that correspond to all of these band gaps. The photonic band gaps between the 2^{nd} and 3^{rd} bands shift to longer wavelengths, and widen after infiltration. For the inverse opal, this band gap shifts back to a shorter wavelength, and widens even further. As previously mentioned, the calculated band diagrams show gap widths of 5.3%, 6.43%, and 15.7 % for the sintered, infiltrated, and inverse opals, respectively.

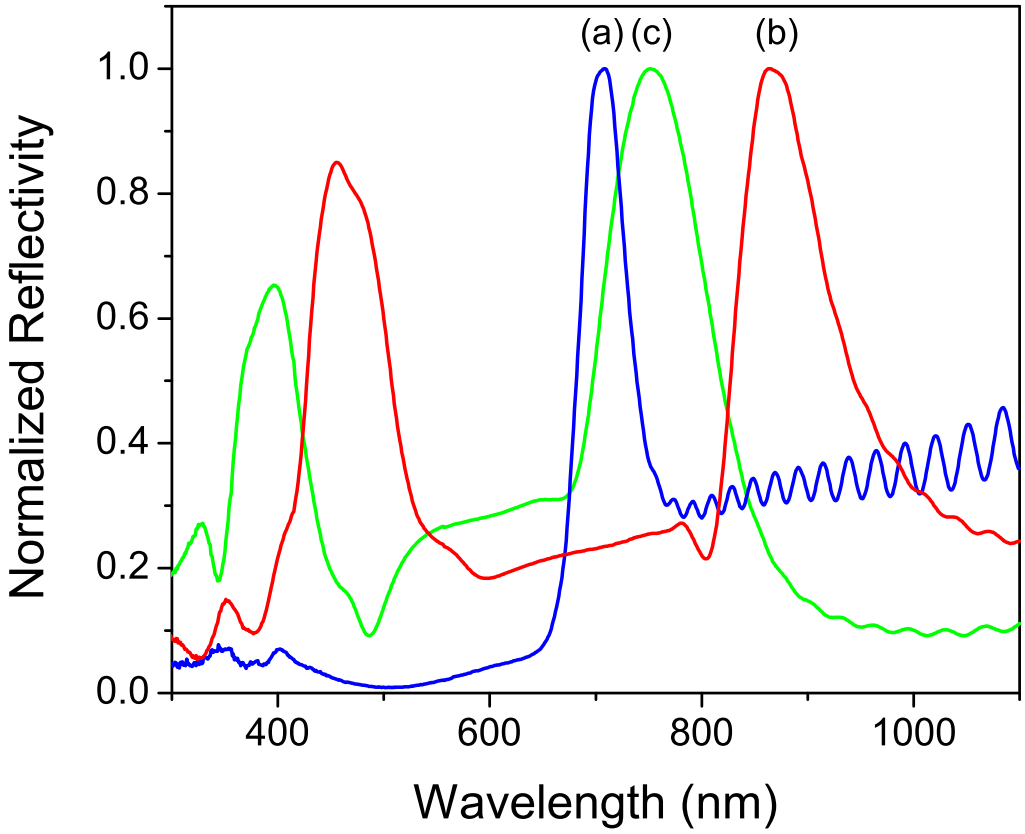

Figure 6.19 Reflectivity for 330 nm (a) sintered, (b) TiO_2 infiltrated, and (c) inverse opals.

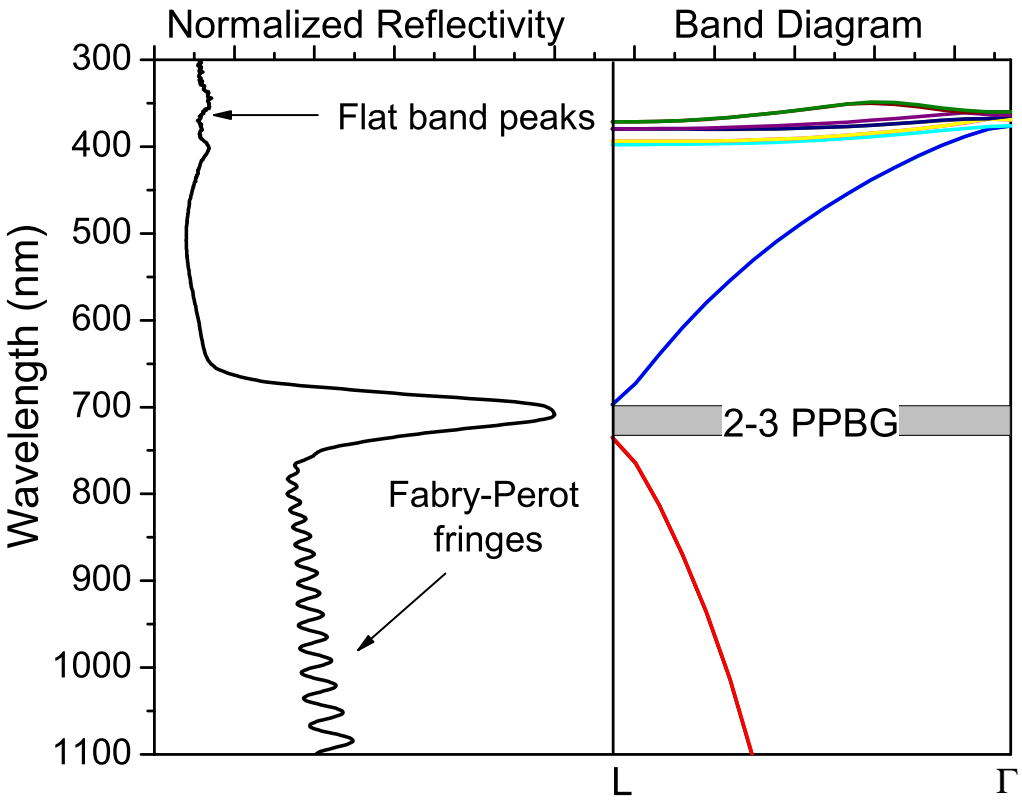

Figure 6.20 Reflectivity and Γ-L band diagram for sintered 330 nm opal.

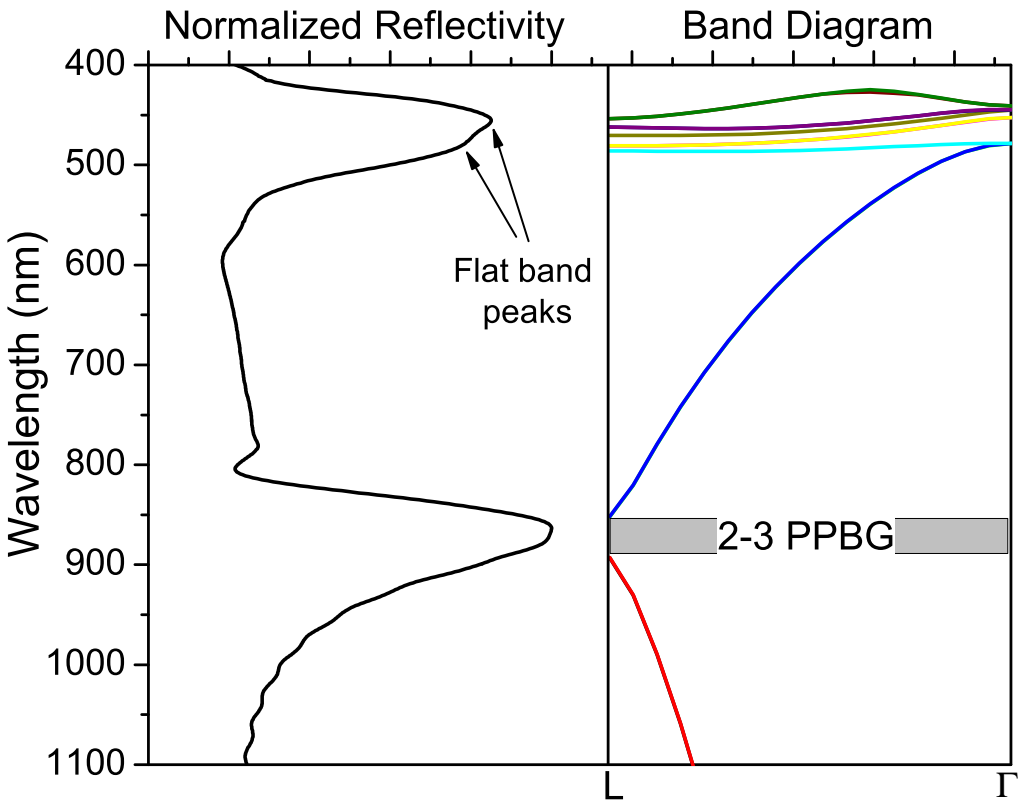

Figure 6.21 Reflectivity and Γ-L band diagram for TiO_2 infiltrated opal.

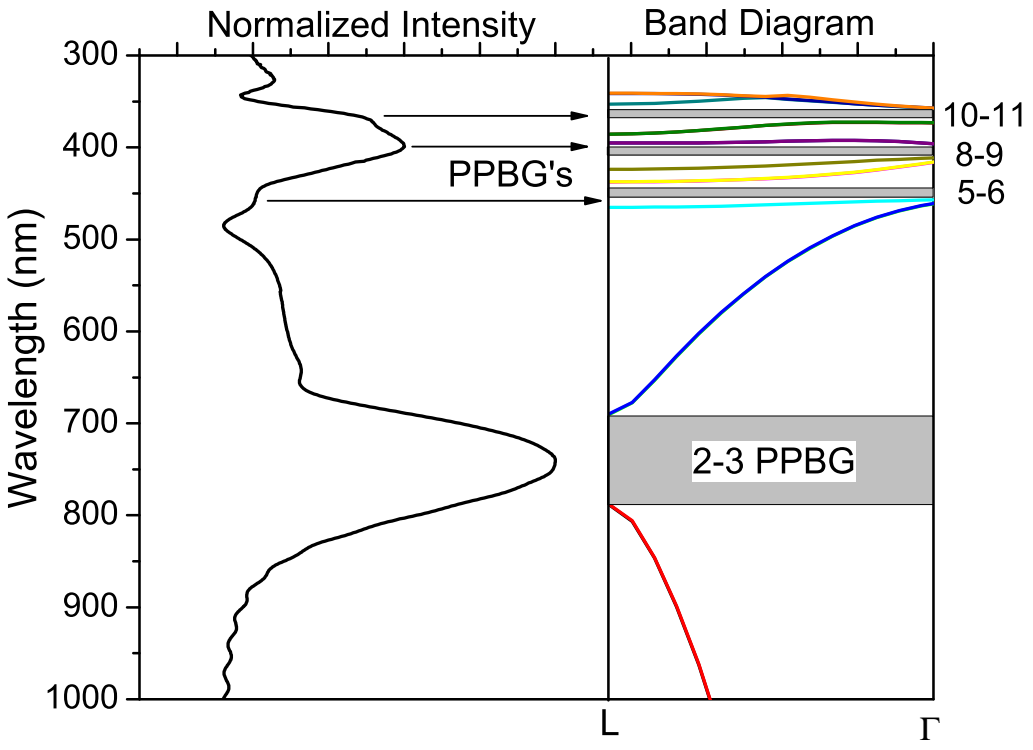

Figure 6.22 Reflectivity and Γ-L band diagram for TiO_2 inverse opal.

6.7. Titania Precise Infiltration Control

To demonstrate the control that ALD offers for TiO_2, a 266 nm opal was infiltrated in steps of 20 pulse/purge cycles, and the transmission and reflectivity were measured after each infiltration step. These measurements are summarized in Figure 6.23. The peak that begins at ~ 650 nm and shifts to ~800 nm is the PPBG between the 2nd and 3rd bands. As discussed in section 5.2.1, photonic band calculations predict that this band gap should shift to longer wavelengths with increased infiltration, close, then reopen and widen for higher filling fractions. The data shown in figure 6.23 shows this behavior, with the PPBG disappearing after 80 ALD cycles. Figure 6.24 shows the resulting void filling fraction as a function of number of ALD cycles, demonstrating the precision that can be achieved in deposition. There is no data point for 80 ALD cycles, because the PPBG peak has disappeared, preventing calculation of the filling fraction. Monte Carlo calculations predict that the (111) plane will close at ~86% infiltration (Figure 4.12), as indicated in Figure 6.24 by the dashed line. While the experimental data clearly indicates that this maximum infiltration amount has been achieved by the 350th ALD cycle, it is also important to notice that no change in filling fraction occurs after the last 20 ALD cycles, indicating that access to the remaining porosity in the structure has been closed, as predicted. The data indicates a final filling fraction of 88%, which is remarkably close to the 86% predicted by simulation. The figure clearly indicates that for the first 80 cycles a different a different trend is followed than for the last 300 cycles. This is likely due to the fact that the layers that grow on the opals in the first 80 cycles make a larger contribution to the filling fraction than do the layers in the later cycles. The data matches well with

that predicted by the aforementioned Monte Carlo simulations. Figure 6.25 shows the void space filling as a function of coating thickness, calculated by comparing peak positions with calculated photonic band diagrams for the shell infiltrations, with the theoretical filling behavior shown for comparison. In the figure, the Monte Carlo simulation data is shown as the solid line, for comparison. The resulting coating thicknesses were then plotted as a function of ALD cycles, as shown in Figure 6.26. The slope of the trend line reveals a growth rate of 0.51 Å per cycle, approximately half that of the planar growth rate. As with the previous figures, the gap in the figure is due to the disappearance of the PPBG peak. This lower growth rate indicates that the interior surface of the opal is not reaching full saturation. Thus, although the coatings are uniform, the growth rate could be increased by further optimizing the ALD conditions.

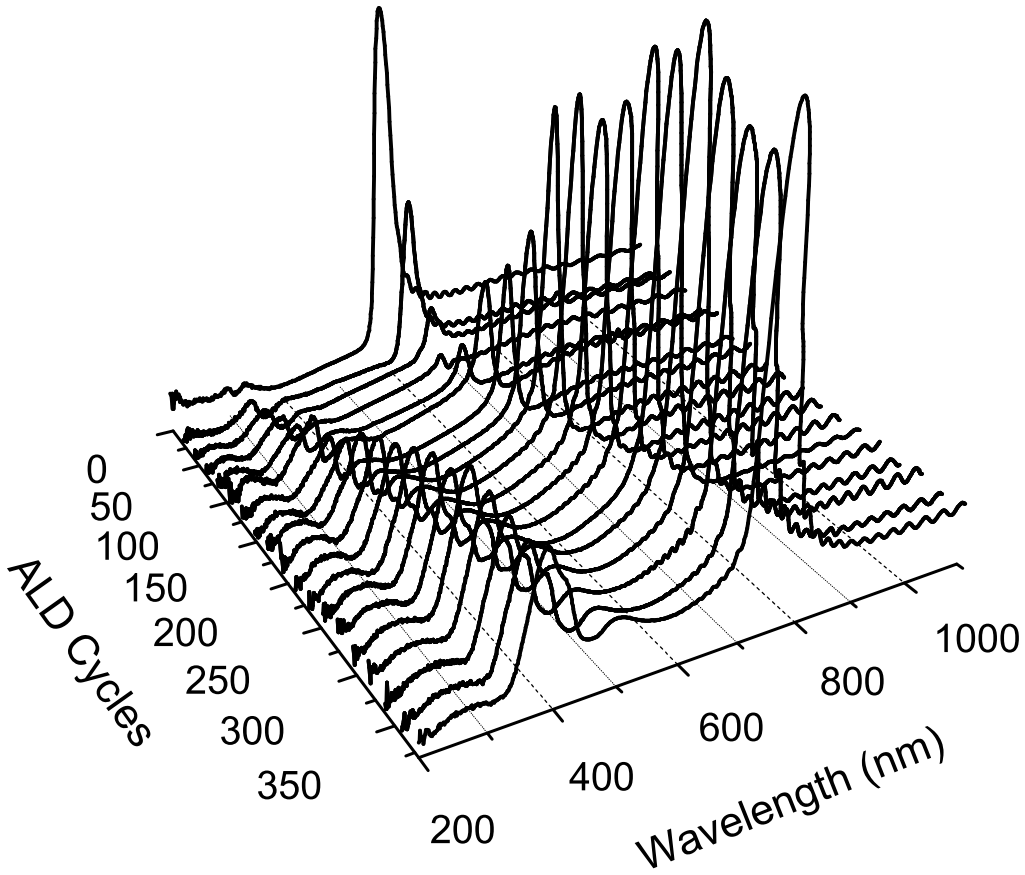

Figure 6.23 Reflectivity data collected during progressive infiltration of 266 nm silica opal.

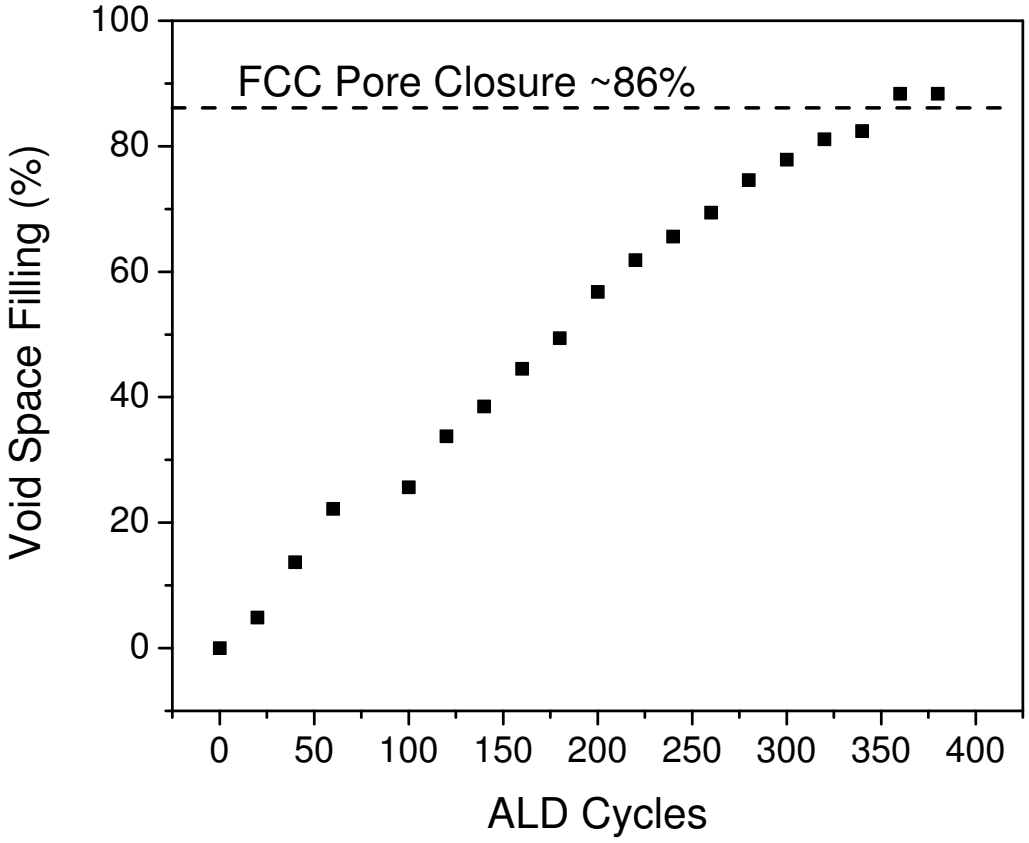

Figure 6.24 Calculated filling fractions from data reported in Figure 6.23, plotted as a function of ALD cycles. Maximum filling line is shown as dotted line.

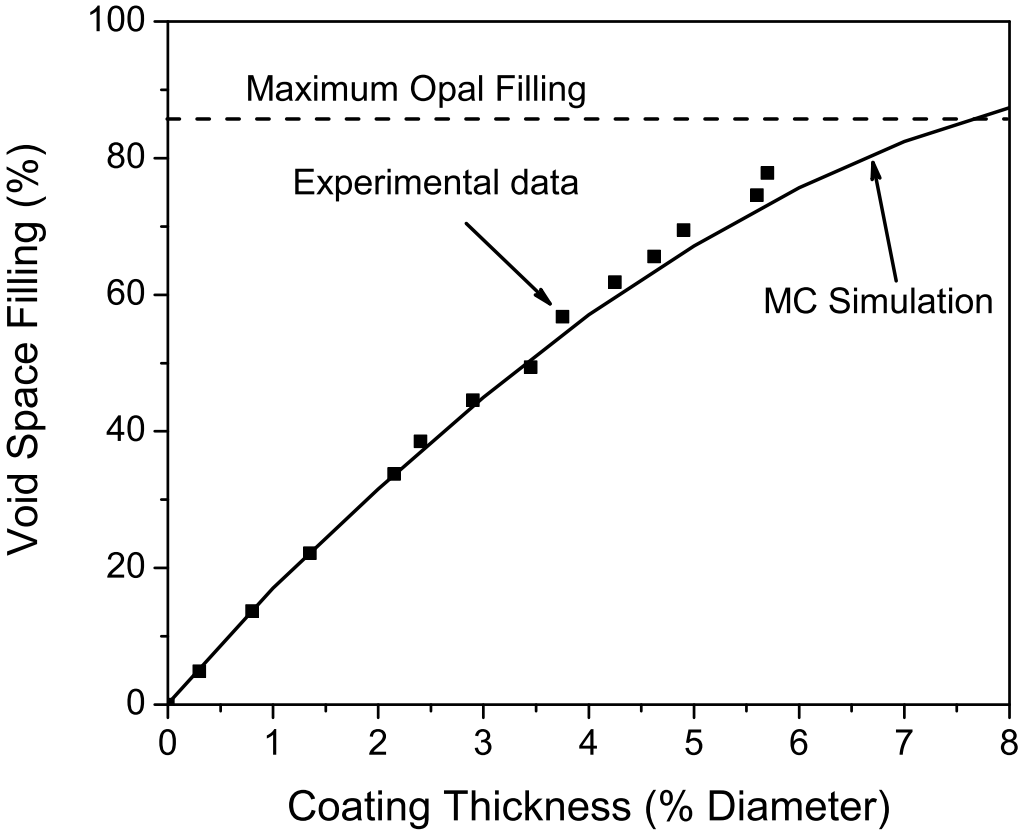

Figure 6.25 Void space filling as a function of coating thickness, calculated from comparison of data from 6.24 with calculated photonic band diagrams for shell opals.

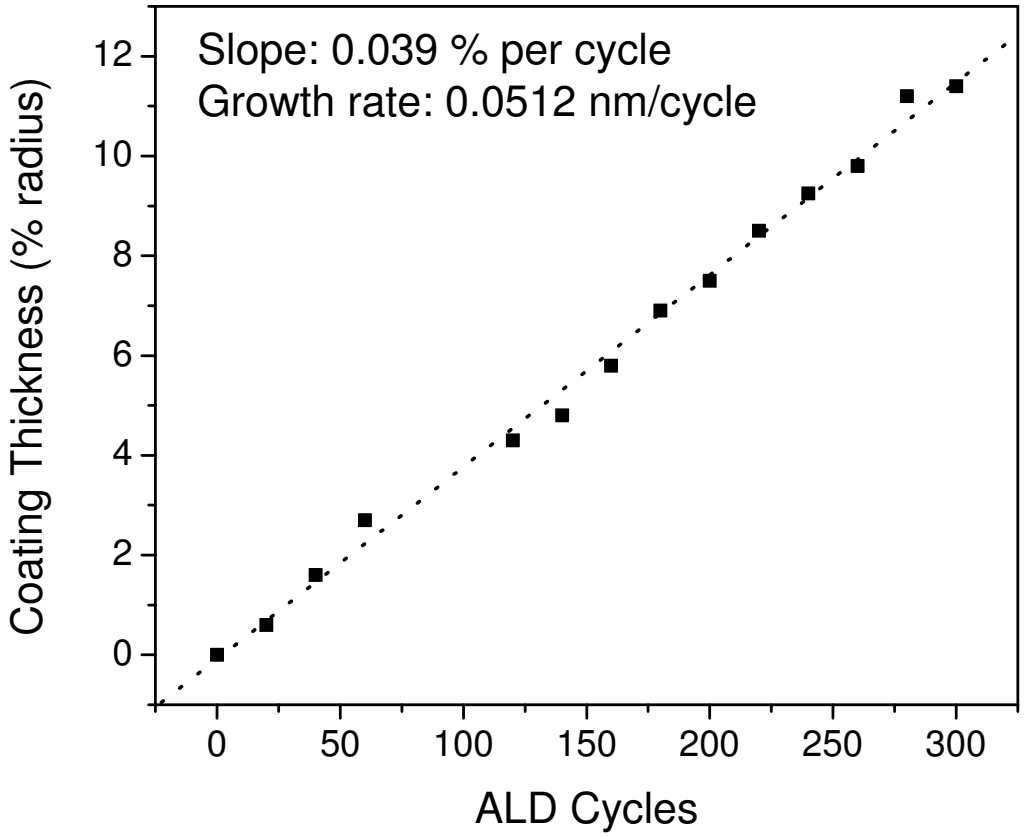

Figure 6.26 Coating thickness from Figure 6.25 plotted as a function of ALD cycles, with resulting growth rate calculation.

CHAPTER 7

LUMINESCENT COMPOSITE PHOTONIC CRYSTALS

This chapter details results of the final stage of the research described within this thesis. The work described takes the knowledge bases gained during the two different studies that were described in Chapters 5 and 6 on ZnS:Mn and TiO_2 and combines them for the fabrication of composite photonic crystals. Since these structures required infiltration of both ZnS:Mn and TiO_2, both the F120 and the custom built ALD reactors were used. The resulting structures were characterized using SEM, XRD, specular reflectivity, and PL, revealing successful fabrication of multilayered infiltrated and inverse opals that exhibit photonic band gaps as well as modification of the spontaneous emission using the high order photonic band gaps (flat bands). This work demonstrates that multi-layered infiltrations using atomic layer deposition (ALD) uniquely enable the formation of high quality inverse opals that combine both high index and luminescent materials. In this chapter, the results of formation of luminescent, layered ZnS/TiO2 inverse opals using ALD are presented. The results presented herein demonstrate yet again the enormous potential that ALD has for the fabrication of high performance photonic crystals.

7.1 Motivation

Very limited results have been reported that demonstrate the finesse needed in fabrication to effectively exploit the potential of opal-based photonic crystals. There have been numerous examples of successful fabrication of the inverse opal structure, exhibiting either full or partial infiltration of reasonably high index material, as discussed in section 2.6. These examples of partial infiltrations have typically not exhibited the dense, conformal films that would enable fabrication of structurally stable inverse opals that have characteristics such as optimized filling fractions or multiple layers. While they have been used for partial infiltrations, sol-gel and chemical bath techniques cannot offer conformal, dense coatings, or the nano-scale growth control required for formation of multi-layer opals. In addition, infiltration of opals and inverse opals with luminescent materials, such as laser dyes and nanoparticles has also been attempted, but neither technique can be used to precisely place or position the luminescent material, while maintaining a homogeneous inverse opal backbone.[27, 31, 89]

The precision of ALD uniquely makes infiltrations of different materials possible in any given sequence, and allows fabrication of new PC architectures including multi-layered composites. For example, one material can be used to create the necessary refractive index contrast, and another material can provide luminescence. Most luminescent materials do not offer sufficient index to realize a full photonic band gap. Thus, to obtain high index, luminescent materials as required for photonic crystal phosphors, a combination of two materials offers a practical route. For example: a ZnS:Mn (luminescent) and TiO_2 (high n) multi-layered structure could satisfy both

requirements. TiO_2 has a refractive index of 2.9 - 3.3 at wavelengths of 400 – 350 nm, respectively, for the anatase phase so it is anticipated that a full photonic band gap can be formed in the near UV for a TiO_2 inverse opal. It has been demonstrated that if a photonic band edge is located in a frequency range that experiences significant material absorption, the absorption can be enhanced by the low group velocity at the band edges.[20] Hence, incorporation of a small amount of ZnS:Mn in a TiO_2 inverse opal that exhibits a photonic band edge ~ 350 nm could increase the absorption of UV excitation at the ZnS:Mn band edge (~ 330 nm), thus improving the efficiency of the phosphor.

Even if a complete photonic band gap is not attained, the ability to form composite inverse opals allows a high level of tailorability of the photonic crystal properties. For example, the incorporation of TiO_2 with ZnS may flatten the high energy bands sufficiently to improve PL the efficiency by increasing absorption of excitation by the resulting decrease in the photon group velocity. In addition, instead of making use of full band gaps for suppression of emission, by proper design, the luminescence could be modified from a typical lambertian distribution to a focused or directional output by using partial band gaps. Another advantage of composite structures is that it enables tuning of the filling fraction, and hence the photonic bands, of a given structure by adding additional non-luminescent material. This maintains a constant amount of luminescent material within the photonic crystal, allowing better comparison between samples.

The growth methodology developed for formation of a composite PC requires the ability to infiltrate an opal or inverse opal (or other template) with a high degree of finesse. The process must allow great control of the infiltrated film thickness, and the

material must be dense and conformal. As demonstrated in Chapters 5 and 6, these strict requirements can be met by ALD.

7.2 Design Considerations

For a multi-layered structure, the dielectric approximation gives the effective refractive index as: $x_1.n_1(\lambda) + x_2.n_2(\lambda)$, where x_k and n_k are the volume fraction and refractive indices of component *k*. Thus, to support a full PBG in an inverse opal, $x_1.n_1(\lambda) + x_2.n_2(\lambda) \geq 2.8$. At 450 and 400 nm, the refractive indices of ZnS and TiO_2 (rutile phase) are, 2.46 and 2.52, and 3.0 and 3.2, respectively. Thus a ZnS/TiO_2 multi-layer inverse opal will support a full PBG if the ZnS content is less than 36% at 450 nm, or 59% at 400 nm. The rutile phase of TiO_2 has proven to be difficult to form, while the anatase phase forms quite easily, which has an index of 2.7 at 450 nm, and 2.9 at 400 nm. Thus, at 400 nm, it is possible to form a ZnS/anatase TiO_2 multi-layer with a full PBG if the ZnS content is less than 26%.

7.3 Details of Fabrication

In this study, opal templates were infiltrated with high index or luminescent material by partially filling the opal interstitial void space using ALD in a flow style hot-wall reactor. This first layer consisted of either ZnS:Mn or TiO_2, depending on the desired final structure. For two-layer inverse opals, the initial infiltration was TiO_2 as illustrated in Figure 7.1, while for three-layer inverse opals, the initial infiltration was ZnS:Mn, as illustrated in Figure 7.2. Next, the remaining interstitial volume was then

infiltrated with a second material, creating a two-layer infiltrated opal. As was done for TiO_2 infiltrations, the surface of the doubly infiltrated structure was removed using an ion mill, exposing the silica template. Removal of the silica spheres by etching with 2% HF resulted in formation of a stable two-layer inverse opal. For two-layer inverse opals with the ZnS:Mn layer as the first deposited layer, a third TiO_2 infiltration step was then used to backfill the original air sphere space, forming a non-close-packed, three-layer, luminescent inverse opal.

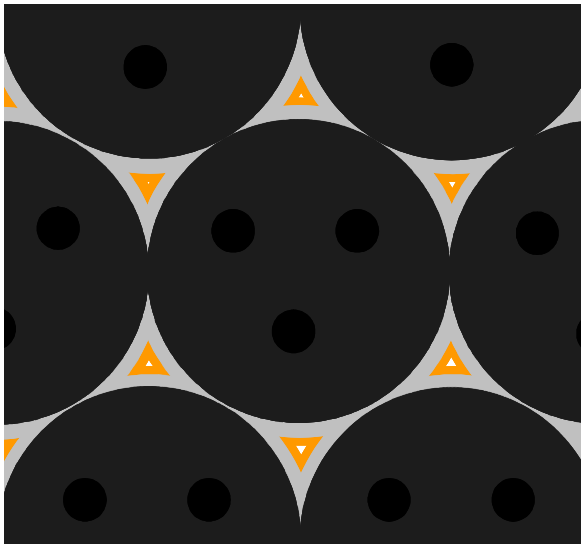

Figure 7.1 Diagram of ZnS:Mn/TiO_2 inverse opal. Grey layers are TiO_2 and orange layer is ZnS:Mn.

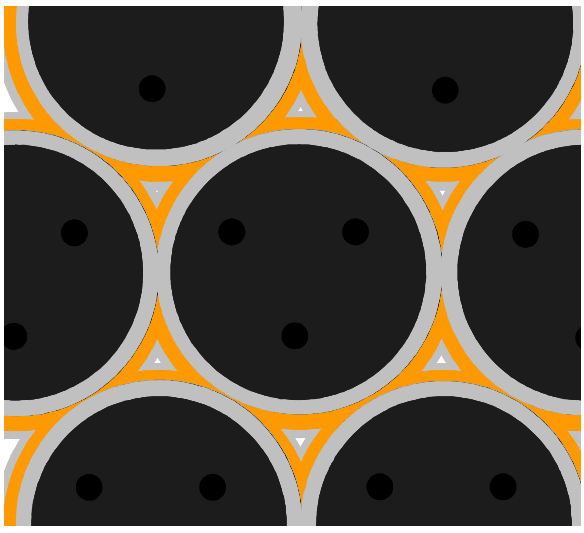

Figure 7.2 Diagram of TiO_2/ZnS:Mn/TiO_2 inverse opal. Grey layers are TiO_2 and orange layer is ZnS:Mn.

7.4 Results/Discussion

7.4.1 X-ray Diffraction

X-ray diffraction data was measured for the composite infiltration, to confirm the presence of both TiO_2 and ZnS:Mn in the structure. The anatase phase of TiO_2 and the wurtzite phase of ZnS were found, as shown in Figure 7.3. This figure shows the existence of peaks from both infiltrated materials. The peaks are labeled with "A" or "W", denoting anatase or wurtzite, respectively, and are indexed with the respective planes responsible for diffraction. The broad hump-like peak starting at $2\theta = 20°$ and extending to ~ $2\theta = 32°$ is characteristic of amorphous materials, and is therefore attributed to the silica spheres making up the infiltrated opal template.

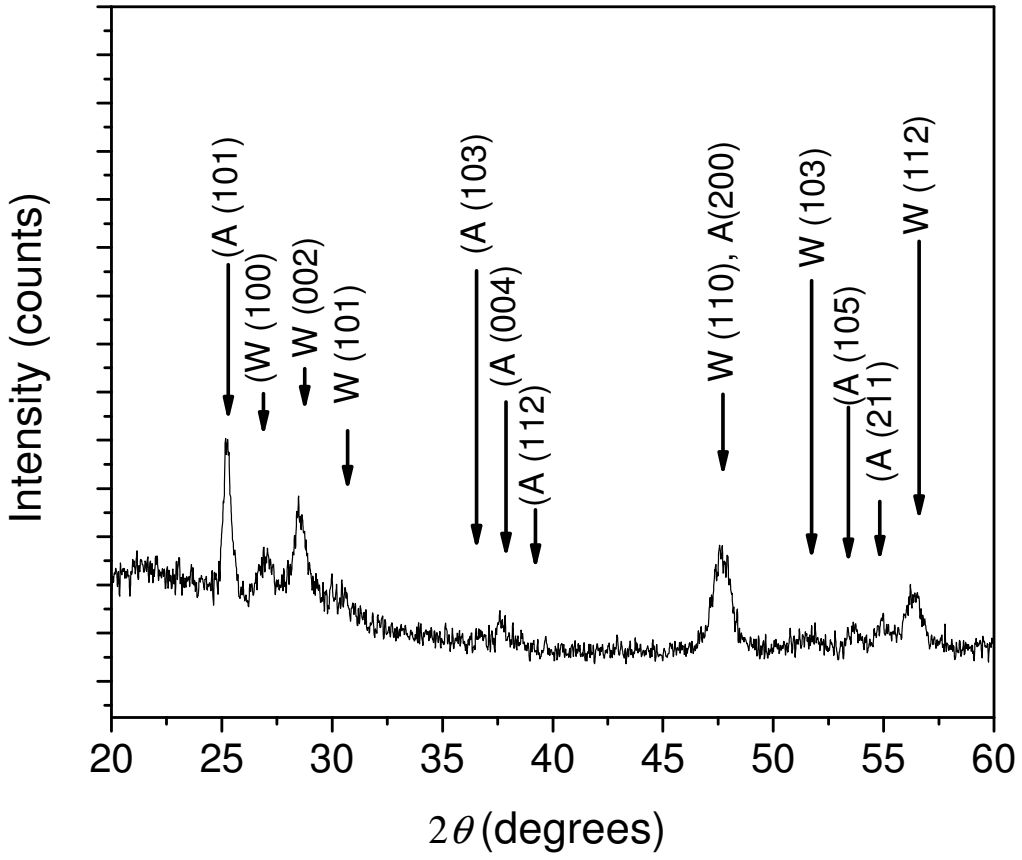

Figure 7.3 X-ray diffraction data for a ZnS + TiO_2 multi-layered infiltration of a silica opal. TiO_2 reflections are indicated by A(ijk), and ZnS:Mn by W(ijk).

7.4.2 Scanning Electron Microscopy

For structural characterizations, the resulting films were examined in a SEM. Figure 7.4 shows an ion-milled cross section of the (111) plane of a ZnS/TiO_2/Air inverse opal, clearly revealing the resulting periodic structure of high dielectric material and air spheres. The original silica sphere diameter for this sample was 330 nm, and both TiO_2 and ZnS:Mn layers were 10 nm thick. The maximum thickness of infiltrated material for this opal size is 25.6 nm, so as expected, there is still some air remaining in the original pore volume, as confirmed by the dark regions adjacent to the ZnS:Mn layer in the figure. Closer examination of the image reveals that there are clearly two distinct conformal layers that comprise the structure, with the TiO_2 layer being the first layer (closest to the "air sphere") and the second being the ZnS:Mn layer. The larger dark spots in the image on the surface of the air sphere region are the air holes resulting from the connectivity between the SiO_2 spheres formed after sintering (prior to infiltration). The inset portion of the figure is a higher magnification image of the multi-layer region formed at the interstice between the air spheres. In this image, the darker material is TiO_2 and the lighter material is ZnS:Mn, again with the darkest region being air due to intentional incomplete infiltration.

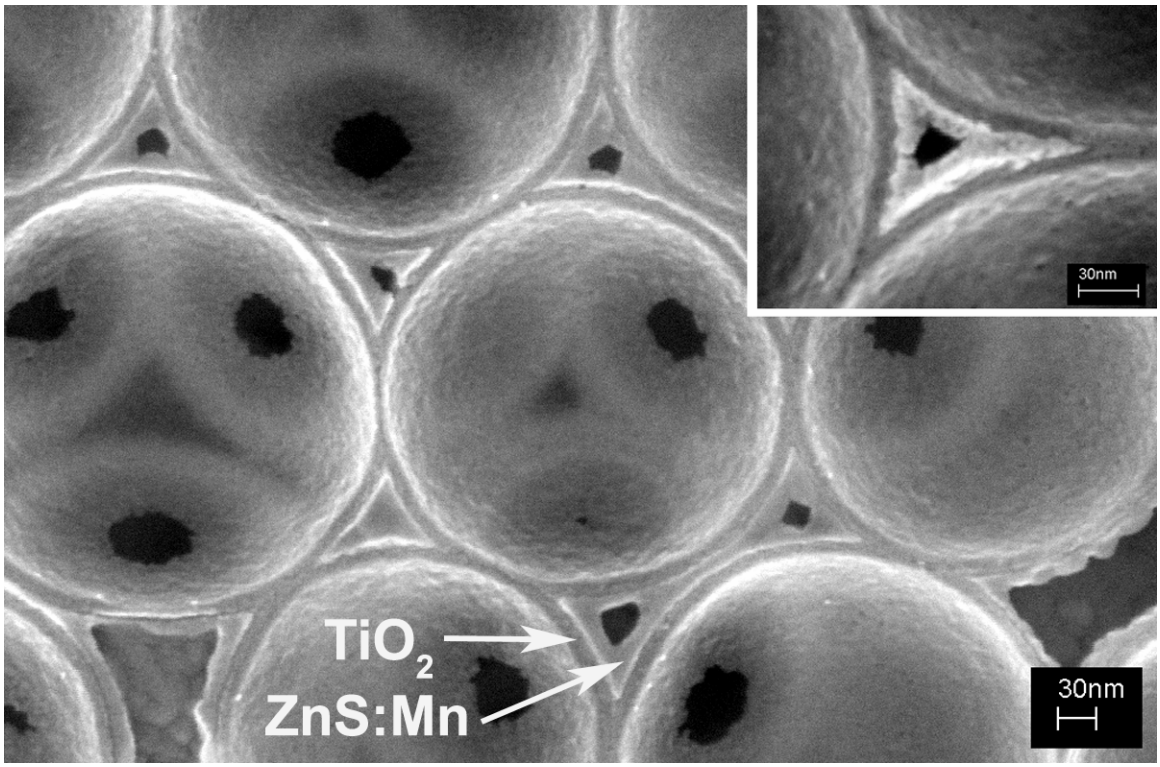

Figure 7.4 330 nm sized ZnS (10 nm)/TiO2 (10 nm) inverse opal photonic crystal, with detail of multi-layer region (inset).

Figure 7.5 shows a similar SEM cross section of a TiO_2/ZnS:Mn/TiO_2/air (24/10/10 nm) inverse opal. The original sphere diameter for this structure was 433 nm. Inset is an image of the three-layer inverse structure prior to the final ion milling step. The surface was ion milled after deposition of layer 2 to allow for SiO_2 sphere removal, as shown by the large dark hole in the inset image. The three layers are labeled in the image, with the TiO_2 layers being the gray regions, and the ZnS:Mn layer being the lighter region sandwiched between them. Clearly the layers are highly conformal and spatially distinct, and a multi-layer inverse opal has been successfully formed. It is important to also notice that the air sphere connectivity points have reduced in size when compared to the 2-layer inverse opal due to the fact that the 3rd layer is grown on the surface of the air sphere, backfilling the inverse opal.

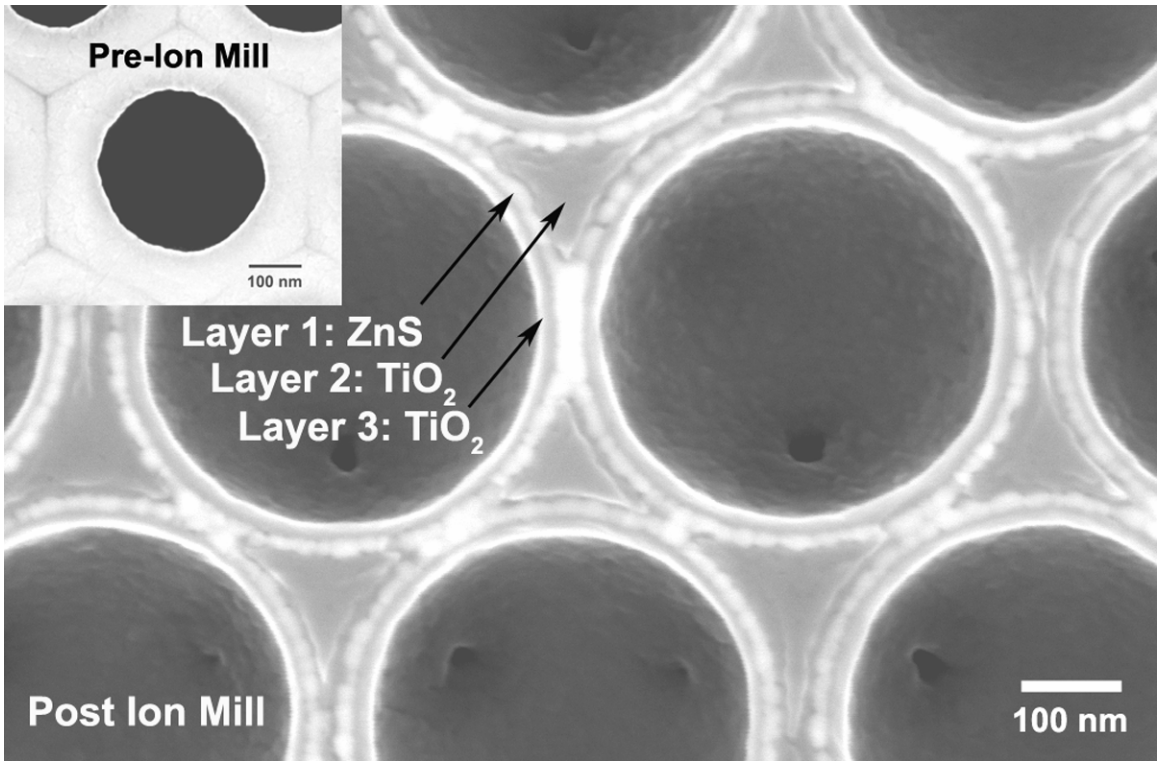

Figure 7.5 Ion milled cross section of the (111) plane of a 433 nm sphere diameter TiO_2 /ZnS:Mn/TiO_2/air (24/10/10 nm) layered inverse opal photonic crystal. Inset is of three-layer inverse structure after backfilling, but prior to ion milling step.

7.4.3 Resulting Photonic Band Structure: Specular Reflectivity

During fabrication of a 2 or 3-layer multi-layer photonic crystal, as in the case of single component infiltrations, each processing step can again be followed by examining the shift of the Γ-L PPBG peak found in specular reflectance as a function of wavelength. Figure 7.6 is a plot of the reflection spectra measured at 15° from normal incidence during the formation of a three layer inverse opal using a 330 nm SiO_2 opal template, prior to backfilling with TiO_2 to form the 3rd layer. For the sintered opal, the peak is at 714 nm. The peak then shifts to 822 nm and widens after infiltration with 10 nm of ZnS:Mn, and shifts to 866 nm and further widens after the remaining pore volume is filled with TiO_2. After removing the SiO_2 spheres, the peak shifts to 721 nm, consistent with the resulting decrease in average refractive index, and again widens. The broad reflectivity peaks for the 2-layer inverse opal (curve d) at ~400 nm are attributed to Γ-L PPBGs that form between the 5th and 6th and the 8th and 9th bands in an inverse opal, as calculated using the plane wave expansion method [84].

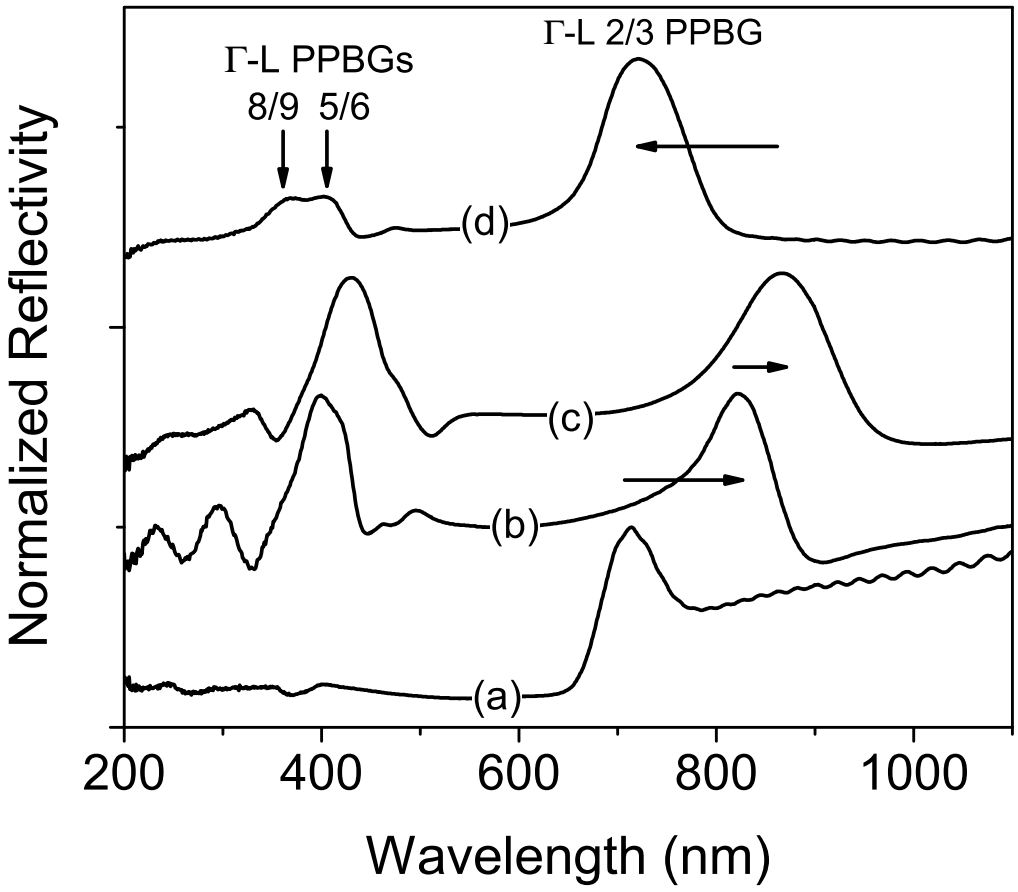

Figure 7.6 Specular reflectivity at 15º for (a) sintered, (b)ZnS:Mn infiltrated, (c) ZnS:Mn/TiO_2 infiltrated, and (d)ZnS:Mn/TiO_2 inverse 330 nm opal.

Figure 7.7 summarizes the specular reflectivity changes that occur during the processing sequence for a 433 nm three-layer composite inverse opal, with a final TiO_2 backfill thickness of 10 nm. The Γ-L peak is at 930 nm for the bare opal, and shifts to just beyond 1100 nm after infiltration with 10 nm of ZnS:Mn. The same peak shift after infiltration with 24 nm of TiO_2 could not be tracked, because it is beyond the range of the spectrometer, but the flat band peak clearly becomes stronger and wider, with a peak at 580 nm. After etching with HF, the primary peak returns to a measurable wavelength, 987 nm. The high order peak does not shift much, but does develop into two peaks, one at 576, and one at 620 nm. Backfilling the inverse 2-layer structure with 10 nm of TiO_2 yielded more changes in reflectivity: the primary peak again shifts to beyond the measurement range, and higher order peaks develop at 585 nm and 725 nm.

Figure 7.8 details the changes in specular reflectance found during progressive backfilling of a 2-layer inverse opal with TiO_2, forming the desired 3-layer structure. The 2-layer inverse opal was formed using a 433 nm SiO_2 template, in the same manner as the 330 nm sample detailed in Figure 7.6 (10 nm ZnS:Mn + remainder TiO_2), but the final layer was deposited in 1 nm steps, yielding a thinner final layer thickness of 5 nm. This sample was fabricated to show the PBG tunability that ALD allows, and is the sample that was used for photoluminescence measurements presented in the next section. The Γ-L 2/3 PPBG peak starts at 996 nm, for the 2-layer structure, shifting to higher wavelength after each TiO_2 infiltration; after 5 nm of TiO_2 backfilling, or 100 ALD cycles, the peak shifts to 1069 nm. The higher order PPBG peaks also shift to higher wavelengths, starting at ~ 585 and 616 nm, and ending at ~ 623 and 660 nm, for the 8/9 and 5/6 gaps,

respectively. This particular sample was fabricated because the high order band gap position overlaps the emission peak from the ZnS:Mn phosphor layer.

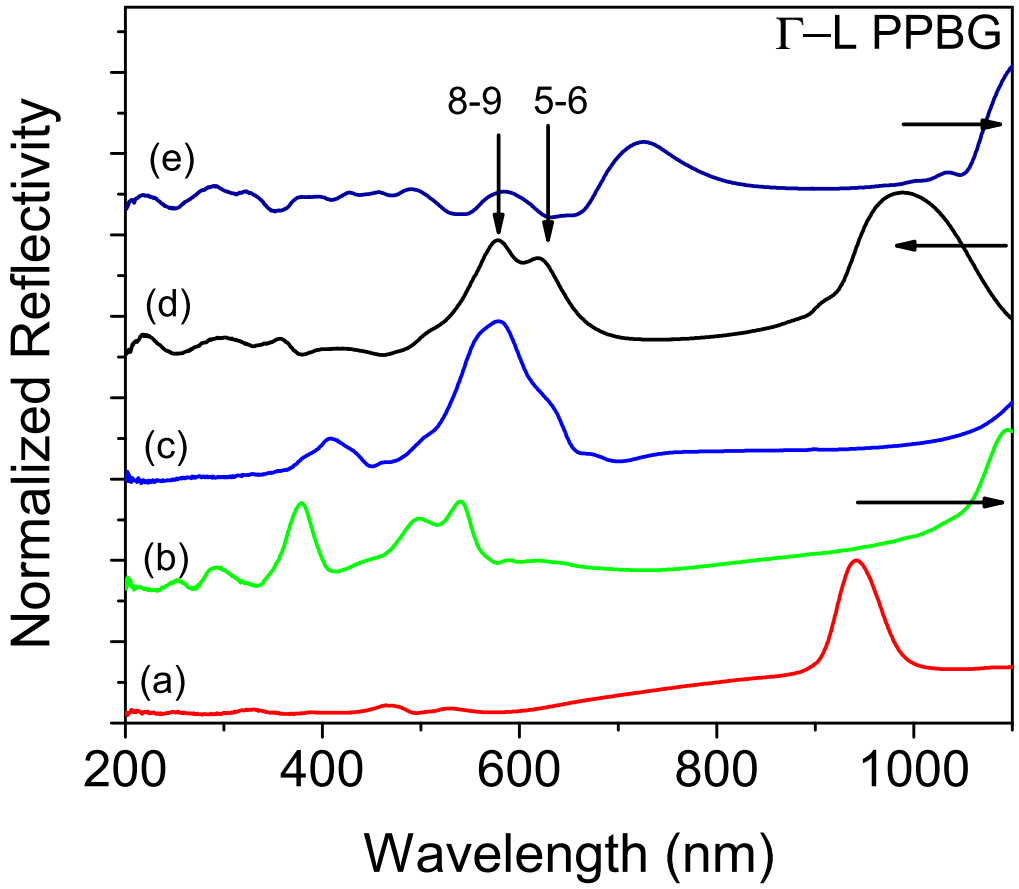

Figure 7.7 Summary of specular reflectivity measured during fabrication of 433 nm 24 nm TiO_2/10 nm ZnS:Mn/ 10 nm TiO_2 inverse opal photonic crystal. (a) sintered, (b)ZnS:Mn infiltrated, (c) TiO_2/ZnS:Mn infiltrated (d) TiO_2/ZnS:Mn inverse, and (e) TiO_2/ZnS:Mn/TiO_2 inverse opals.

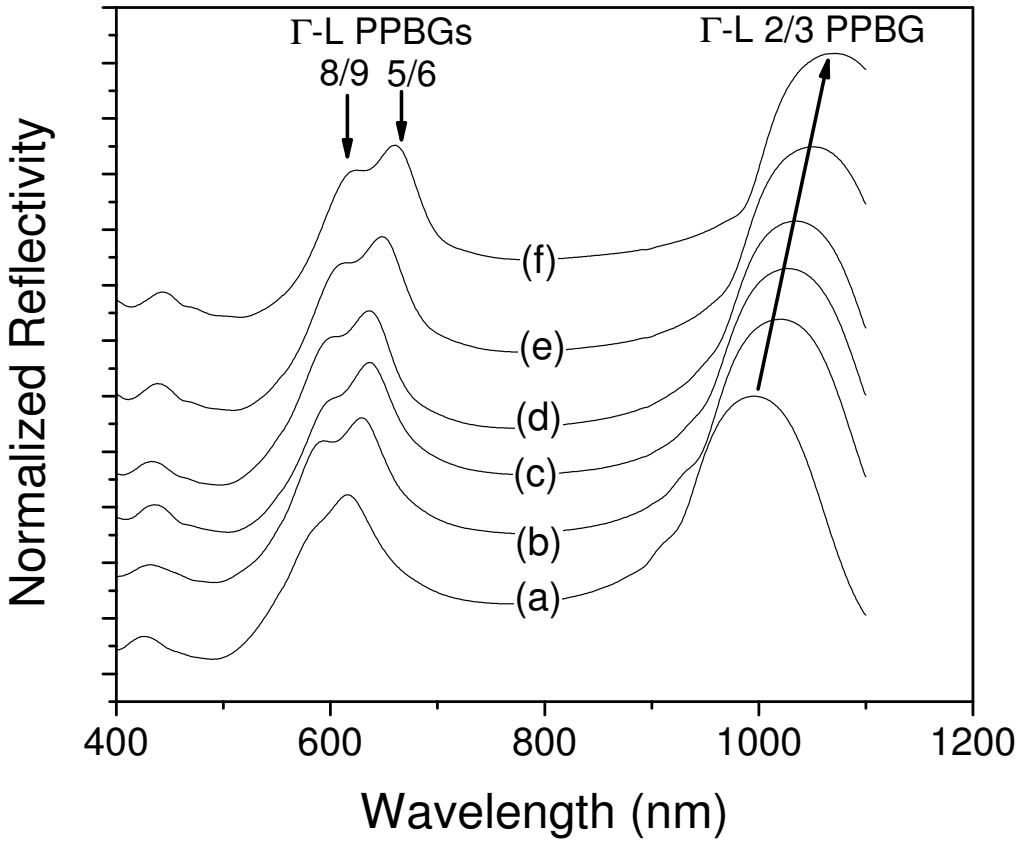

Figure 7.8 Specular reflectance at 15º for (a) ZnS:Mn/TiO_2 433 nm inverse opal, and resulting TiO_2/ZnS:Mn/TiO_2 inverse opal after backfilling with (b) 20, (c) 40, (d) 60, (e) 80, (f) 100 total ALD cycles (~0.5 Å/cycle). The initial ZnS:Mn layer was 10 nm thick, and the final backfilled thickness is ~5 nm.

The Γ-L portion of the photonic band diagram for the two-layer multilayered opal consisting of a 24 nm TiO_2 layer and a 10 nm ZnS:Mn layer was calculated using the effective index approximation for the refractive index used in the simulation, instead of creating a dielectric function with distinct layers of differing refractive index. This band diagram is shown in figure 7.9, as compared to the measured reflectivity data. Two wide and one narrow PPBGs have developed in the high energy portion of the band diagram, between the 5^{th} and 6^{th}, 8^{th} and 9^{th}, and the 10^{th} and 11^{th} bands. The peak in the reflectivity matches the position of the gap between the 5^{th} and 6^{th} bands. While there is no other distinct peak in the reflectivity, the width of the peak spans the width of the three band gaps. The PPBG between the 2^{nd} and 3^{rd} bands is located at the long wavelength region on the diagram, and is clearly wide, agreeing with the reflectivity peak in both position and width.

The same portion of the band diagram was calculated in the same manner for the same structure, after backfilling with 5 nm of TiO_2, and is shown in figure 7.10, again compared with the measured reflectivity data. The primary peak has shifted partially beyond the measurement range, agreeing with the band diagram. The long wavelength band edge cannot be measured from the reflectivity data, but the peak position agrees with the band diagram. The band diagram indicates that by backfilling the inverse opal slightly, the same band gaps are present as before, but the 10^{th} to 11^{th} gap has opened wider, and another gap has opened between the 12^{th} and 13^{th} bands. The high energy reflectivity peak again spans the wavelength range of these 4 band gaps.

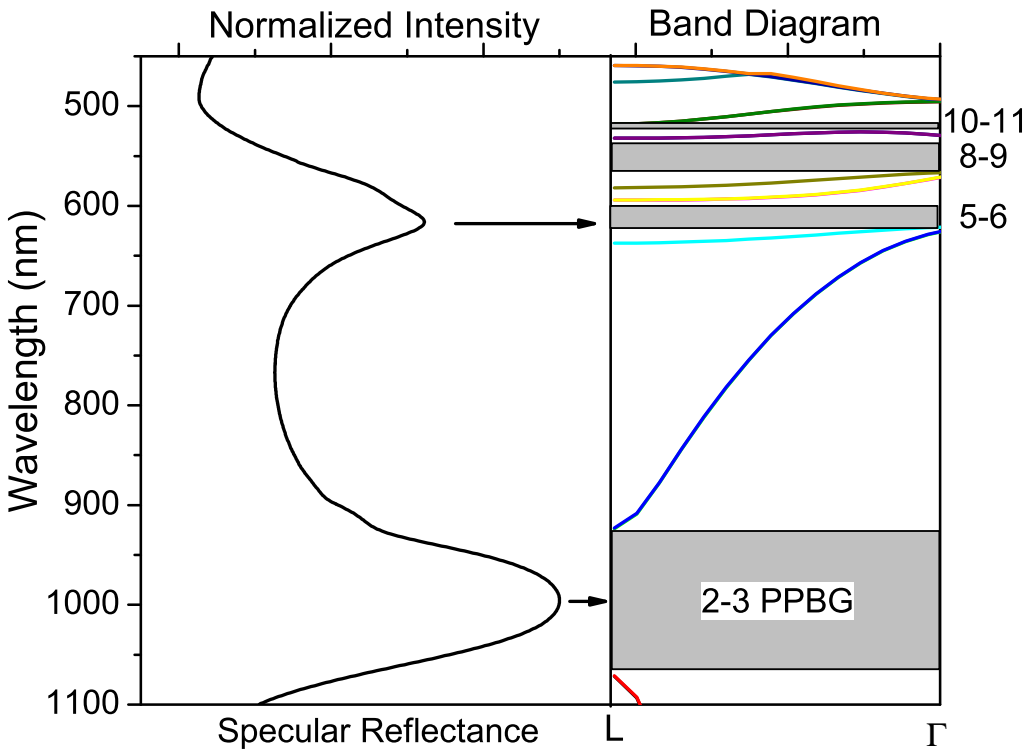

Figure 7.9 Specular reflectivity compared with the photonic band diagram for a two-layer 433 nm inverse opal. (24 nm TiO_2/10 nm ZnS)

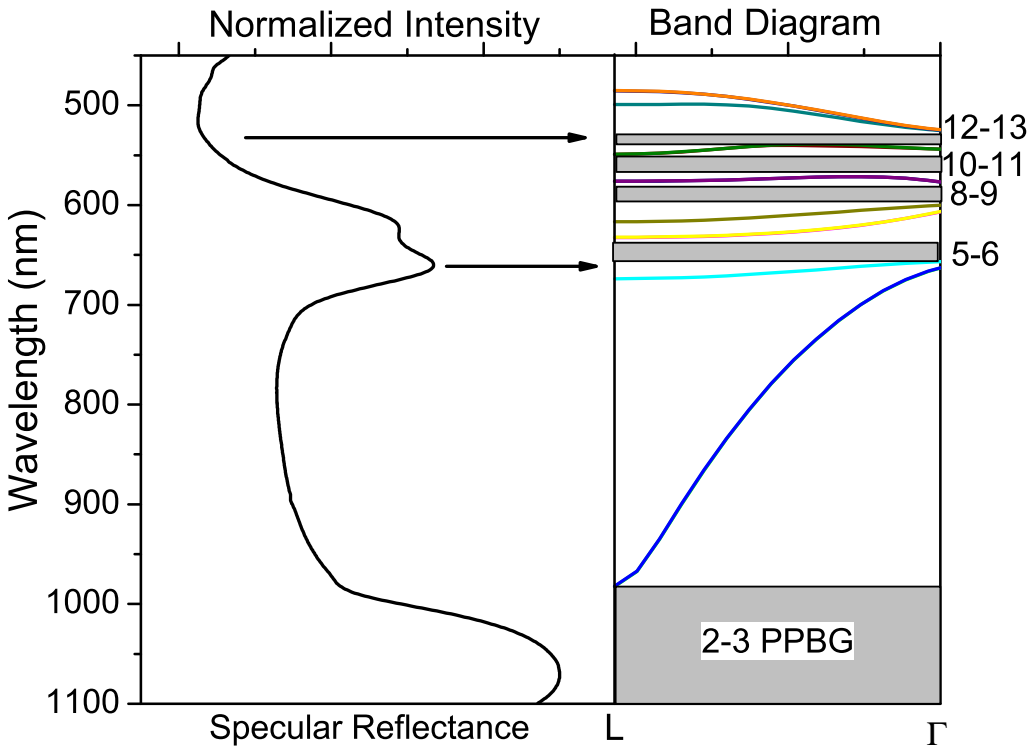

Figure 7.10 Specular reflectivity for 24 nm/ 10 nm ZnS:Mn/ 5 nm 433 nm inverse opal, compared with Γ-L portion of the photonic band diagram.

7.4.4 Spontaneous Emission Modification: Photoluminescence

Photoluminescence was next measured with 45º incident 337 nm pulsed UV excitation for both 10 nm and 20 nm ZnS:Mn layer samples. Figure 7.11 shows the PL collected normal to the (111) surface after each backfilling step of the fabrication of a 433 nm 3-layer inverse opal with a 20 nm ZnS:Mn layer, as well as the reflectivity measured at 15º for the same sample. The reflectivity peaks measured before TiO_2 backfilling indicate that the positions of the PPBGs are at 590 nm for the gap between the 8^{th} and 9^{th} bands, and 630 nm for the gap between the 5^{th} and 6^{th} bands. These peaks shift with each ALD backfilling sequence, ultimately moving to 645 and 687 nm after 5 nm of deposition. Emission peaks were observed at both 460 nm and 585 nm, corresponding to Cl^- defect donor-acceptor and Mn^{2+} luminescent center emission, respectively. The 585 nm emission peak is nearly coincident with the PPBG at 590 nm found in the TiO_2/ZnS:Mn inverse opal. The curves were therefore normalized to the 460 nm peak, which reveals a systematic increase in PL relative intensity of 108% for the 585 nm peak as the photonic band gaps shift to higher wavelength with increasing ALD backfilling.

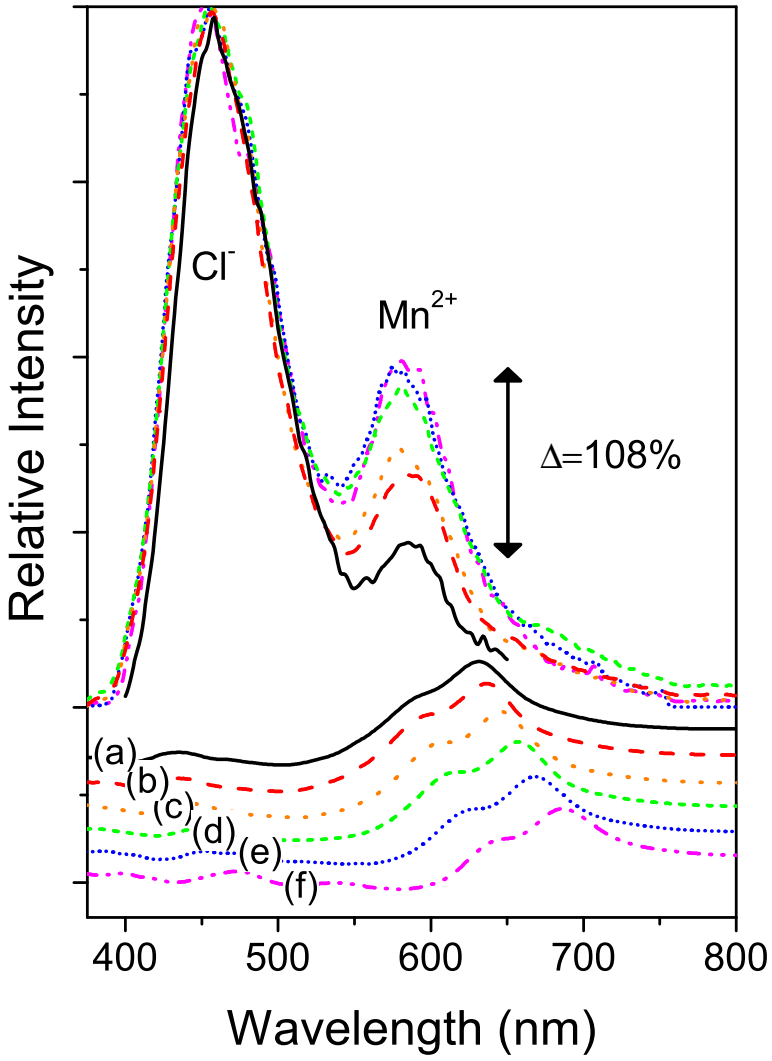

Figure 7.11 Photoluminescence (upper curves) compared with specular reflectivity (lower curves) as measured for (a, black) TiO_2 (14 nm)/ ZnS:Mn (20 nm)/air 433 nm inverse opal and after backfilling with (b, red)) 1 (c, orange) 2, (d, green) 3, (e, blue) 4, and (f, magenta) 5 nm of TiO_2.

CHAPTER 8

CONCLUSIONS

Photonic Crystals are exciting new prospects for the future of optoelectronics. They have application in areas ranging from biological sensors to flat panel displays. The groundbreaking theoretical work by Yablonovitch and John has led to numerous successes in the laboratory. The challenge to fabricate three-dimensional Photonic Crystals for visible wavelengths is a difficult but attainable goal, and it has been demonstrated that ALD has enormous potential for making these structures. In this thesis, the fabrication methods for forming inverse opals using the infiltration of self assembled silica thin films was described. Opal based PC's were infiltrated with ZnS:Mn and TiO_2, with successful realization of filling fractions approaching theoretical maximum values. Photoluminescence data shows that the infiltrated opals are of high quality, and modification of emission has been demonstrated. Finally, ZnS:Mn/TiO_2 multilayer photonic crystals were successfully formed, again exhibiting modification of spontaneous emission by the photonic band structure. Fabricated structures were characterized using SEM, FIB, specular reflectivity and transmission, x-ray diffraction, and photoluminescence.

ZnS:Mn infiltrated and inverse opals were successfully formed by ALD infiltration of silica opals using $ZnCL_2$ and H_2S, at 500° C, in a commercially available reactor. Filling fractions approaching the maximum amount for conformal growth were achieved (~ 86%), for opal sizes ranging from 160 to 460 nm, and the resulting opals

exhibit PL that has intensity comparable to ZnS:Mn thin films. The evolution of the photonic band structure was studied as a function of infiltration amount, and after etching to form the inverse opal. Specular reflectivity indicated the existence of a peak that corresponds to the PPBG formed between the 2nd and 3rd photonic bands in the Γ-L direction, as well as numerous shorter wavelength peaks that correspond to either flat bands for the infiltrated opal, or PPBGs for the inverse opal. Comparison of this data with the calculated photonic band diagrams reveals good agreement between the two, for silica opals, infiltrated opals, and inverse opals.

The low temperature fabrication of TiO_2 inverse "shell" opals using ALD was reported. After optimizing the pulse and purge lengths to achieve full penetration of the 10 μm opal film, self-assembled 200 - 440 nm-sized silica opals were infiltrated using conventional precursors at 100° C, annealed for 2 hrs at 400° C, and inverted using HF. The shifts in the Γ-L PBG position and width were confirmed by specular reflectance and transmission, revealing behavior consistent with photonic band calculations. The peak positions indicate that filling terminated at ~ 88 % of the pore volume, as estimated from the modified Bragg equation, supporting the theoretical prediction that maximum filling for a "shell" opal is 86%. SEM and AFM analysis reveals ultra-smooth (RMS roughness of < 0.5 nm), highly conformal anatase films as a result of the combination of low temperature deposition with a short heat treatment. In addition, precise infiltration control (< 1 nm) was achieved with this technique, making the fine-tuning of photonic crystal properties a reality. The success of this work shows that precisely controlling the placement of dielectric materials is possible using ALD, enabling the fabrication of many of the "optimized" structures that have been predicted to have the best optical properties.

Precise, controllable, tuning of photonic crystal optical properties using atomic layer deposition of ZnS:Mn and TiO_2 was also reported. By combining ALD of these two materials independent control of the luminescent and PBG properties of multi-layer 3D inverse opal PC's was achieved. Suppression of photoluminescence by superpositioning the PPBGs formed by the 8^{th} and 9^{th} bands and the 5^{th} and 6^{th} bands with the 585 nm Mn^{2+} emission peak was demonstrated. Backfilling a 2-layer inverse opal with a thin layer of high index material was also used to fine-tune the optical properties, allowing the PPBGs to be shifted off of the emission peak, yielding a 108% increase in PL relative intensity. The data presented demonstrates that multi-layered infiltrations using ALD uniquely enable the formation of high quality inverse opals that combine both high index and luminescent materials.

The successful realization of high-quality infiltrated, inverse, and multilayered opals using ALD infiltration of silica opals with ZnS:Mn and TiO_2 reveals the potential that this technique has for the future of photonic crystal fabrication. ALD can be used for fabrication of PCs based on the opal architecture, but it also has great potential for integration with other fabrication methods such as holographic lithography, traditional lithographically produced 2D and 3D structures, as well as e-beam derived PCs. Its conformal nature, precision, flexibility, and low temperature capability make it an indispensable tool for the future of PC fabrication.

APPENDIX A

CALCULATION OF INFILTRATION FILLING FRACTIONS

Bragg's law for optical diffraction from (111) planes is,

$$\lambda = 2d0.816\sqrt{\varepsilon_{avg.} - Sin^2\theta}$$

where λ is the wavelength of diffraction, d is the average size of the spheres comprising the opal, ε_{avg} is the effective dielectric constant of the film, and θ is the angle of incidence (normal incidence to the (111) planes is 0°). For an opal with FCC crystal structure (26% void volume), the effective dielectric constant is:

$$\varepsilon_{avg} = \varepsilon_{Silica}0.74 + (0.26)\varepsilon_{air}$$

Since ε_{avg} is known for an opal, measurement of λ allows calculation of *d*, the average sphere diameter of the opal film. If the opal is then infiltrated with a material of dielectric constant ε_{inf}, ε_{avg} becomes:

$$\varepsilon_{avg} = \varepsilon_{Silica}0.74 + (0.26 - f)\varepsilon_{air} + f\varepsilon_{\inf}$$

The terms in the above equation $(0.26 - f)\,\varepsilon_{air} + f\varepsilon_{inf}$, are the contribution to the average dielectric constant by the infiltrated and uninfiltrated pore volume. The term, $f\varepsilon_{inf}$, is the

contribution to the average dielectric constant by the resulting volume fraction of infiltrated material. The term $(0.26 - f)\,\varepsilon_{air}$ is the contribution of the air within the pore volume, which consists of both any internal porosity of the infiltrated material and the uninfiltrated portion of the pore volume. The maximum amount possible to infiltrate an FCC structure would be the entire pore volume, or 26% of the entire volume. Since *d* was previously measured, the resulting $\lambda_{infiltrated}$ allows calculation of the change in ε_{avg}. Rewriting the above equation yields the filling fraction:

$$f = \frac{\varepsilon_{avg} - \varepsilon_{silica}(0.74)) - 0.26}{\varepsilon_{\inf} - 1}$$

For FCC structures, since the available pore space is 26% the filling fraction of the available pore volume after infiltration is:

$$filling\% = \frac{f}{0.26} \cdot 100\%$$

REFERENCES

[1] Witzens, J., M. Loncar, and A. Scherer, *IEEE Journal of Selected Topics in Quantum Electronics*, **2002**. *8,* 1246.

[2] Yablonovitch, E., *Phys. Rev. Lett*, **1987**. *58,* 2059.

[3] Dowling, J.P., M. Scalora, M.J. Bloemer, and C.M. Bowden, *Journal of Applied Physics*, **1994**. *75,* 1896.

[4] John, S. and T. Quang, *Physical Review A (Atomic, Molecular, and Optical Physics)*, **1994**. *50,* 1764.

[5] Birks, T.A., W.J. Wadsworth, and P.S.J. Russell.1 pp. in *Conference Digest. 2000 Conference on Lasers and Electro-Optics Europe, 10-15 Sept. 2000*. 2000. Nice, France: IEEE.

[6] www.crystal-fibre.com

[7] Park, S.H., D. Qin, and Y. Xia, *Adv. Mat.*, **1998**. *10,* 1028.

[8] Stober, W., A. Fink, and E. Bohn, *J. Coll. Int. Sci.*, **1968**. *26,* 62.

[9] John, S. and K. Busch, *Journal of Lightwave Technology*, **1999**. *17,* 1931.

[10] John, S., *Phys. Rev. Lett*, **1987**. *58,* 2486.

[11] Russell, P.S.J., T.A. Birks, J.C. Knight, R.F. Cregan, B.J. Mangan, and J.-P. de Sandro, *Japanese Journal of Applied Physics, Supplement International Workshop on Structure and Functional Optical Properties of Silica and Silica-Related Glasses, 10-11 July 1997*, **1998**. 45.

[12] Sakoda, K., *Optical Properties of Photonic Crystals*. 1 ed. Springer-Verlag, New York **2001**.

[13] Yeh, P., *Journal of the Optical Society of America*, **1979**. *69,* 742.

[14] John, S. and T. Quang, *Phys. Rev. Lett*, **1997**. *78,* 1888.

[15] John, S. and T. Quang, *Phys. Rev. Lett*, **1995**. *74,* 3419.

[16] Lin, S.Y., J. Moreno, and J.G. Fleming, *App. Phys. Lett.*, **2003**. *83,* 380.

[17] John, S. and T. Quang, *Phys. Rev. Lett*, **1996**. *76,* 2484.

[18] Mekis, A., J.C. Chen, I. Kurland, S. Fan, P.R. Villeneuve, and J.D. Joannopoulos, *Phys. Rev. Lett*, **1996**. *77,* 3787.

[19] Villeneuve, P.R., S. Fan, J.D. Joannopoulos, K.-Y. Lim, G.S. Petrich, L.A. Kolodziejski, and R. Reif, *App. Phys. Lett.*, **1995**. *67,* 167.

[20] Lin, S.Y., J.G. Fleming, Z.Y. Li, I. El-Kady, R. Biswas, and K.M. Ho, *Journal of the Optical Society of America B (Optical Physics)*, **2003**. *20,* 1538.

[21] Yariv, A., Yeh, P., *Optical Waves in Crystals*. Wiley, New York **1984**.

[22] Yee, K., *IEEE Transactions on Antennas and Propagation*, **1966**. 302.

[23] Neff, C.W., PWE-derived photonic band diagrams were calculated with his assistance, using MIT's Photonic Bands package.,

[24] Gaillot, D., Yamashita, T., FDTD-derived photonic band diagrams were calculated with the assistance of these two group members, and code they developed.,

[25] Purcell, E.M., *Physical Review*, **1946**. *69,* 681.

[26] Blanco, A., H. Miguez, F. Meseguer, C. Lopez, F. Lopez-Tejeira, and J. Sanchez-Dehesa, *App. Phys. Lett.*, **2001**. *78,* 3181.

[27] Romanov, S.G., A.V. Fokin, and R.M. De La Rue, *App. Phys. Lett.*, **1999**. *74,* 1821.

[28] Meier, M., A. Dodabalapur, J.A. Rogers, R.E. Slusher, A. Mekis, A. Timko, C.A. Murray, R. Ruel, and O. Nalamasu, *Journal of Applied Physics*, **1999**. *86,* 3502.

[29] Megens, M., J.E.G.J. Wijnhoven, A. Lagendijk, and W.L. Vos, *Journal of the Optical Society of America B (Optical Physics)*, *16,* 1403.

[30] King, J.S., C.W. Neff, S. Blomquist, E. Forsythe, D. Morton, and C.J. Summers, *Phys. Stat. Sol. (b)*, **2004**. *241,* 763.

[31] Megens, M., J.E.G.J. Wijnhoven, A. Lagendijk, and W.L. Vos, *Physical Review A. Atomic, Molecular, and Optical Physics*, **1999**. *59,* 4727.

[32] Yablonovitch, E., T.J. Gmitter, and K.M. Leung, *Phys. Rev. Lett*, **1991**. *67,* 2295.

[33] Chelnokov, A., K. Wang, S. Rowson, P. Garoche, and J.-M. Lourtioz, *App. Phys. Lett.*, **2000**. *77,* 2943.

[34] Ozbay, E., E. Michel, G. Tuttle, R. Biswas, M. Sigalas, and K.-M. Ho, *App. Phys. Lett.*, **1994**. *64,* 2059.

[35] Lin, S.Y., J.G. Fleming, D.L. Hetherington, B.K. Smith, R. Biswas, K.M. Ho, M.M. Sigalas, W. Zubrzycki, S.R. Kurtz, and J. Bur, *Nature*, **1998**. *394,* 251.

[36] Campbell, M., D.N. Sharp, M.T. Harrison, R.G. Denning, and A.J. Turberfield, *Nature*, **2000**. *404,* 53.

[37] Lin, S.-Y. www.sandia.gov

[38] Sozuer, H.S., J.W. Haus, and R. Inguva, *Physical Review B (Condensed Matter)*, **1992**. *45,* 13962.

[39] Blanco, A., E. Chomski, S. Grabtchak, M. Ibisate, S. John, S.W. Leonard, C. Lopez, F. Meseguer, H. Miguez, J.P. Mondla, G.A. Ozin, O. Toader, and H.M. van Driel, *Nature*, **2000**. *405,* 437.

[40] Wijnhoven, J.E.G.J. and W.L. Vos, *Science*, **1998**. *281,* 802.

[41] Wijnhoven, J.E.G.J., L. Bechger, and W.L. Vos, *Chemistry of Materials*, **2001**. *13,* 4486.

[42] Soten, I., H. Miguez, S.M. Yang, S. Petrov, N. Coombs, N. Tetreault, N. Matsuura, H.E. Ruda, and G.A. Ozin, *Adv. Func. Mat.*, **2002**. *12,* 71.

[43] Kim, B.G., K.S. Parikh, G. Ussery, A. Zakhidov, R.H. Baughman, E. Yablonobitch, and B.S. Dunn, *App. Phys. Lett.*, **2002**. *81,* 4440.

[44] Li, B., J. Zhou, L. Li, X.J. Wang, X.H. Liu, and J. Zi, *App. Phys. Lett.*, **2003**. *83,* 4704.

[45] Astratov, V.N., A.M. Adawi, M.S. Skolnick, V.K. Tikhomirov, V. Lyubin, D.G. Lidzey, M. Ariu, and A.L. Reynolds, *App. Phys. Lett.*, **2001**. *78,* 4094.

[46] Golubev, V.G., D.A. Kurdyukov, A.B. Pevtsov, A.V. Sel'kin, E.B. Shadrin, A.V. Il'inskii, and R. Boeyink, *Fizika i Tekhnika Poluprovodnikov*, **2002**. *36,* 1122.

[47] Scott, R.W.J., S.M. Yang, G. Chabanis, N. Coombs, D.E. Williams, and G.A. Ozin, *Adv. Mat.*, **2001**. *13,* 1468.

[48] Zakhidov, A.A., R.H. Baughman, Z. Iqbal, C. Cui, I. Khayrullin, S.O. Dantas, J. Marti, and V.G. Ralchenko, *Science*, **1998**. *282,* 897.

[49] Romanov, S.G., H.M. Yates, M.E. Pemble, and R.M. De La Rue, *J. Phys: Cond. Matt.*, **2000**. *12,* 8221.

[50] Yates, H.M., W.R. Flavell, M.E. Pemble, N.P. Johnson, S.G. Romanov, and C.M. Sotomayor-Torres, *J. Cryst. Growth*, **1997**. *170,* 611.

[51] Romanov, S.G., N.P. Johnson, A.V. Fokin, V.Y. Butko, H.M. Yates, M.E. Pemble, and C.M.S. Torres, *App. Phys. Lett.*, **1997**. *70,* 2091.

[52] Muller, M., R. Zentel, T. Maka, S.G. Romanov, and C.M. Sotomayor Torres, *Adv. Mat.*, **2000**. *12,* 1499.

[53] Miguez, H., E. Chomski, F. Garcia-Santamaria, M. Ibisate, S. John, C. Lopez, F. Meseguer, J.P. Mondia, G.A. Ozin, O. Toader, and H.M. Van Driel, *Adv. Mat.*, **2001**. *13,* 1634.

[54] Garcia-Santamaria, F., M. Ibisate, I. Rodriguez, F. Meseguer, and C. Lopez, *Adv. Mat.*, **2003**. *15,* 788.

[55] Subramania, G., K. Constant, R. Biswas, M.M. Sigalas, and K.-M. Ho, *App. Phys. Lett.*, **1999**. *74,* 3933.

[56] Gu, Z.-Z., S. Kubo, W. Qian, Y. Einaga, D.A. Tryk, A. Fujishima, and O. Sato, *Langmuir*, **2001**. *17,* 6751.

[57] Kozhevnikov, V.F., M. Diwekar, V.P. Kamaev, J. Shi, and Z.V. Vardeny.159 in *Proceedings of the Sixth International Conference on Electrica (ETOPIM 6), Jul 15-19 2002*. 2003. Snowbird, UT, United States: Elsevier.

[58] King, J.S., C.W. Neff, C.J. Summers, W. Park, S. Blomquist, E. Forsythe, and D. Morton, *App. Phys. Lett.*, **2003**. *83,* 2566.

[59] King, J.S., C.W. Neff, D.L. Heineman, E.D. Graugnard, and C.J. Summers.W3.9.1 in *Mat. Res. Society*. 2003. Boston, MA.

[60] King, J.S., E. Graugnard, and C.J. Summers, *Submitted for publication.*, **2004**.

[61] Doosje, M., B.J. Hoenders, and J. Knoester, *Journal of the Optical Society of America B (Optical Physics)*, **2000**. *17,* 600.

[62] Suntola, T. and J. Hyvarinen, *Atomic layer epitaxy*, in *Annual review of materials science. Vol.15*. 1985, Annual Reviews. p. 177.

[63] Herman, M.A., *App. Surf. Sci.*, **1997**. *112,* 1.

[64] Kattelus, H., M. Ylilammi, J. Saarilahti, J. Antson, and S. Lindfors, *Thin Solid Films 2nd International Atomic Layer Epitaxy Symposium, 2-5 June 1992*, **1993**. *225,* 296.

[65] Ferguson, J.D., A.W. Weimer, and S.M. George, *App. Surf. Sci.*, **2000**. *162-163,* 280.

[66] Ferguson, J.D., A.W. Weimer, and S.M. George, *Thin Solid Films*, **2000**. *371,* 95.

[67] Sneh, O., R.B. Clark-Phelps, A.R. Londergan, J. Winkler, and T.E. Seidel, *Thin Solid Films*, **2002**. *402,* 248.

[68] Suntola, T. and M. Simpson, *Atomic Layer Epitaxy*. Chapman and Hall, New York **1990**.

[69] Palik, E.D., Ghosh, Gorachand., *Handbook of optical constants of solids*. Academic Press, San Diego **1998**.

[70] Tanemura, S., L. Miao, P. Jin, K. Kaneko, A. Terai, and N. Nabatova-Gabain, *App. Surf. Sci.*, **2003**. *212-213,* 654.

[71] Taki, T., T. Nakajima, A. Koukitu, and H. Seki, *J. Cryst. Growth*, **1998**. *183,* 75.

[72] Ishii, M., S. Iwai, H. Kawata, T. Ueki, and Y. Aoyagi, *J. Cryst. Growth*, *180,* 15.

[73] Price, L.S., I.P. Parkin, T.G. Hibbert, and K.C. Molloy, *Chemical Vapor Deposition*, **1998**. *4,* 222.

[74] Heineman, D., Optimization of ALD grown titania thin films for the infiltration of silica photonic crystals. 2004, Georgia Institute of Technology.

[75] Suntola, T., Method for performing growth of compound thin films, US Patent #4,413,022,

[76] Asikainen, T., ASM Microchemistry

[77] Shionoya, S. and W. Yen, *Phosphor Handbook*. CRC Press, Boca Raton **1999**.

[78] Ritala, M., M. Leskela, E. Nykanen, P. Soininen, and L. Niinisto, *Thin Solid Films*, **1993**. *225,* 288.

[79] Aarik, J., A. Aidla, V. Sammelselg, H. Siimon, and T. Uustare, *J. Cryst. Growth*, **1996**. *169,* 496.

[80] Zhang, J., A. Alsayed, K.H. Lin, S. Sanyal, F. Zhang, W.-J. Pao, V.S.K. Balagurusamy, P.A. Heiney, and A.G. Yodh, *App. Phys. Lett.*, **2002**. *81,* 3176.

[81] Ackerson, B.J., *Journal of Rheology*, **1990**. *34,* 553.

[82] John, S. and K. Busch, *J. Lightwave. Tech.*, **1999**. *17,* 1931.

[83] Yamashita, T., Monte Carlo calculation performed using Matlab, with the assistance of T. Yamashita,

[84] Johnson, S.G. and J.D. Joannopoulos, *Opt. Express*, **2001**. *8,*

[85] Microchemistry, F120 Instruction Manual.

[86] Shionoya, S., Koda, T., Era, K., Jujiwara, H., *J. Phys. Soc. Japan*, **1964**. *19,* 1157.

[87] Aarik, J., A. Aidla, T. Uustare, and V. Sammelselg, *J. Cryst. Growth*, **1995**. *148,* 268.

[88] Wong, S., V. Kitaev, and G.A. Ozin, *Journal of the American Chemical Society*, **2003**. *125,* 15589.

[89] Vlasov, Y.A., K. Luterova, I. Pelant, B. Hoenerlage, and V.N. Astratov, *J. Cryst. Growth*, **1998**. *184-185,* 650.

VITA

Jeffrey Stapleton King was born on July 15, 1976 in Birmingham, AL, the 3rd son of Frank and Kay King. He received his B.S. degree in Materials Engineering from Auburn University in 1998. He was a research associate at Auburn under Dr. R. H. Zee from 1998 to 1999, studying the single crystal growth of refractory alloys. He began his Ph.D. studies in Materials Science and Engineering at the Georgia Institute of Technology in 1999, under Professor C. J. Summers. He is a member of the Materials Research Society, ASM International, TMS, and Keramos honor society.